Implementation of effects violating Lorentz invariance in CORSIKA

Masterarbeit
zur Erlangung des akademischen Grades
Master of Science (M.Sc.)

der Universität Siegen

Department Physik

vorgelegt von
Nico Spornhauer

4. November 2024

Betreuer und erster Gutachter: Prof. Dr. Markus Risse
Zweiter Gutachter: Prof. Dr. Markus Cristinziani

Contents

1. Introduction

It is well known that the Standard Model of particle physics (SM), although very precise with its predictions, is not complete, as it does not describe dark matter or gravity. Some current approaches for more inclusive and fundamental theories (e.g. quantum gravity [1]) allow, as a consequence, for violation of Lorentz invariance, deviations from exact Lorentz symmetry. In case of conserved Lorentz symmetry, the laws of physics are invariant under Lorentz transformation and thereby independent of the frame of observation.

In this work, I will investigate isotropic non-birefringent Lorentz invariance violation in the photon sector, which is affiliated with a simple extension of the SM, conceding Lorentz invariance [2]. The consequences of the introduced Lorentz invariance violation, commonly shortened to Lorentz violation (LV), can be limited to very high energies, which makes extensive air showers (EAS) good candidates for observing such effects indirectly. This approach utilizes ultra-high-energy (UHE) cosmic rays, that induce air showers, where secondary particles can exceed the energies reached by today's accelerators. The effects of LV manifest as a steady accumulation of small changes due to otherwise forbidden interactions and decays in macroscopic observables such as the average atmospheric depth of the shower maximum $\langle X_{\mathrm{max}} \rangle$.

The impact of isotropic non-birefringent LV in the photon sector on EAS has already been studied with the 1-dimensional Monte Carlo (MC) air shower simulation program CONEX [3, 4] and limits were set under the conservative assumption of a pure proton composition of cosmic rays [5]. This approach makes use of the reduction of $\langle X_{\mathrm{max}} \rangle$ due to the modified CONEX code compared to the results of the Pierre Auger Observatory. Limits were improved in a following analysis by adding its shower-to-shower fluctuations $\sigma(X_{\mathrm{max}})$ as an additional observable in the analysis and allowing a mixed composition of particles that induce the air showers [6].

The aim of this thesis is the transfer of the implementation of the Lorentz violating processes from CONEX to CORSIKA [7], a 3-dimensional air shower simulation program, comparing the results with those obtained by CONEX and observing the influence of LV on newly obtained observables. The eventual goal is an improved search for Lorentz violation by including observables unavailable to a 1-dimensional simulation, such as those connected to the lateral particle distribution.

2. Physical Background

In this chapter, the physical background for the work done in this thesis is explained. The impact of LV on air shower observables is assessed through Monte Carlo simulations. Extensive air showers are induced by cosmic rays and described by interactions between particles according to the Standard Model of particle physics.

For this purpose, Lorentz symmetry is outlined in Section 2.1, covering Lorentz transformations and the concept of Lorentz invariance. Section 2.2 describes the Standard Model of particle physics, including an overview of particles and their interactions. The central theoretical background for LV is addressed in Section 2.3, highlighting particle interactions affected by LV. Cosmic rays are introduced in Section 2.4, which due to their extremely high energies are good candidates for LV testing and are responsible for initiating EAS. Finally, extensive air showers are detailed in 2.5, explaining their components, simplified models, and briefly introducing the Pierre Auger Observatory.

It should also be noted here, that natural units, $c = \hbar = 1$, have been used, when the corresponding physical constants are not explicitly written, as well as the following definition of the Minkowski metric $\eta_{\mu\nu} = [\mathrm{diag}(1, -1, -1, -1)]_{\mu\nu}$.

2.1 Lorentz Symmetry

Lorentz symmetry is a cornerstone of physics, a foundation which is preserved in most commonly accepted theories, most notably Special Relativity. The Standard Model of particle physics is also a Lorentz invariant theory, meaning that the physics does not depend on the frame of reference.

It is helpful to start with the Galilei transformation, which is the intuitive coordinate transformation, which is valid for speeds much lower than the speed of light, and explain why it has been replaced by the Lorentz transformation. The Galilei transformation relates the coordinates in one inertial frame S to the coordinates in another reference frame S' that is moving at a constant velocity v with respect to the first frame. The z-axis can be arbitrarily chosen to align with the direction of the velocity, with which the frames move relative to each other. Its equations are given by [8]:

$$\begin{aligned} t' &= t, \\ x' &= x, \\ y' &= y, \\ z' &= z - vt \end{aligned} \tag{2.1.1}$$

Mathematically, Galilei transformations build a group together with translations in space and time, and rotations. A typical illustration for different observations is the trajectory of a vertically thrown ball in a moving train, viewed from inside and outside the train. Even though the form of the trajectory changes when you change the reference frame, the underlying physics do not, as you can transpose your observations by transforming your coordinates through a Galilei transformation [8].

While this transformation is a good approximation at speeds much lower than the speed of light, it has to be replaced by the Lorentz transformation to explain some physical observations where Galilei transformations fail.

The Lorentz transformation was introduced to solve the incompatibility of the Maxwell equations under Galilei transformations and later formed the foundation for Special Relativity. The Galilei transformation equations are replaced by the equations for a Lorentz transformation [9]:

$$\begin{aligned} t' &= \gamma \left(t - \beta z \right), \\ x' &= x, \\ y' &= y, \\ z' &= \gamma \left(z - \beta t \right), \end{aligned} \tag{2.1.2}$$

with $c = 1$, $\beta = vc^{-1}$ and $\gamma = (\sqrt{1 - \beta^2})^{-1}$.

In the limit for $c \to \infty$ the Lorentz transformation will reduce to the Galilei transformations.

A quantity unchanged by a Lorentz transformation is called a Lorentz scalar or invariant and is the same in all reference frames. Examples include the speed of light or the mass of a particle. As the Lorentz transformation was introduced to change the electric and magnetic fields, they are, on the contrary, not invariant under Lorentz transformations, and they instead transform according to [9]:

$$\begin{aligned} E'_x &= \gamma\left(E_x - \beta B_y\right) & B'_x &= \gamma\left(B_x + \beta E_y\right) \\ E'_y &= \gamma\left(E_y + \beta B_x\right) & B'_y &= \gamma\left(B_y - \beta E_x\right) \\ E'_z &= E_z & B'_z &= B_z \end{aligned} \tag{2.1.3}$$

The electric field strength tensor F is therefore also not Lorentz invariant as we do not measure the same electric and magnetic fields in all reference frames. Its components can be written using the vector potential A:

$$F^{\mu\nu} = \partial^\mu A^\nu - \partial^\nu A^\mu \tag{2.1.4}$$

Or in matrix form, the tensor looks like the following, together with its covariant form [9]:

$$F^{\mu\nu} = \begin{pmatrix} 0 & -E_x & -E_y & -E_z \\ E_x & 0 & -B_z & B_y \\ E_y & B_z & 0 & -B_x \\ E_z & -B_y & B_x & 0 \end{pmatrix}, \; F_{\mu\nu} = \begin{pmatrix} 0 & E_x & E_y & E_z \\ -E_x & 0 & -B_z & B_y \\ -E_y & B_z & 0 & -B_x \\ -E_z & -B_y & B_x & 0 \end{pmatrix} \tag{2.1.5}$$

For a free field, one can write the Lagrangian density, commonly abbreviated as Lagrangian, from which one can extract the Maxwell equations through the Euler-Lagrange equations as the contraction of two field strength tensors:

$$\mathcal{L} = -\frac{1}{4} F^{\mu\nu} F_{\mu\nu} \tag{2.1.6}$$

This Lagrangian is now a Lorentz scalar and one says it is symmetric under Lorentz transformations as:

$$\begin{aligned} \mathcal{L}' &= -\frac{1}{4} F'_{\mu\nu} F'^{\mu\nu} = -\frac{1}{2}\left(\vec{B}'^{\,2} - \vec{E}'^{\,2}\right) \\ &= -\frac{1}{2}\left(\gamma^2 (B_x + \beta E_y)^2 + \gamma^2 (B_y - \beta E_x)^2 + B_z^2\right) \\ &\quad + \frac{1}{2}\left(\gamma^2 (E_x - \beta B_y)^2 + \gamma^2 (E_y + \beta B_x)^2 + E_z^2\right) \\ &= -\frac{1}{2}\left(\gamma^2 (1-\beta^2)(B_x^2 + B_y^2) + B_z^2 - \gamma^2 (1-\beta^2)(E_x^2 + E_y^2) - E_z^2\right) \\ &= -\frac{1}{2}\left(\vec{B}^{\,2} - \vec{E}^{\,2}\right) = -\frac{1}{4} F_{\mu\nu} F^{\mu\nu} = \mathcal{L} \; . \end{aligned} \tag{2.1.7}$$

If the Lagrangian is invariant under Lorentz transformations, then the equations derived from it, such as Maxwell's equations, remain consistent in all reference frames. Lorentz invariance implies that the action, which is defined as the integral of the Lagrangian over spacetime, is also invariant. This ensures that the physical laws underlying electromagnetism are the same, independent of the frame of observation.

In short, Lorentz invariance means, in the context of this thesis, that the physics do not change when changing the frame of observation.

2.2 Standard Model of Particle Physics

The SM is a relativistic quantum field theory. It successfully explains three of the four fundamental forces -strong, weak, and electromagnetic- in a single framework, while describing all known elementary particles and their interactions between them. The following section provides a brief overview of the SM. A more comprehensive explanation of the SM can be found in many textbooks, including [10, 11, 12]. The Lagrangian of the SM, which describes the dynamics of the theory, can be neatly written as a single equation often depicted at T-shirts or coffee mugs [13]. The elementary particles described by the SM can be organized in a small table that illustrates their properties. Mathematically, the SM is described by the gauge symmetry SU(3)×SU(2)×U(1). In particular, SU(3) represents the strong interaction through quantum chromodynamics, while SU(2)×U(1) characterizes the electroweak interaction, the unification of the weak and electromagnetic forces. The model also has additional symmetries. These are linked to conservation laws by Noether's theorem like the conservation of electric charge, dictating which interactions are possible.

The SM describes particles and its interactions to very high precision, but it doesn't explain all observations, like gravity, dark matter, or neutrino oscillation and as thus it is incomplete. This demands theories beyond the SM.

2.2.1 Particles

The SM classifies elementary particles into quarks, leptons, gauge bosons, and the Higgs boson, as can be seen in Figure 2.1. The table is organized by the properties of the particles, such as spin, charge, mass, and how they interact via the fundamental forces. The elementary particles include six different kind of quarks, so-called flavors, as well as six lepton flavors, grouped in three generations each, four gauge bosons mediating three of the fundamental forces and the Higgs, a scalar boson responsible for giving particles their mass.

Quarks and Leptons

Quarks and leptons are the particles which make up matter. Both are fermions, meaning they have a half-integer spin, in our case each flavor has a spin of 1/2. One distinguishes quarks between up-type quarks in the first row with namely up, charm, and top flavor and down-type quarks in the second row called down, strange, and bottom. Up-type quarks have an electric charge of 2/3, while down-type quarks have a charge of -1/3.

Leptons are grouped by their charge as well. The top row containing the electron, muon and tau have a charge of -1. The bottom row contains their corresponding neutrinos with no electric charge.

The mass increases from generation to generation, except for neutrinos where the SM predicts the mass to be 0. The difference in mass is also quite considerable. The top quark for example is with about 173 GeV as heavy as a single gold atom [15].

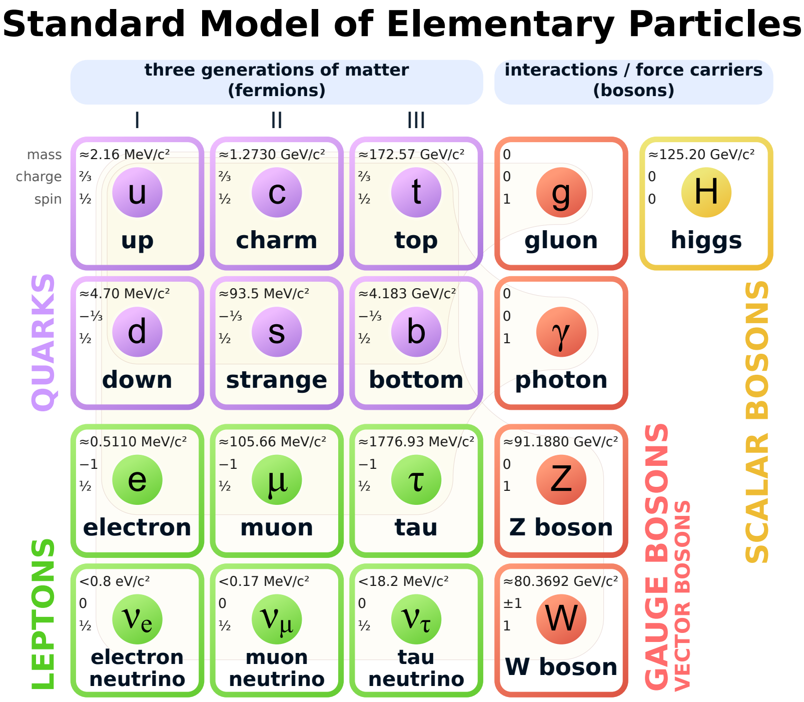

Figure 2.1. *Elementary particles of the Standard Model of particle physics* [14].

In total this results in 12 flavors of particles between quarks and leptons, but each particle also has its so-called antiparticle, bringing the total to 24 so far. Antiparticles have the same mass as the regular particle, but opposite quantum numbers corresponding to charges. For example, the positron, the electron's antiparticle, is therefore positively charged.

In our everyday life, however, we only witness matter composed from the first generation: Up and down as valence quarks make up protons and neutrons, that together built atomic nuclei and together with electrons atoms, that make up the world we live in. This is because the heavier particles are not stable and will eventually decay into lighter particles.

Gauge Bosons and Interactions

The fundamental forces that are described by the SM are the electromagnetic, weak and strong interactions, but not the comparatively weak gravitation. These interactions are mediated by force carriers: Gluon for strong, photon for electromagnetic, and the Z and W bosons for the weak interaction. The force carriers are called vector bosons with an integer spin of 1. The Bose-Einstein-statistic applies to collections of them, in contrast to fermions, which obey the Fermi-Dirac-statistic. A force carrier can only mediate interactions if a particle has the corresponding charge. The binding force between protons and neutrons in an atomic nuclei for example is due to the strong interaction, while the weak interaction is responsible for the radioactive beta decay.

Electrically charged particles are subject to the electromagnetic interaction, where the force between the particles are described by the exchange of (virtual) photons. This is the reason why photons and the other gauge bosons are called force carriers. This interaction is described in quantum electrodynamics (QED), which is an extension of classical electrodynamics.

Quarks have an additional so-called color charge, either blue, red, or green, which is the charge corresponding to the strong interaction. In contrast, antiquarks have a charge of anti-blue, anti-red, or anti-green. It is important to note here, that quarks are confined and not found freely, such that the particles they form are always color neutral. Meaning Quarks can form particles by either a quark-antiquark pair, where the color and anti-color cancel each other, or in a 3 quark state, where blue, red, and green form again a color neutral state. These compound particles are called hadrons. In the case of a quark-antiquark pair, they are named mesons or baryons, when 3 quarks form the particle, like a proton, which consists of two up quarks and one down quark. Quarks and antiquarks can interact with the gluon, which has 2 effective color charges, one color and one anti-color, being able to change the color of a quark, when interacting with it. For example a quark with blue color can interact with a gluon with anti-blue and green, leaving the quark with a green color as blue and anti-blue cancel. With three possible colors and corresponding anti-colors, there would be nine gluons, but the gluon to be more precise is actually in a color state, that is a linear combination of those effective states. This leaves a color singlet state, which is colorless, and an octet of eight linear independent states, which correspond to the Gell-Mann matrices. The color singlet state does not exist, as this would imply that the gluon would couple to colorless particles, allowing long range interactions. Therefore only eight gluons exist.

The weak interaction is mediated by 3 force carriers, the Z boson and the two W bosons. The W bosons are the only electrically charged force carriers with a positive or negative charge of 1, respectively. All particles interact weakly, but since neutrinos have no electrical or color charge, the weak interaction is their only interaction channel and they are therefore difficult to detect.

Higgs Boson

The last elementary particle in Figure 2.1 is the Higgs and its discovery in 2012 was another major success for the SM. It is a scalar boson due to its spin of 0. It is created by the excitation of the Higgs field and decays rapidly into other particles.

The Higgs mechanism is the explanation on how the particles aquire their mass as it describes the interaction of particles with the permeating Higgs field, which has a non-zero expectation value due to spontaneous symmetry breaking. The breaking of the electroweak symmetry gives the W and Z bosons mass, while photons remain massless as the electromagnetic gauge symmetry, in contrast, remains unbroken.

2.2.2 Lagrangian

In quantum field theory, particles are described by corresponding quantized fields. The fields must satisfy certain field equations. For scalar fields this is the Klein-Gordon equation, for spinor fields the Dirac equation, for massive vector fields the Proca equation, and for massless photons, the Maxwell equations. These field equations must be derived for free fields from the Euler-Lagrange equations. The part describing the free propagation of particles in the Lagrangian is called the kinetic term.

$$\text{Klein-Gordon equation:} \qquad (\partial_\mu \partial^\mu + m^2)\phi = 0 \tag{2.2.1}$$
$$\text{Dirac equation:} \qquad (i\gamma^\mu \partial_\mu - m)\psi = 0 \tag{2.2.2}$$
$$\text{Proca equation:} \qquad \left[(\partial^\mu \partial_\mu + m^2)g^{\mu\nu} - \partial^\mu \partial^\nu\right] A_\nu = 0 \tag{2.2.3}$$
$$\text{Maxwell equation:} \qquad \partial_\mu F^{\mu\nu} = 0 \tag{2.2.4}$$

Here, ∂_μ is the four-gradient operator, m represents the mass, ϕ is the scalar field, γ^μ are the gamma matrices, ψ is the spinor field, A is the vector field, and $F^{\mu\nu}$ is the electromagnetic field tensor [16].

Interactions introduce additional terms to the Lagrangian, so that the equations of motion for the fields change.

The complete SM Lagrangian is often compressed in the compact form:

$$\mathcal{L}_{\text{SM}} = -\frac{1}{4} F_{\mu\nu} F^{\mu\nu} + i\bar{\psi} \not{D} \psi + \text{h.c.} + \psi_i Y_{i,j} \psi_j \phi + \text{h.c.} + |D_\mu \phi|^2 - V(\phi) \tag{2.2.5}$$

In this equation, $F_{\mu\nu}$ are the different gauge fields, ψ is the spinor field, $\not{D}$ is the Feynman slash notation for the covariant derivative, $Y_{i,j}$ are the Yukawa couplings, ϕ the Higgs field and $V(\phi)$ is the Higgs potential. Here, the interaction terms are hidden behind the fact, that the covariant derivative D_μ contains the gauge couplings and gauge fields, which ensures the Lagrangian is invariant under local gauge transformations.

Quantum Electrodynamics

Quantum Electrodynamics is a quantum field theory which describes the interaction between spin-$\frac{1}{2}$ fermions and photons and is important in the context of this thesis.

$$\mathcal{L}_{\text{QED}} = -\frac{1}{4} F_{\mu\nu} F^{\mu\nu} + \bar{\psi}(i\gamma^\mu \partial_\mu - m)\psi - e\bar{\psi}\gamma^\mu \psi A_\mu \tag{2.2.6}$$

This Lagrangian can be separated into three components, two kinetic terms and one interaction term. The first term is the kinetic term describing the free propagation of photons and the second is the kinetic term for the fermions, describing their free propagation. Here $F^{\mu\nu}$ now only depicts the electromagnetic field tensor. One can also see, that the Euler-Lagrange equations for the kinetic terms will yield the Maxwell and Dirac equation for the photon and fermions respectively.

$$\frac{\partial \mathcal{L}}{\partial \phi} - \partial_\mu \left(\frac{\partial \mathcal{L}}{\partial(\partial_\mu \phi)} \right) = 0 \tag{2.2.7}$$

Here, ϕ is the field in question. The last term $e\bar{\psi}\gamma^\mu \psi A_\mu$ is the interaction term, where the elemental charge $e = \sqrt{4\pi\alpha}$ is the electromagnetic coupling, with the fine-structure constant $\alpha \approx \frac{1}{137}$, which couples the fermion fields ψ with the photon field A.

2.2.3 Conservation Laws

Noether's theorem states that a symmetry leads to a conserved current. The SM incorporates several symmetries, leading to conservation laws. Some examples include the invariance under time and space translation, which leads to energy and momentum conservation. Whether certain interactions are allowed can be determined by these conservation laws. However, some conservation laws depend on the interaction, which is illustrated for some quantities in Table 2.1. For example, isospin must be conserved only for the strong interaction and parity conservation is violated for the weak interaction.

Conserved Quantity	electromagnetic i.a.	weak i.a.	strong i.a.
Energy	yes	yes	yes
Momentum	yes	yes	yes
Angular momentum	yes	yes	yes
Baryon number B	yes	yes	yes
Lepton number L	yes	yes	yes
Parity P	yes	no	yes
Charge Conjugation C	yes	no	yes
Product CP	yes	no	yes
Time Reversal T	yes	no	yes
Product CPT	yes	yes	yes

Table 2.1. *Conservation of sample quantities for the different interactions in the SM* [17].

The following consideration shows how four-momentum conservation kinematically forbids an interaction in the SM, which will be allowed in the Standard Model extension, discussed in the next section. The interaction in question is the radiation of a photon from an electron in vacuum. Since the theory is Lorentz invariant, one can look at it from the electrons rest frame, such that the momentum of the electron $\vec{p'}_e$ and photon $\vec{p}_\gamma$ after the interaction have to be back-to-back $\vec{p'}_e = -\vec{p}_\gamma$.

$$
\begin{aligned}
p_e &= p'_e + p_\gamma \\
m_e^2 &= m_e^2 + E'_e E_\gamma - (-\vec{p}_\gamma^{\,2}) \\
0 &= E'_e E_\gamma + \vec{p}_\gamma^{\,2} > 0, \text{ for } E_\gamma > 0
\end{aligned}
\tag{2.2.8}
$$

This is a contradiction, making it kinematically forbidden without an external field.

2.3 Lorentz Invariance Violating Extension of the Standard Model

The Lorentz invariance violation investigated in this work is introduced through an extension of the QED Lagrangian density [18, 19]. One additional term, that only contains the electromagnetic field strength tensor alongside the tensor $(k_F)_{\mu\nu\rho\sigma}$, which does not correspond to any field, is added. Therefore, this represents a modification of the photon behavior compared to the SM.

$$\mathcal{L}(x) = \mathcal{L}_{\mathrm{QED}} - \frac{1}{4}(k_F)_{\mu\nu\rho\sigma}F^{\mu\nu}F^{\rho\sigma} \tag{2.3.1}$$

The tensor $(k_F)_{\mu\nu\rho\sigma}$ has 20 independent constant components. Ten of those produce birefringence, while eight are responsible for direction-dependent modifications of the photon propagation, and one leads to an unobservable double trace, which changes the normalization of the photon field. The last component, here called κ, is the only component of interest for this thesis as it is responsible for the isotropic, non-birefringent violation of Lorentz invariance and is included in $(k_F)_{\mu\nu\rho\sigma}$ as follows:

$$(k_F)_{\mu\nu\rho\sigma} = \frac{1}{2}\left(\eta_{\mu\rho}\tilde{\kappa}_{\nu\sigma} - \eta_{\mu\sigma}\tilde{\kappa}_{\nu\rho} + \eta_{\nu\sigma}\tilde{\kappa}_{\mu\rho} - \eta_{\nu\rho}\tilde{\kappa}_{\mu\sigma}\right) \tag{2.3.2}$$

with

$$\tilde{\kappa}_{\mu\nu} = \frac{\kappa}{2}[\mathrm{diag}(3,1,1,1)]_{\mu\nu}, \tag{2.3.3}$$

where κ is restricted to the half-open interval $(-1, 1]$ [2]. This approach preserves the gauge invariance as well as the CPT invariance under the combined transformation of charge conjugation, parity reflection, and time reversal, which are required in the SM. For $\kappa = 0$, one obtains the Lagrangian of the SM.

The LV parameter κ can also be described by the phase velocity v_{ph} of the non-standard photon $\tilde{\gamma}$, since in this theory it is dependent on κ:

$$v_{\mathrm{ph}} = \frac{\omega}{k} = \sqrt{\frac{1-\kappa}{1+\kappa}}c \tag{2.3.4}$$

$$\kappa = \frac{c^2 - v_{\mathrm{ph}}^2}{c^2 + v_{\mathrm{ph}}^2} \approx 1 - v_{\mathrm{ph}} \tag{2.3.5}$$

The speed of light in the SM, which is the maximum achievable fermion speed, has been set to $c = 1$. The non-standard photon is also referred to as a fast photon for negative κ, as its phase velocity is now greater than c, and a slow photon for positive κ. With a nonzero κ, various interactions forbidden in the SM are allowed. For easier understanding, the cases for negative and positive κ are separated.

2.3.1 Positive Values of κ

For $\kappa > 0$, charged particles are contrary to the SM allowed to radiate photons, called vacuum Cherenkov (VCh) radiation. This process happens continuously until the particle energy is below the following energy threshold [20]:

$$E_{\text{thresh}}^{\text{VCh}}(\kappa) = m\sqrt{\frac{1+\kappa}{2\kappa}} \approx \frac{m}{\sqrt{2\kappa}} \tag{2.3.6}$$

The emission rate Γ is dependent on the energy of the radiated photon, which is cut off at an upper bound ω_{max} and which is described by the following two equations [21]:

$$\frac{d\Gamma}{d\omega} = \frac{\alpha Z^2}{E\sqrt{E^2 - m^2}}\left[\frac{2\kappa E}{1-\kappa^2}(E-\omega) - \frac{m^2}{1-\kappa} + \frac{\kappa}{(1-\kappa^2)(1-\kappa)}\omega^2\right] \tag{2.3.7}$$

$$\omega_{\text{max}} = \left(\frac{1-\kappa}{\kappa}\right)\left[\sqrt{\frac{1+\kappa}{1-\kappa}}\sqrt{E^2-m^2} - E\right] \tag{2.3.8}$$

Here, ω is the photon energy, α is the fine-structure constant, and Z is the particle charge in natural units ($e = 1$).

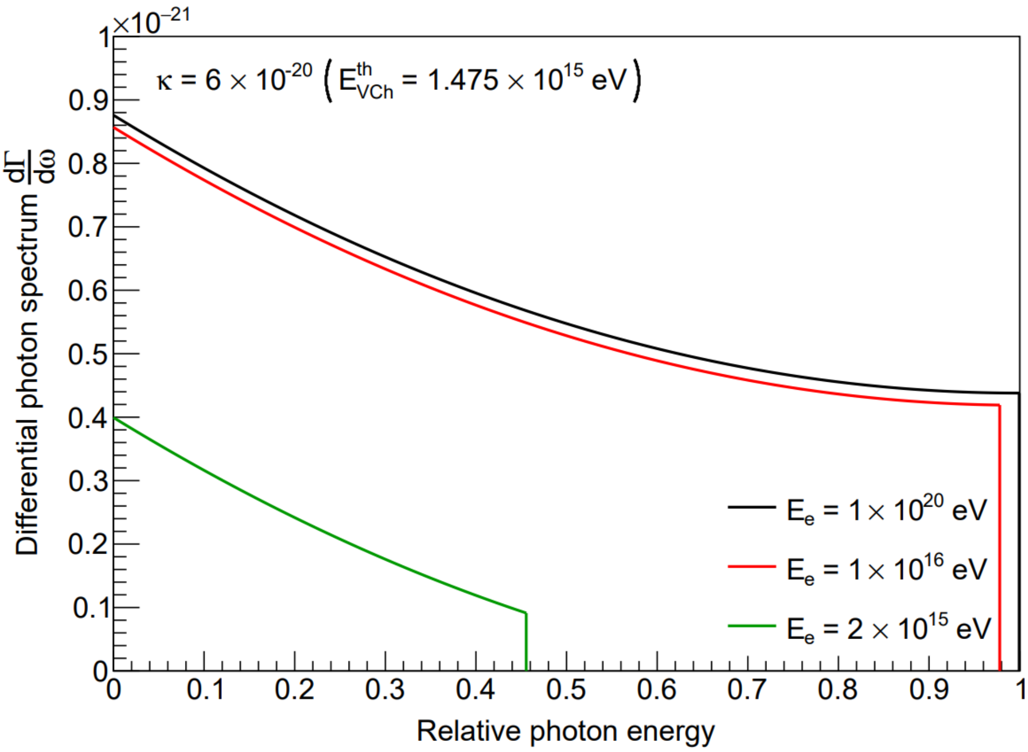

Figure 2.2. *Emission rates of VCh photons for $\kappa = 6 \times 10^{-20}$, which inherit a relative energy fraction of one primary electron, with different energies* [22]. *The emission rate is given by Equation* (2.3.7).

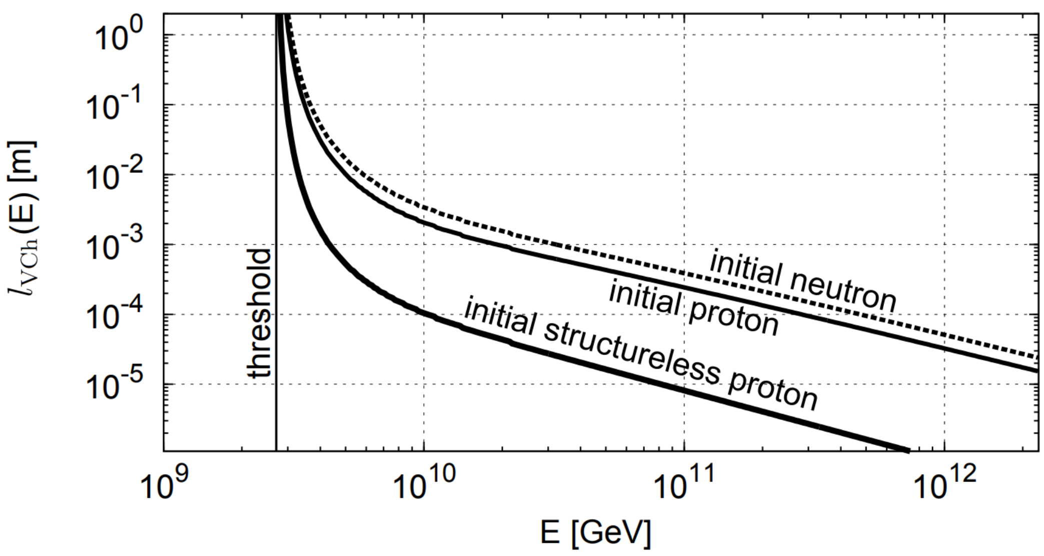

Figure 2.3. *VCh radiation length l_{VCh} for $\kappa = 6 \times 10^{-20}$ in meters for a proton, a neutron, and a structureless charged Dirac fermion* [21].

Figure 2.2 shows that the photons can inherit a significant fraction of the primary energy of the charged particle. Close to the threshold energy, the electron can still radiate about 45% of its energy as can be seen by the green line. For larger energies the maximum of the radiated energy fraction becomes nearly a 100% as can be seen by the black line.

Figure 2.3 illustrates the interaction length for VCh radiation, which drops to below a meter scale shortly above the threshold energy. Together this results in an efficient energy loss, leading to the conclusion that charged particles above the threshold energy from distant sources cannot reach the Earth if they undergo VCh radiation.

2.3.2 Negative Values of κ

For $\kappa < 0$, there are two interactions to consider. Firstly, the non-standard photons $\tilde{\gamma}$ decay into an electron-positron pair at sufficiently high energies. Secondly, the decay of neutral pions is affected, increasing the lifetime with increasing energy of the pion until they become stable at energies exceeding a cut-off energy [20, 23, 24].

$$\tilde{\gamma} \to e^- + e^+ \tag{2.3.9}$$
$$\pi^0 \to \tilde{\gamma} + \tilde{\gamma} \tag{2.3.10}$$

The energy thresholds above which the photon decay takes place and neutral pions become stable are described by the following two equations [20, 24]:

$$E^{\gamma}_{\mathrm{thresh}}(\kappa) = 2m_e\sqrt{\frac{1-\kappa}{-2\kappa}} \approx \frac{2m_e}{\sqrt{-2\kappa}} \tag{2.3.11}$$
$$E^{\pi^0}_{\mathrm{cut}}(\kappa) = m_{\pi^0}\sqrt{\frac{1-\kappa}{-2\kappa}} \approx \frac{m_{\pi^0}}{\sqrt{-2\kappa}} \approx \frac{m_{\pi^0}}{2m_e}E^{\gamma}_{\mathrm{thresh}} \approx 132 E^{\gamma}_{\mathrm{thresh}} \tag{2.3.12}$$

where α again stands for the fine-structure constant.

With the rest masses $m_{\pi^0} \approx 135$ MeV and $m_e \approx 511$ keV inserted, the approximations of the energy thresholds show that the pions become stable only at an energy that is about two orders of magnitude larger than the threshold energy of the photon decay.

The photon decay (PhD) rate Γ_{PhD} can be described by [21]:

$$\Gamma_{\mathrm{PhD}}(E_\gamma) = \frac{\alpha}{3} \cdot \frac{-\kappa}{(1-\kappa)^2} \sqrt{E_\gamma^2 - (E^\gamma_{\mathrm{thresh}})^2} \cdot \left(2 + \left(\frac{E^\gamma_{\mathrm{thresh}}}{E_\gamma}\right)^2\right) \tag{2.3.13}$$

As shown in Figure 2.4, the decay length is only a few centimeters just above the energy threshold. This means that the decay in the context of air showers, which is the environment under which the effects of LV are investigated in this thesis, is quasi-instantaneous.

The lifetime of neutral pions is modified by a factor $g(E_{\pi^0}, \kappa)$, which is zero above $E^{\pi^0}_{\mathrm{cut}}$, so that the pion is stable in this theory [24].

$$\tau(E_{\pi^0}, \kappa) = \frac{\tau_{\mathrm{SM}}}{g(E_{\pi^0}, \kappa)}, \text{ with} \tag{2.3.14}$$

$$g(E_{\pi^0}, \kappa) = \frac{\sqrt{1-\kappa^2}}{(1-\kappa)^3} \left[1 - \frac{(E_{\pi^0})^2 - (m_{\pi^0})^2}{(E^{\pi^0}_{\mathrm{cut}})^2 - (m_{\pi^0})^2}\right], \text{ for } E_{\pi^0} \leq E^{\pi^0}_{\mathrm{cut}} \tag{2.3.15}$$

where τ_{SM} is the lifetime of the neutral pion in the Standard Model.

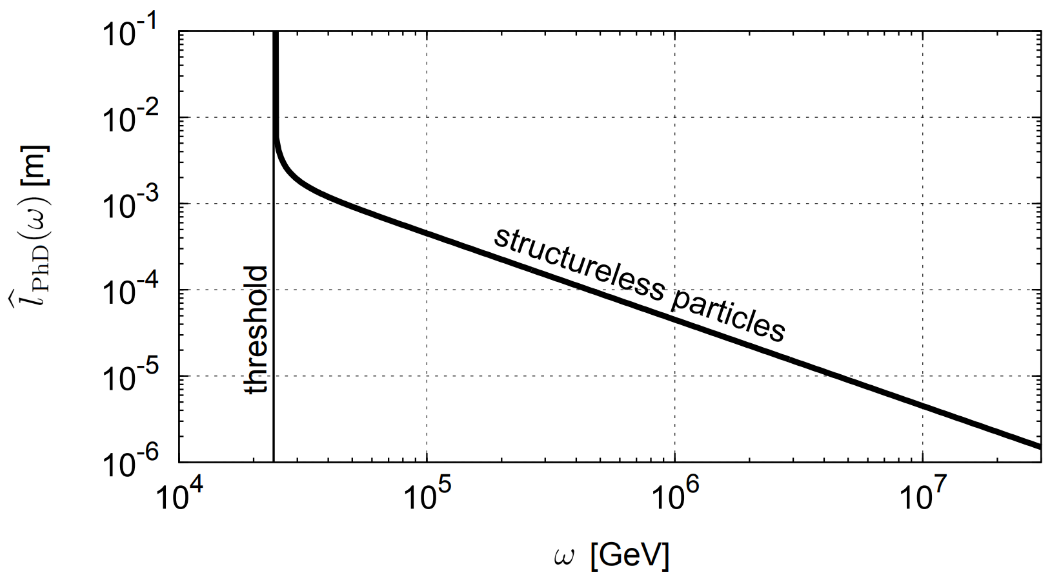

Figure 2.4. *Photon decay length $\hat{l}_{PhD}$ for $\kappa = -9 \times 10^{-16}$ in meters against photon energy ω [21]. The threshold energy is given by equation (2.3.11).*

2.4 Cosmic Rays

An EAS arises from a primary particle that comes from outside the atmosphere and interacts with it. Due to historic reasons, only those particles that are charged are called cosmic rays (CR). In spite of this, neutral particles are also of interest, as they, unlike charged particles, are not deflected by magnetic fields during propagation. Therefore, researchers look in this regard especially for high-energy photons and neutrinos that can provide information about the sources.

Observatories stationed on Earth usually measure secondary particles of EAS, with the exception of neutrinos, that require enormous detectors due to their small cross-section. From measurements of EAS, properties like the energy of the shower initiating particle can be inferred. This type of measurement is called indirect. To directly measure the primary particles, the primary particles themselves must interact with the detectors. Therefore, experiments above the Earth's atmosphere are particularly suitable for this purpose. Particle identification, energy, and direction determination can be achieved by combining different types of detectors in space with satellite experiments. One such satellite experiment is PAMELA, standing for "Payload for Antimatter Matter Exploration and Light-nuclei Astrophysics," which primarily searched for antimatter in CR between 2006 and 2016 [25].

While the origin and acceleration of CR are interesting topics of research, they are not directly relevant for this thesis and won't be detailed any further. The two characteristics of CR, that will be discussed in the next subsections are the elemental composition of CR that reach the Earth and the energy spectrum, as the argument of a mixed composition is later used and to show, why to study LV using EAS instead of direct measurements.

2.4.1 Elemental Composition

CR that reach the Earth are composed of charged stable particles, including protons, ionized atomic nuclei, and electrons. These compositions are primarily determined by direct measurements at low energies in the context of CR and are still uncertain for the highest energies. The main components of primary cosmic rays at lower energies are protons and helium nuclei. Heavier nuclei, as well as electrons or positrons, each make up about one percent of the energy at a few GeV. The composition of galactic cosmic rays (GRC) is comparable to composition in the solar system. The relative abundance is shown in Figure 2.5. The lower frequency of hydrogen and helium in GCR can be explained through their high ionization energies, as most acceleration mechanisms only accelerate charged particles, while the increased abundance of certain elements compared to the solar system is due to them being spallation products, and therefore, a measure of the amount of matter traversed during particle propagation [26].

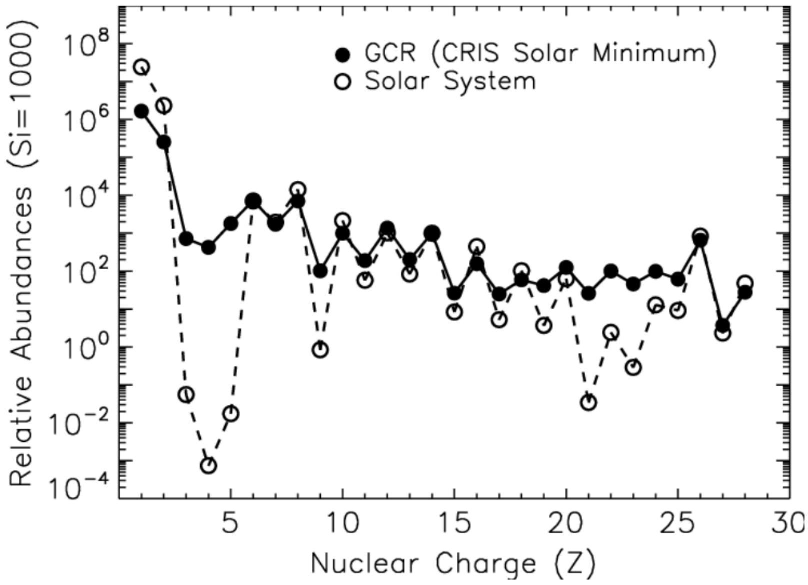

Figure 2.5. *The elemental abundance of galactic cosmic rays is compared with that of the solar system. The values are normalized for Si* ($Z = 14$) *to* 1000 [27].

The composition at higher energies is unknown and still subject to research. One difficulty is the low flux of particles at the highest energies, which is further detailed in the next subsection. It is connected to a smaller statistic size and, on the other hand, the ability to discriminate different CR due to the lack of direct measurements and the reliance on indirect measurements. Those have to be based on measured properties of air showers, which makes it challenging, as the distributions for X_{max} (see Section 2.5) for example overlap for different primary particles initiating the air shower.

Although the exact composition is unknown, it is known that the composition is mixed and tends to heavier nuclei for increasing energies. With air shower simulations and measurements, such as from the Pierre Auger Observatory, this can be shown with different approaches. One caveat is the limited knowledge of the hadronic interactions as there are no accelerators experiments that can produce these kind of energies such that the extrapolated hadronic interaction models bring significant uncertainties with them in this regard. In Figure 2.6 a transition from the measured data from the simulated proton line to the iron line can be observed for energies $E \gtrsim 10^{18.5}$ eV for 3 different hadronic interaction models, indicating a mixed composition.

One approach to determine the fractions of each particle is to fit a mixture of primaries to the overall measured distribution of X_{max}. A study found that a model of two-components with proton as lightest and iron as heaviest, could not describe the observed data, but including intermediate nuclei significantly improved the fits. Additionally, this brought the different interaction models in their prediction of proton and iron fractions in agreement, but with large differences for the remaining nuclei. It also noted that the trend could be due to deviations from the extrapolation in hadronic interaction models, not an evolution of composition mix [29].

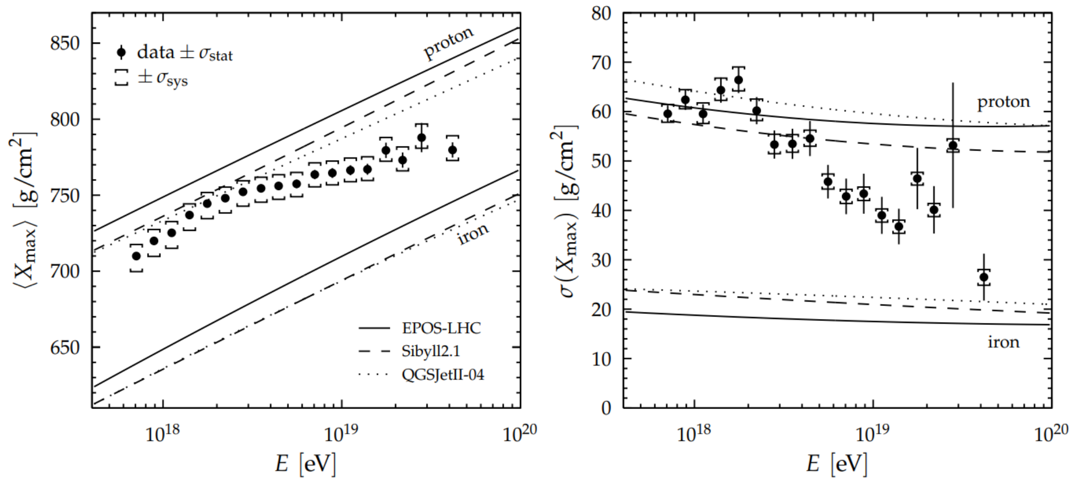

Figure 2.6. *Comparison of the first two central moments of the X_{max} distribution for measurements and simulations with proton and iron primaries plotted against energy* [28].

A different, more stable approach that determines a mixed composition, but not the specific fraction of each element, uses the correlation between $X_{\max}$ and N_μ in air showers. It was found that the simulations with a pure composition were in conflict with data, but instead support a mixed composition that also includes heavier nuclei with $A > 4$. Changing the muon component or key hadronic parameters in the simulations did not affect the findings [30].

2.4.2 Energy Spectrum

The spectrum of cosmic radiation is known over many orders of magnitude in energy, and a power law is found for the differential flux Φ:

$$\Phi(E) \sim E^{-\gamma} \tag{2.4.1}$$

Here, γ denotes the spectral index, which is around 2.7 starting from about 10 GeV. Solar modulation influences incoming particles at lower energies of around $E < 1$ GeV/nucleon, and thus affecting the flux of cosmic radiation. However, the flux is lower with higher solar wind, because it shields against other radiation. The flux is shown in Figure 2.7 and while the energy covers many magnitudes on the x-axis, the flux itself spans over 30 magnitudes due to the steep slope γ in the double logarithmic plot.

The strongly decreasing number of particles at higher energy makes different measurements necessary. A direct measurement with balloon flights or satellites, with the associated small detector areas, won't generate sufficient statistics at the higher energy range of the flux, where the flux falls from around one particle per m^2 and year at energies above 1 PeV to one particle per km^2 and century at 10^{20} eV. This is why, at energies above the PeV range, measurements are taken indirectly through air shower experiments, where detector arrays can cover square kilometers, measuring secondary particles.

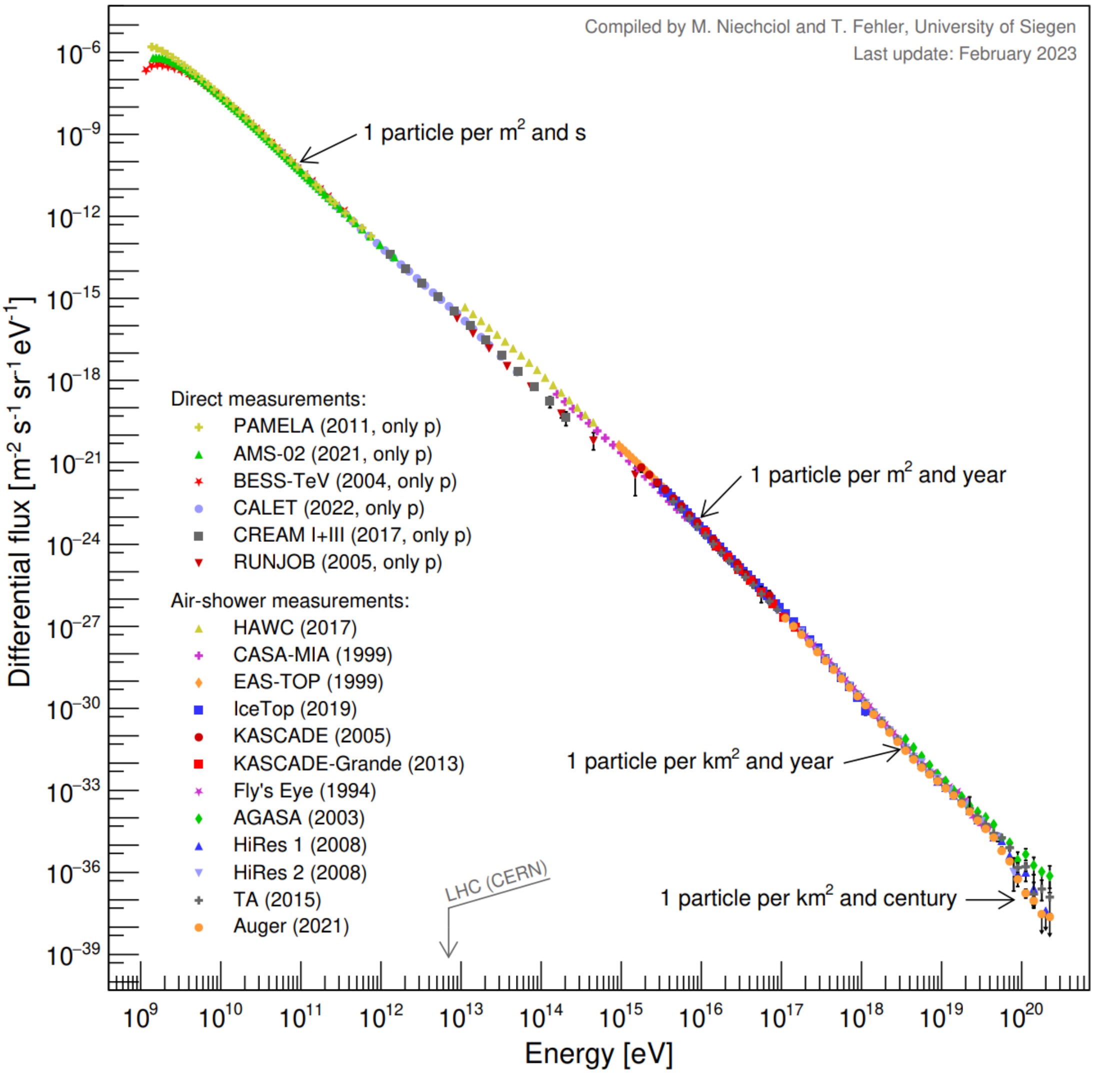

Figure 2.7. *The energy spectrum of cosmic rays, as observed by a variety of experiments. The direct measurements only show the flux of protons* [31].

Spectral Index Changes

The overall energy spectrum for all CR has some distinct features, where the spectral index does change at certain energies. The first bend in the plot is called knee at around 3 PeV as the index increases to $\gamma = 3$, leading to a steeper line. Other changes in the spectral index are also called after characteristics of the human leg, such as the ankle at around 3 EeV, where the spectral index flattens again to about $\gamma = 2.7$, which can be seen in Figure 2.8. There are different theories for those characteristics, such as the transition from galactic to extragalactic sources for the ankle [26].

The spectral index does also vary for different particle types. As for example electrons lose energy faster due to bremsstrahlung than protons, so the flux for electrons decreases faster at higher energies.

At the highest energies the flux drops sharply. The origin of this is unclear, proposed

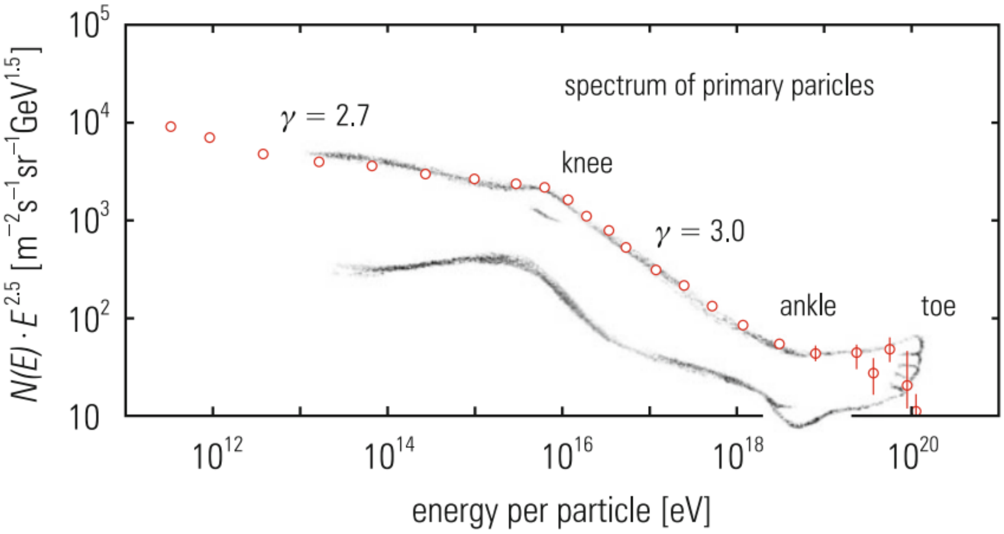

Figure 2.8. *Artist's view of the different structures in the spectrum of primary CR.* [26].

explanations are suppression by the GZK effect during particle propagation or due to the maximum energy at the source.

Flux Suppression

The GZK effect, named after Kenneth Greisen, Georgi Zatsepin, and Vadim Kuzmin, describes the energy loss of ultra-high-energy protons through interactions with the cosmic microwave background radiation. This sets a limit on the distance of the sources. In the interaction, Delta resonances $\Delta(1232)^+$ are produced, which in turn decay into a nucleon and a pion.

$$p + \gamma_{2.7K} \rightarrow \Delta(1232)^+ \rightarrow n + \pi^+ \tag{2.4.2}$$
$$p + \gamma_{2.7K} \rightarrow \Delta(1232)^+ \rightarrow p + \pi^0 \tag{2.4.3}$$

The energy of the protons is thus quickly reduced to below 10^{20} eV after a few hundred Mpc, nearly independent of the initial energy. This is graphically represented in Figure 2.9. The energy loss length for other particles is also small at these energies. For example, nuclei lose their energy through photodisintegration, electrons through the inverse Compton effect and bremsstrahlung, and photons through pair production [32].

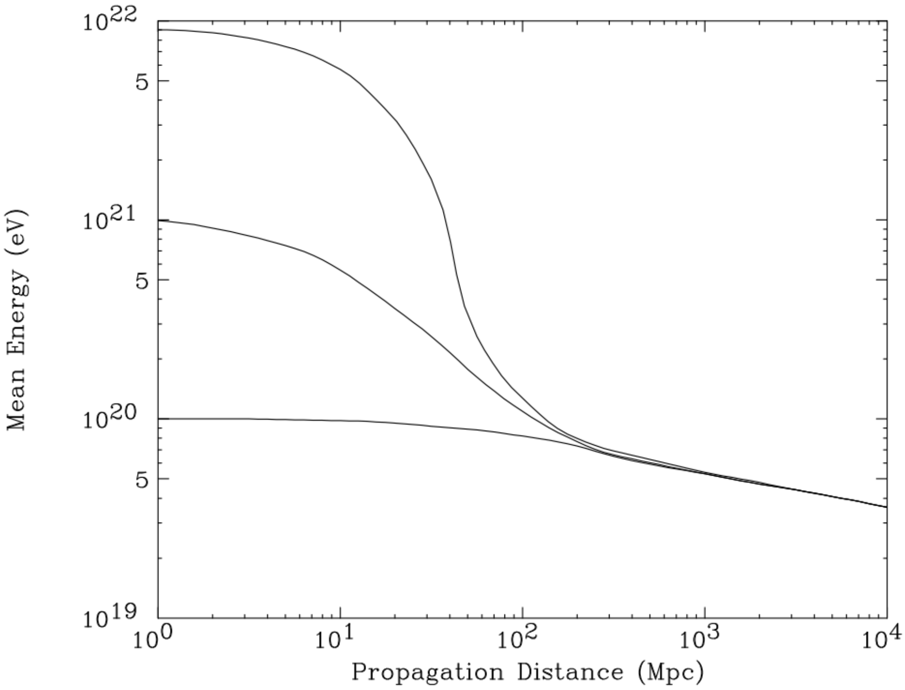

Figure 2.9. *The mean energy of a proton is plotted as a function of the propagation distance through the cosmic microwave background. It can be observed that in spite of different energies, the energy at a distance of a few 100* Mpc *is approximately equal and falls below* 10^{20} eV [33].

2.5 Extensive Air Showers

Around 1900, radioactivity, which had been recently discovered, was initially considered the cause of the discharge of electroscopes as a terrestrial source. Under this assumption, one expected lower ionization at higher altitudes. However, measurements of Theodor Wulf at the Eiffel Tower in 1910, showed that the ionization decreased slower than expected. New measurements, which requited higher altitudes, were conducted by Victor Franz Hess in a series of balloon flights in 1912. He discovered that ionization increases again after approximately one kilometer and proposed radiation originating from outside the atmosphere. He excluded the sun as the source, as there was no reduction in the radiation intensity during night or a solar eclipse. For his discovery of cosmic rays he was awarded the Nobel Prize in Physics in 1936. Further measurements in 1929 by Walther Bothe and Werner Kolhörster showed, through coincidence measurements, that the radiation they detected consists of penetrating, charged particles [34].

This radiation is described by extensive air showers. EAS are a cascade of particles initiated by a particle of non-terrestrial origin that interacts with the Earth's atmosphere. The primary particle that hits the Earth interacts mainly with nitrogen nuclei in the atmosphere, producing several secondary particles. These secondary particles in turn create more particles through interactions with the atmosphere, creating the cascade. However, this cascading effect does not go on endlessly, as the energy available is restricted by the energy of the primary particle. At the beginning, when the EAS penetrates the atmosphere the number of its particles increases, while the energy per particle decreases. After several interactions, the energy of a new particle, which is generally not evenly distributed among the generated particles, is too low to produce additional particles. The EAS will reach a maximum number of particles at a certain height, but it is more useful to describe the air shower through atmospheric depth, called X. The atmospheric depth, also called slant depth, is a measure of the actual material traversed rather than the length of the path. As such it is expressed in g/cm^2 and depends on the air density ρ and height h in the following way for vertical showers:

$$X(h) = \int_h^\infty \rho(h')dh' \tag{2.5.1}$$

For inclined showers with zenith angles below 60°, the curvature of the Earth can be neglected in the flat Earth approximation, and the slant depth can be approximated to be [35]:

$$X_{\text{inclined}}(h, \theta) \approx \frac{X(h)}{\cos\theta} \tag{2.5.2}$$

The slant depth of the shower maximum is called $X_{\max}$, which is an observable that provides information about the primary particle and its initial energy, as these, along with the rest of the air shower's development, depend heavily on the first interaction. Beyond this depth, the number of particles in the shower decreases again, as particles can, for example, be absorbed, until the particles reach the Earths surface or the shower dies out.

Typical air shower with a primary energy above of 10^{15} eV produce millions of secondary particles [26]. The particles of the air shower are located in a disk moving at approximately the speed of light along the straight shower axis towards the Earth's surface. The area of this disk reaches the order of square kilometers, with most of the particles concentrated in the middle of the disk.

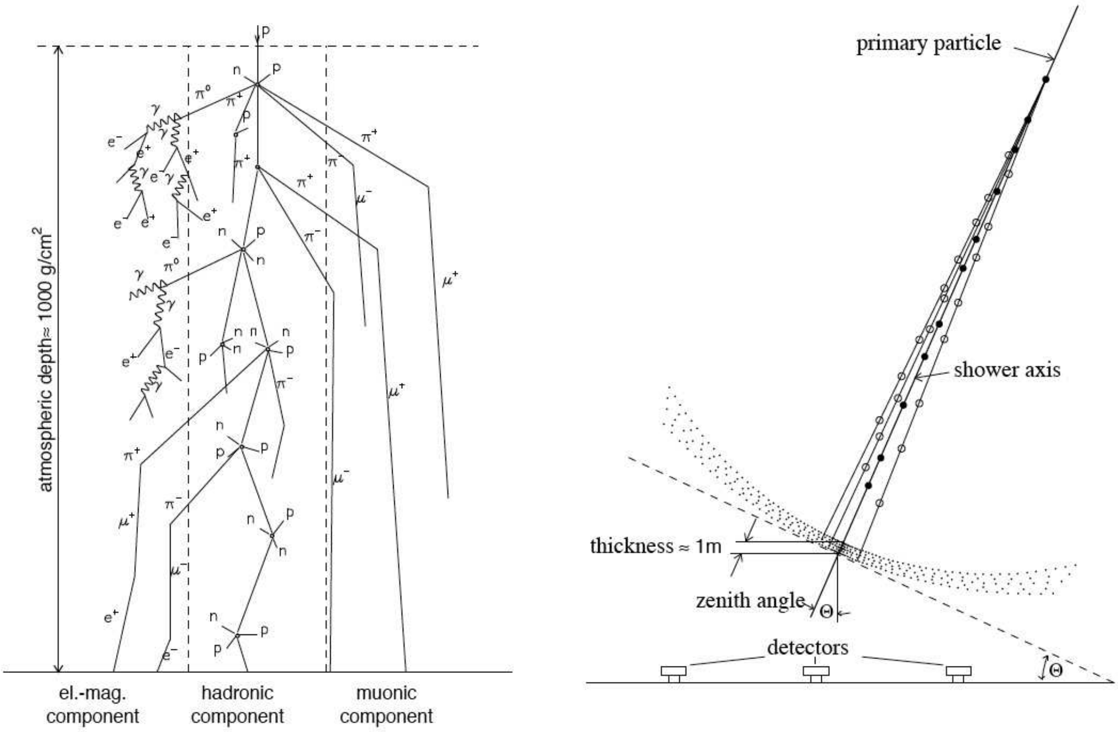

Figure 2.10. *On the left is the schematic structure of a proton induced air shower over an atmospheric depth of about* 1000 g/cm^2*. The particles produced by the interactions are divided into three components.*
In the figure on the right, the shower axis and the particle distribution are schematically shown. The dots represent particles and most of them are located near the shower axis. The disk of particles is widely extended and has a thickness of about 1*m* [36].

Components of an EAS

The particles that make up the air shower can essentially be divided into three different components. Hadrons form the hadronic component, muons the muonic component, and electrons, positrons, and photons the electromagnetic component.

The hadronic component arises from strong interactions, comprising hadrons, most of which are pions. The charged pions continue to interact strongly or electromagnetically, while the neutral pions, due to their shorter lifetime, decay into photons. Consequently, more and more energy from the hadronic component is redistributed into the electromagnetic and muonic components.

Muons are produced by the decay of charged mesons, such as pions. Most muons are initially generated at lower atmospheric densities, where the interaction length is longer, and thus the probability of decay is higher. The lifetime of muons is

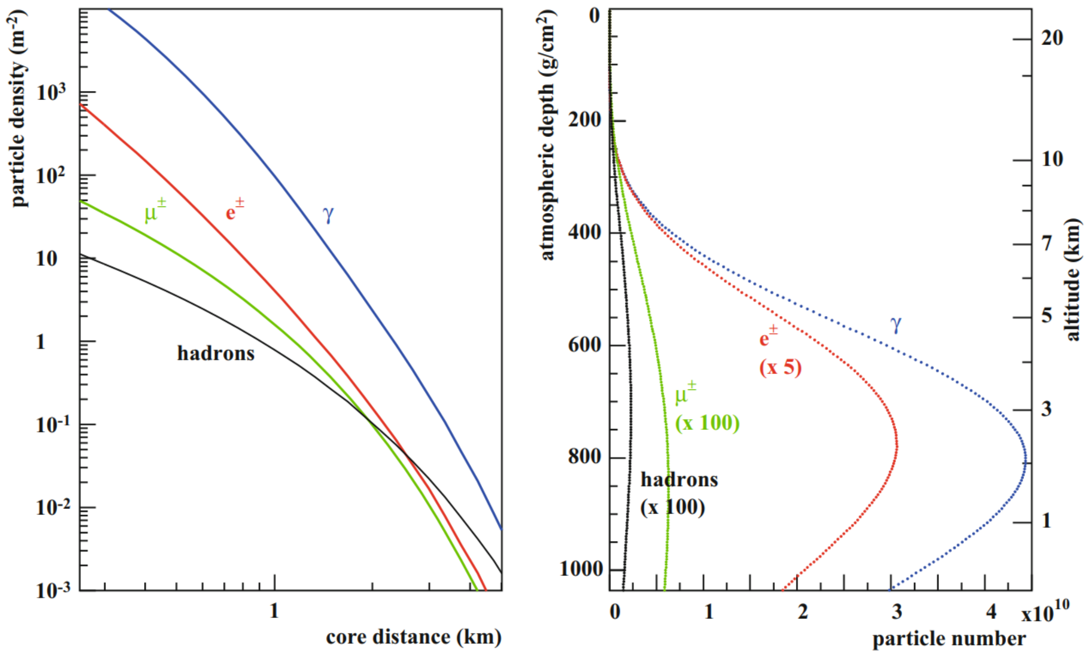

Figure 2.11. *Simulated number of particles corresponding to the different components. On the left is the lateral profile and on the right the longitudinal profile at an observation level of atmospheric depth* 870 g/cm^2*, corresponding to the altitude of the Pierre Auger Observatory* [37].

$\tau = 2.2\,\mu$s [38], but at high energies, muons can reach the Earth's surface due to relativistic time dilation, as they do not interact strongly. Muons account for about 80% of the detectable particles at ground level [26].

Compton and photoelectric effects can be neglected at high energies. The Heitler model provides a good simplification of the electromagnetic cascade, where after each interaction length, an electron radiates a photon, and a photon produces an electron-positron pair. The first photons are often generated by neutral pion decay and the electromagnetic component consists of all the different electromagnetic cascades.

Heitler Model

One model for an air shower is the simplified Heitler model, which only takes electrons, positrons and photons into account [35]. Electrons, positrons, and photons interact electromagnetically with the atmosphere. The photon decays into an electron positron pair through pair production while the electron and positron emit photons through bremsstrahlung:

$$\begin{aligned} \gamma + \text{nucleus} &\rightarrow e^+ + e^- + \text{nucleus} \\ e^\pm + \text{nucleus} &\rightarrow e^\pm + \gamma + \text{nucleus} \end{aligned} \tag{2.5.3}$$

In this toy model, the particles interact after a fixed interaction length λ, doubling the number of particles after each succession as the nucleus in 2.5.3 is not further considered and the transferred energy is neglected, while distributing the energy equally among the two particles. The model does only describe the particle shower until it reaches its maximum and one can find the following analytical forms for the atmospheric depth $X = n\lambda$, the number of particles $N = 2^n$, and the Energy per particle $E = \frac{E_0}{2^n}$, to describe the air shower:

$$N_{\max} = \frac{E_0}{E_c} \tag{2.5.4}$$

$$X_{\max} = \frac{\lambda}{\ln 2} \ln \frac{E_0}{E_c} \tag{2.5.5}$$

Here, E_c is the critical energy after which the energy is no longer sufficient to produce an electron-positron pair and therefore no new particles can be produced, ending the description of this model. Although the model is highly simplified, its predictions of the relation between the primary energy E_0 and $N_{\max}$, being proportional, and $X_{\max}$, being proportional to the logarithm, are qualitatively well described compared to EAS simulations.

Superposition Model for EAS initiated by Nuclei

A different model regarding air showers initiated by nuclei heavier than protons is the superposition model. The development of air showers initiated by a nucleus with a mass number A and energy E can be approximated by treating the primary nucleus as A independent nucleons each with the evenly scaled energy E/A. This can be done as the binding energy of the individual nucleons is much smaller than the overall energy [37]. The total shower is then described by the superposition of A subshowers. Qualitatively, the effect on $X_{\max}$ can be viewed through the Heitler model. Equation (2.5.5) shows that $X_{\max} \propto \ln(E_0/E_c)$, such that substituting the energy by E_0/A, will yield A subshowers, each developing earlier in the atmosphere with a smaller $X_{\max}$ given by:

$$X_{\max} \propto \ln\left(\frac{E_0}{AE_c}\right) \tag{2.5.6}$$

2.5.1 Pierre Auger Observatory

The Pierre Auger Observatory is an air shower experiment specifically designed to study UHE CR through indirect measurements. It is located near Malargue in the Argentinean province of Mendoza, and is currently one of the most powerful experiments, with over 500 scientists being part of the Pierre Auger Collaboration. It has an average elevation of 1,400 meters above sea level, corresponding to a mean atmospheric depth of 870 g cm^{-2}.

A key feature of the Pierre Auger Observatory is its hybrid design, which combines two independent types of detector systems to achieve high accuracy. In this approach, a surface detector (SD) employs over 1,600 water Cherenkov detectors, covering an area of $\sim 3,000$ km^2, while telescope stations oversee the area forming the fluorescence detector (FD). Having access to observing air showers through these complementary methods provides cross-checks and measurement redundancy [39, 40]. This section will briefly outline the two detector systems, while omitting extensions to the observatory and more technical aspects, such as the calibration, monitoring, data acquisition, or the reconstruction of air shower events. For a more detailed explanation, see for example [39].

Surface Detector

The SD consists of over 1,600 independent Cherenkov detectors. Each of these detectors works autonomously with a duty cycle of nearly 100%. These detectors are spread over an area of 3,000 km^2 with a distance of 1.5 km between each tank and are arranged in a hexagonal pattern. A single Cherenkov detector in the ground array of the SD is a cylindrical tank with a diameter of 3.6 m, which is filled with 12,000 l of purified water. The water functions as the detection medium, utilizing the emission of Cherenkov radiation caused by the transit of relativistic, electrically charged particles through the water.

Three photomultiplier tubes (PMT) are symmetrically installed per station to measure the Cherenkov radiation and convert it into an electric signal. The PMTs are powered by a battery that is charged by a solar panel mounted on the tank. The signals recorded in a single detector station are presented in units of vertical equivalent muon, which is defined as the signal measured by a station for a single muon passing vertically and centrally through the detector. The SD signal is sensitive to the number of muons as well as electrons and positrons in the EAS and can be used as an energy estimator based on hybrid events, measured by both the SD and FD. A commonly used observable is S(1000), which is the total signal at a distance of 1 km from the shower core.

Fluorescence Detector

Charged particles in the air shower can excite nitrogen molecules in the air, depositing some of their energy. When an excited nitrogen molecule returns to the ground state, it emits fluorescence light in the ultraviolet range. Each of the four FD sites is equipped with six optical fluorescence telescopes, that measure the fluorescence light.

The extensive air showers longitudinal profile of the deposited energy in the atmosphere, can be inferred by the FD, due to the dependency of the amount of fluorescence light on the deposited energy. The energy of the primary particle initiating the EAS can be derived from this profile, if the shower fully developed in the FDs field of view. However, one has to account for the invisible energy component attributed to neutrinos and high energy muons, which don't deposit their energy in the atmosphere.

One drawback of the FD is its low duty cycle of about 13% compared to the SD. This is because measurements are limited by the light conditions, as it can only observe the dim fluorescence light on clear, moonless, and cloudless nights.

3. Air Shower Simulations

Using data from air shower simulations and comparing them with actual measurements has proven to be a useful tool for testing theories. An example of this was briefly discussed in the previous chapter for the mixed mass composition of CR.

A problem that was also briefly addressed with this approach is the uncertainty of hadronic interactions at ultra high energies, as there are no accelerator experiments capable of providing clear insight at these energies. As such, there are different kinds of extrapolated hadronic interaction models available. The simulations in this work are based on SIBYLL 2.3d [41, 42], although other models, such as EPOS LHC or QGSJET-II-04, could have been used.

Two air shower simulation programs are discussed in this chapter. Section 3.1 briefly discusses CONEX, which was used for comparison. CORSIKA, in which the LV processes were implemented as part of this thesis, is detailed in Section 3.2.
The LV processes were implemented separately in a modified version of the simulation programs to show the effect of the constituents on air showers, as well as simultaneously.

For $\kappa < 0$, these include the photon decay and the increased lifetime of neutral pions. The plots in this work shown in chapter 5 use the following naming convention: Both processes together are labeled as modified in red, photon decay is labeled as photon modified in cyan, and the change of the neutral pion lifetime is labeled as pion modified in green.

For $\kappa > 0$, the complete implementation is plotted in blue and labeled VCh modified. The VCh radiation of electrons and positrons is also implemented individually and labeled VCh modified ($e^{\pm}$) in magenta.

In the absence of partial modifications, the κ value is displayed as the label for complete modifications, as well as $\kappa = 0$ for the unmodified case.

3.1 CONEX

CONEX is a fast simulation program, which uses a hybrid approach, simulating EAS in one dimension [3, 4]. At high energies, early in the shower development, it uses Monte Carlo simulations. Particles that fall below an energy threshold are instead treated by cascade equations. Compared to a full three-dimensional MC approach, this significantly speeds up the computation time. This makes CONEX useful for studies where large statistics at ultra-high-energies are required, and where only the longitudinal profile is of interest.

CONEX simulations have already been used to study LV, as shown in [6, 22]. The LV was implemented in the MC part of the simulations, such that the energy threshold for cascade equations needed to be below the energy thresholds for LV given by Equation (2.3.11) and (2.3.6).

Without setting limits on κ, one can plot observables as a function of κ. Figure 3.1 shows results of CONEX simulations with the version 2r7.50 comparing the number of muons for different κ values at ground level relative to the unmodified simulations. Qualitatively, it can be seen that a value closer to zero shifts the onset, where the modified and unmodified curves differ, to higher energies.

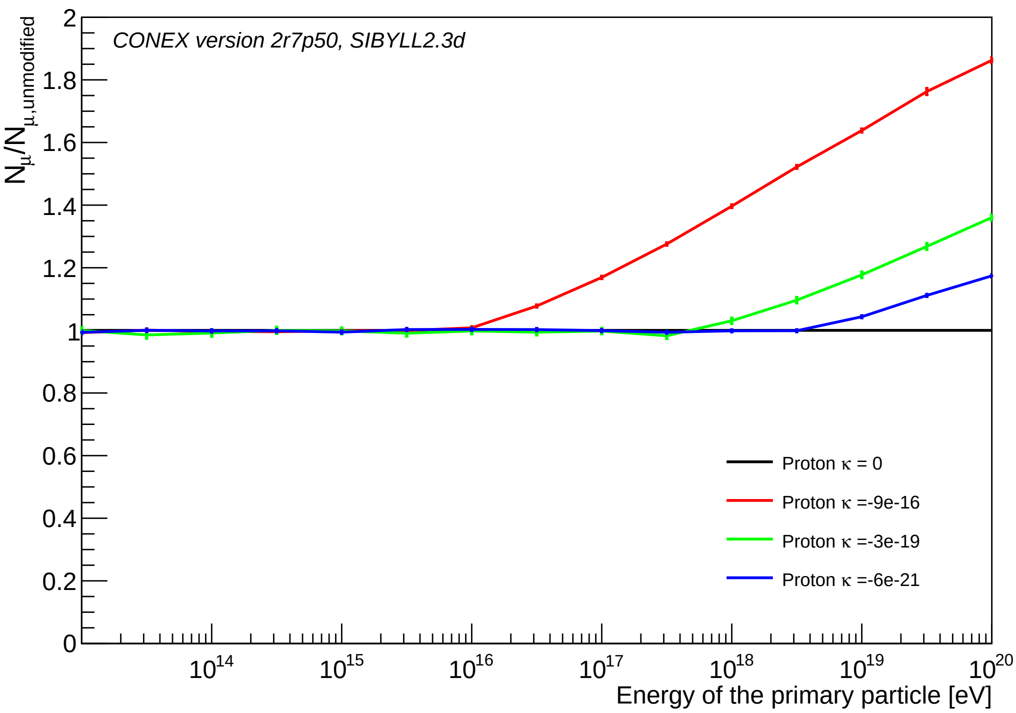

Figure 3.1. *Number of muons at ground level in dependence of the primary energy of a primary proton derived from simulations for different κ values scaled to the unmodified case. The onset shifts for κ values closer to zero to higher energies as $E^{\pi^0}_{cut}$, given by equation* (2.3.12)*, increases.*

3.2 CORSIKA

CORSIKA, which stands for COsmic Ray SImulations for KAscade, is a widely used air shower simulation program [7]. As the name suggests, it was originally designed for the KASCADE experiment in Karlsruhe. Now it is a commonly used program that is versatile, suitable for a wide range of applications, producing detailed air showers simulations.

In contrast to CONEX, CORSIKA provides a full three dimensional MC simulation, allowing for a more detailed study, where observables connected to the lateral distribution can be used. Secondary particles in the air shower simulation are monitored until their decay, interaction, or until they fall below a defined energy threshold.

CORSIKA allows the customization of the simulation by a variety of configurations [7, 43]. As it was the case for CONEX, this includes for example the different hadronic interaction models. Here, as mentioned above, SIBYLL2.3d has been used for CONEX as well as CORSIKA. The steering parameters controlling the behavior of the simulations are written in an input card for CORSIKA, which will be discussed in a following section.

The important observable X_{max} is obtained in CORSIKA through a fit of the longitudinal shower profile using the Gaisser-Hillas function. Nevertheless, in certain instances, especially when double maxima occur in the profile, the fit may fail. Simulations with unphysical results for X_{max} are discarded. Additionally, for consistency, only values up to 2500 g/cm^2 are considered in both CORSIKA and CONEX simulations.

Version 7.7500 of CORSIKA is used for the simulations performed in this work. A new version CORSIKA 8, which is based on C++ instead of FORTRAN is currently under development [44].

3.2.1 Implementation

One option that CORSIKA offers is to use CONEX up to a certain energy after which the particles are transferred to CORSIKA for the full three dimensional simulation. This does not affect observables such as the moments of $X_{\max}$ and is sufficient for this thesis. Even though CORSIKA uses CONEX for parts of the simulation, I will refer to those simulations as CORSIKA, while CONEX simulations refer to CONEX-only simulations.

As such, the LV can be implemented similarly to the modified standalone MC part of the CONEX code, when the energy thresholds are chosen such that particles are not returned to CORSIKA when their energy is above VCh or the photon decay threshold energy, depending on whether κ is positive or negative. As the length scales in Figure 2.3 and 2.4 are in the context of air showers quasi instantaneous, they are implemented as instantaneous. The FORTRAN code for the modifications is given in Appendix B.

For positive κ, this introduces an additional interaction mode above the VCh energy threshold, where electrically charged particles as well as neutral hadrons, as they are made of electrically charged constituents, radiate photons, with a randomly drawn energy, given by the emission rate in Equation (2.3.7).

For negative κ, the photon decay is handled in the EGS4 part. A photon with an energy above the decay threshold will be replaced by an electron and a positron. The energy for the electron will be randomly drawn from an energy spectrum, while the positron's energy is determined through energy conservation, being the photon's energy minus the electron's. The neutral pion decay width is multiplied by the factor g, which is given by Equation (2.3.15).

3.2.2 Input Card

The behavior of CORSIKA simulations is governed by a set of steering parameters, which are defined in an input card. The choice of options can significantly impact the results, especially at the highest energies. An example of a CORSIKA input card is provided below, followed by a short explanation of some steering parameters. For a more detailed description, see the CORSIKA user guide [43].

```
RUNNR   1                               run number
EVTNR   1                               number of first shower event
NSHOW   1                               number of showers to generate

PRMPAR  5626                            particle type of prim. particle (14 = proton)
ERANGE  1E11 1E11                       energy range of primary particle (GeV)
THETAP  0.  0.                          range of zenith angle (degree)
PHIP    0.  0.                          range of azimuth angle (degree)

SEED    100000  0       0               seeds for random number sequences
SEED    100000  0       0
SEED    100000  0       0
SEED    100000  0       0
SEED    100000  0       0
SEED    100000  0       0
SEED    100000  0       0
SEED    100000  0       0

OBSLEV  1452.E2                         observation level (in cm)
MAGNET  20.1 -14.2                      magnetic field Pierre Auger Observatory
SIBYLL  T 0                             use SIBYLL routines
SIBSIG  T                               use SIBYLL cross-sections
SIBCHM  T                               turn Charm production in SIBYLL on
HADFLG  0  0  0  0  0  2                flags hadr.interact.&fragmentation
ELMFLG  T   T                           em. interaction flags (NKG,EGS)
STEPFC  1.0                             mult. scattering step length fact.
RADNKG  200.E2                          outer radius for NKG lat.dens.distr.
LONGI   T   10.   T  T                  longit.distr. & step size & fit & out
MUMULT  T                               muon multiple scattering angle

THIN    2.3e-07   23000  80.e2          thinlev, maxweight, innerradius
THINH   1.  100.                        thinrat hadronic, weightrad hadronic
ECUTS   0.3  0.3  0.003  0.003          energy cuts for particles

CASCADE F F F                           flags for simplified CONEX threshold management
CX2COR  2.3e+04 2.3e+04 2.3e+04 0.      thresholds for transition from CONEX to CORSIKA

CONEX   2e-07 2e-07 2e-07               energy fractions above which particles are treated by MC methods
MUADDI  F                               additional info for muons
MAXPRT  0                               max. number of printed events
PAROUT  T  F                            print output tables
DATBAS  F                               write out database file

DIRECT  ./                              output directory
DATDIR  /data/auger7/LorentzViolation/CORSIKA/CompiledCORSIKAVersions/Conex/corsika-77500-modified/run/
EXIT
```

Figure 3.2. *CORSIKA input card for an iron initiated air shower simulation with a primary energy of* $E = 10^{20}$ eV *using the CONEX code at high energies and transitioning to CORSIKA at energies below* 2.3 TeV.

In this thesis, only vertical showers with a zenith angle (THETAP) of 0 degree, are simulated. In order to enable the reproducibility of results, the random number sequences are initialized with explicit seeds (SEED). The observation level (OBSLEV) as well as the magnetic field (MAGNET) have been set to values corresponding to the Pierre Auger Observatory [45]. To reduce computation time, especially at the highest energies, CORSIKA employs a thinning mechanism, which is controlled by the THIN keyword. In the simulation, weights are assigned to secondary particles to reduce the number of tracked particles and consequently reducing computation time and output file sizes. CORSIKA performs thinning for secondary particles below the specified energy fraction of the primaries energy. Additionally, a maximum weight can be set, and the area surrounding the shower core, where thinning will occur, is determined by the radius parameter RMAX. In this input card, an energy fraction of 2.3×10^{-7} was chosen, such that thinning takes place below the energy threshold of photon decay in case of the modified CORSIKA code, which is given by Equation (2.3.11). The maximum weight is chosen to be the product of the energy fraction and the primary energy as suggested in [43], while the radius was set to 80 m around the shower core.

Figure 3.3 shows the time needed for a single air shower simulation at an energy of 10^{20} eV for a proton as a primary particle. It illustrates the effectiveness of the thinning algorithm, by comparing the computation time for the unmodified CORSIKA code using a thinning of 10^{-5} compared to the modified CORSIKA code using a thinning level of 2.3×10^{-7}.

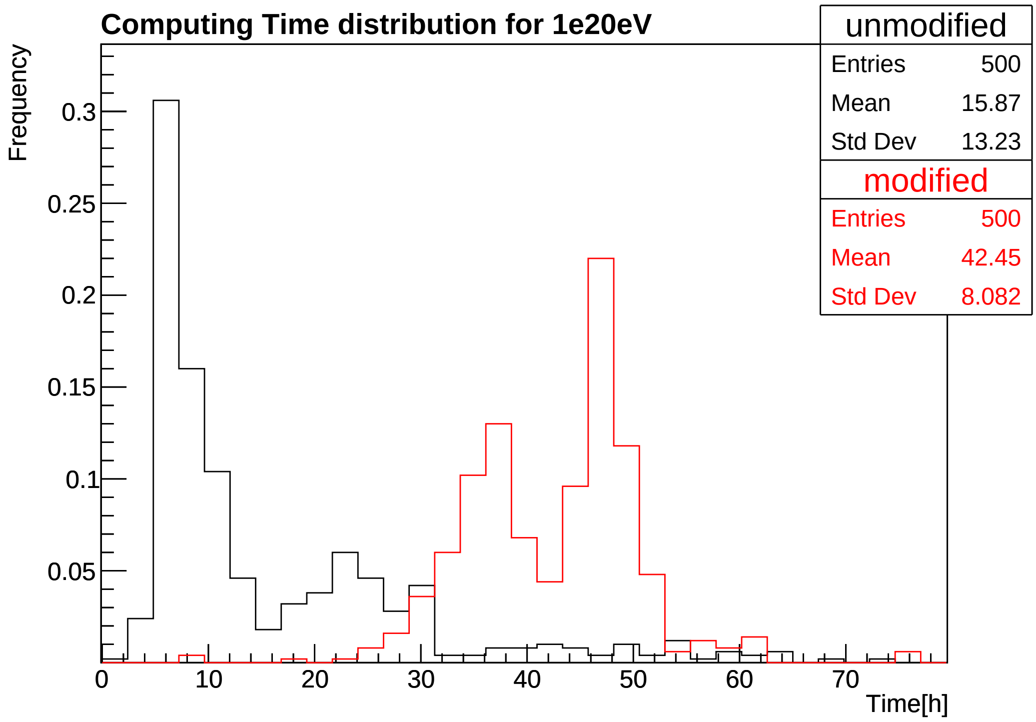

Figure 3.3. *Comparison of two histograms depicting the different computing times for proton initiated air showers with different thinning levels with a primary energy of $E = 10^{20}$ eV.*

On average, simulations with the increased thinning level of 10^{-5} (in black), are finished faster by a factor of around 2.7. However, it can also be seen that even with the increased thinning, simulations take a considerable amount of time, especially since there are quite a few outliers, resulting in a large standard deviation.

4. Limits on Lorentz Invariance Violation

From a theoretical standpoint, the LV parameter κ is restricted to the half-open interval $(-1, 1]$, so that microcausality and unitarity hold.

The values κ can take were limited even more by observing UHE CR and photons, which is discussed in Section 4.1. The parameter was even further restricted by indirect measurements in combination with air shower simulation. In Section 4.2 the limit was obtained by a comparison of the average atmospheric depth of the shower maximum under the conservative assumption of a pure proton composition of CR. The best limits on LV up to date are presented in Section 4.3, where the shower-to-shower fluctuations and a mixed mass composition are additionally included in the analysis.

This chapter is motivated by the improvement of the limits by including additional observables, which was the incentive to implement the LV effects into CORSIKA, to gain access to new observables connected to the lateral distribution of an EAS.

4.1 Inferred from Observation of Particles

A two-sided bound was set on κ using measurements of high energy CR and gamma rays. The argument for both positive and negative κ is similar. For the upper limit, if a CR with energy E is observed, it implies $E < E_{\text{thresh}}^{\text{VCh}}(\kappa)$. The threshold energy for VCh radiation must be higher, as it otherwise would not have reached Earth without losing energy by emitting VCh radiation. Together with Equation (2.3.6) an upper bound on κ can be set, if the particle type is identified. Otherwise a conservative estimate can be calculated due to the mass dependency.

A hybrid event from the Pierre Auger Observatory was used, which had a primary energy of $E = 212$ EeV, and the mass of an iron nucleus $m = 52$ GeV was conservatively chosen, obtaining the following bound [20]:

$$\kappa < 6 \times 10^{-20} \text{ at 98\% CL} \tag{4.1.1}$$

The same logic applies to the lower limit. If a photon with an energy E is detected, the threshold energy for photon decay $E_{\text{thresh}}^{\gamma}(\kappa)$ has to be higher, because the photon otherwise would have decayed into an electron-positron-pair. From Equation (2.3.11) the κ value can be determined. With the High Energy Stereoscopic System (HESS) gamma-ray photons with energies above 30 TeV have been detected, leading to the two-σ lower bound of [20]:

$$\kappa > -9 \times 10^{-16} \text{ at 98\% CL} \tag{4.1.2}$$

Searches for UHE photons are of particular interest to study direction dependencies, but could also incidentally improve this limit on LV. So far no events could be unambiguously identified as photons at these energies.

4.2 Comparison of $\langle X_{\text{max}} \rangle$ for a pure Proton Composition

Figure 4.1 shows the mean atmospheric depth of the shower maximum $\langle X_{\text{max}} \rangle$ of simulations based on modified CONEX code together with data measured at the Pierre Auger Observatory plotted against the primary energy of the particle inducing the air shower. The simulations are initiated by a proton as a primary particle and made for different κ values. This approach utilizes the effect of secondary photons produced in the EAS. Protons were chosen as a conservative choice to compare to the Auger data. The smaller values of $\langle X_{\text{max}} \rangle$ would result in stronger bounds on κ.

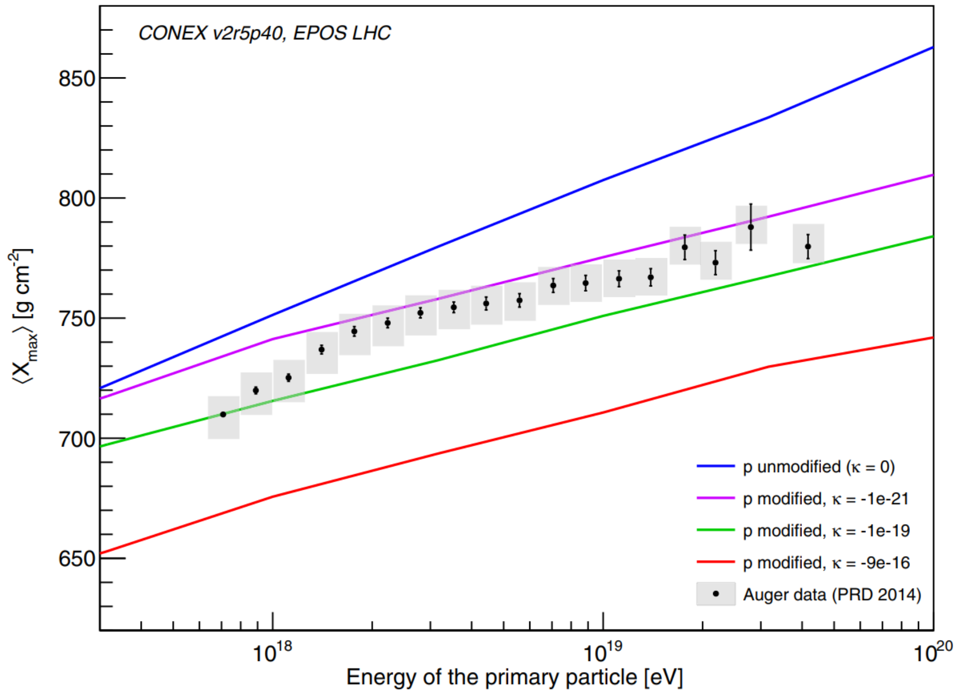

Figure 4.1. *Comparison of simulated $\langle X_{max} \rangle$ values of proton initiated EAS as a function of the primary energy for different κ with the measured values of $\langle X_{max} \rangle$ by the Pierre Auger Observatory. The systematic uncertainties of the measurements are indicated by the gray boxes around the data points* [5].

It can be seen that for a value of $\kappa = -9 \times 10^{-16}$, which is the lower limit based on the observation of a high energy photon, the simulation and the measured data are not in agreement.

Based on $\langle X_{\max} \rangle$ alone, an improved bound can be obtained through comparison of simulations and measurements of the Pierre Auger Observatory.

$$\kappa > -3 \times 10^{-19} \text{ at } 98\% \text{ CL} \tag{4.2.1}$$

For this bound, EPOS-LHC simulations were used and a conservative systematic uncertainty of 20 g cm^{-2} was assumed, accounting for uncertainties related to the choice of the hadronic interaction model. This improved the limit compared to the previous one by a factor of 3000 [5].

4.3 Mixed Mass Composition and Inclusion of $\sigma(X_{\max})$

By the inclusion of the shower-to-shower fluctuations observable $\sigma(X_{\max})$ and waiving the conservative assumption of a pure proton composition, bounds on κ were improved once more. This limiting factor was overcome because, in contrast to $\langle X_{\max} \rangle$, $\sigma(X_{\max})$ is hardly dependent on κ. This allowed, for a given value of κ, to reject compositions that might reproduce one of the observables, but not both at the same time.

Since the exact composition of CRs is unknown, combinations of simulations with representative elements of its mass range were performed to imitate the EAS. Sets of air shower simulations vary by their relative contribution of each primary element. Figure 4.2 shows the results for a set primary energy and different values of κ, which form an umbrella-like shape. Only combinations on the outer border were investigated as all other combinations will lie within the shape.

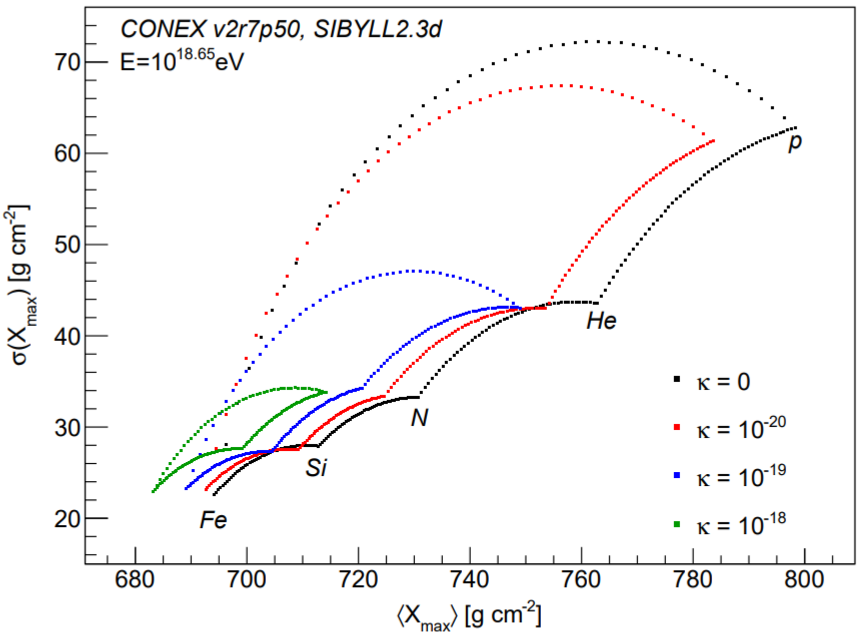

Figure 4.2. *Comparison of $\langle X_{max} \rangle$ obtained by CONEX simulations for different combinations of primary particles and different κ values. The corners are pure compositions with primaries as indicated (proton, helium, nitrogen, silicon, iron). Particles above the VCh radiation threshold are excluded. For a given value of κ, the corresponding umbrella encloses all values that are permitted by arbitrary combinations of those primaries* [22].

An overlap of the umbrella-like shape and the 2D-confidence interval from the Auger data means that they are in agreement for the energy. If there is no overlap, the κ value can be excluded. Figure 4.3 shows on the left a positive κ, where data and simulations are in disagreement for an energy bin and on the right side the same for a negative κ. It should be noted here, that for $\kappa = 3 \times 10^{-20}$ protons are already excluded at an energy of $E = 10^{18.65}$ eV through the energy loss of VCh radiation, and as such do not appear anymore in the left plot.

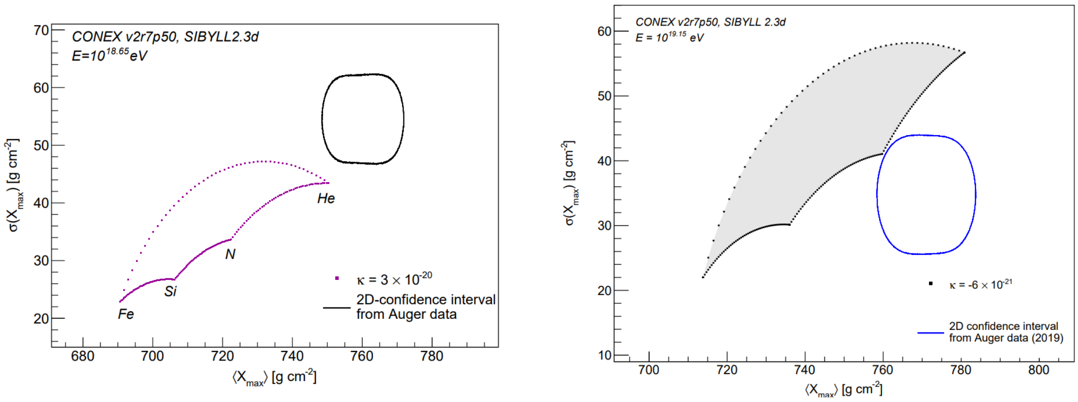

Figure 4.3. *Comparisons of $\langle X_{max}\rangle$ and $\sigma(X_{max})$ between LV simulations and the 2D confidence interval obtained by measurements of the Pierre Auger Observatory* [22, 6].

Up to date, these are the best limits on κ:

$$3 \times 10^{-20} > \kappa > -6 \times 10^{-21} \text{ at } 98\% \text{ CL} \tag{4.3.1}$$

The upper limit was improved by a factor of 2 and the lower limit by a factor of 50 compared to the previous bounds [6, 22]. To infer this strict lower bound from the observation of a photon, would thereby require a photon with an energy $E \gtrsim 9.3$ PeV.

Further improvements may be possible by the inclusion of additional observables like the signal size of the ground array. On the simulation side this calls for 3-dimensional simulations, which can be performed with CORSIKA.

5. Results

This chapter presents the results of the simulations performed by CORSIKA with the modified CONEX code, where the effects of LV were implemented.

The first results shown here focus on key observables such as the average atmospheric depth of the shower maximum $\langle X_{\max} \rangle$ and the shower-to-shower fluctuations $\sigma(X_{\max})$, which were used to determine the most stringent bounds at the time of writing, as discussed in the previous chapter. Additionally, the number of muons at ground level N_μ, normalized to the unmodified simulation results, can be compared to the simulations made with CONEX. The influence of the implemented LV effects - VCh radiation for positive κ as well as photon decay and the increased lifetime of neutral pions for negative κ - will be analyzed for these observables in Section 5.1.

In addition to the observables available to a 1-dimensional air shower simulation, results for particle densities at ground level are presented in Section 5.2. For example the muon density, 1 km from the shower core, will be discussed, as it is correlated to the commonly used $S(1000)$ observable at air shower experiments. These observables connected to the lateral distribution give new insights on the overall shower development for the LV theory discussed in this thesis and might be used in the future, together with detector simulations, to improve existing limits.

5.1 Comparison to CONEX

The following sections detail the results from CORSIKA simulations also available to 1-dimensional simulations and compares them to simulations made with the CONEX simulations.

5.1.1 Results for $\langle X_{\mathbf{max}} \rangle$

Figure 5.1 shows the average atmospheric depth of the shower maximum $\langle X_{\mathrm{max}} \rangle$ as a function of the primary energy for the CORSIKA simulations. The continuous lines correspond to air showers initiated by a proton, while the dashed line corresponds to iron primaries.

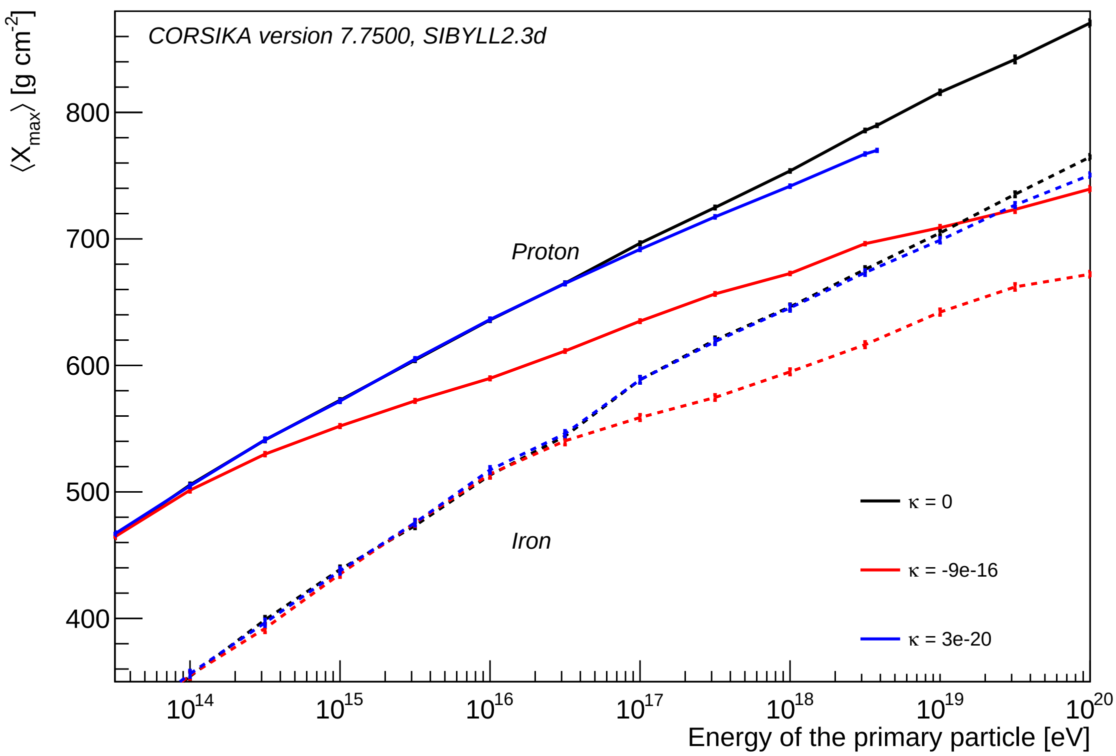

Figure 5.1. *Simulated values using CORSIKA of $\langle X_{max} \rangle$ as a function of the primary energy of the initiating particle. Proton and iron were used as primary particles and three different cases for κ are shown. In case of negative κ simulations were done for a value of -9×10^{-16} and for positive κ with a value of 3×10^{-20}.*

For the simulations, only the statistical uncertainties are displayed, while systematic uncertainties like the choice of the hadronic interaction model are not taken into account. Here, simulations were performed using SIBYLL2.3d, which generally produces higher $\langle X_{\mathrm{max}} \rangle$ values than EPOS LHC or QGSJET. The systematic uncertainties corresponding to the choice of the interaction model are not relevant in this work, since the simulation results won't be compared to simulations made with different models, as both CONEX and CORSIKA simulations are performed using SIBYLL2.3d.

Without a side by side comparison, one can already see in Figure 5.1 that the modified simulations behave generally as expected. The value of -9×10^{-16} was chosen for comparison. It was a previous limit on LV obtained by observation of high energy photons and its absolute value is large enough to see the difference compared to the unmodified simulations at relatively low energies, around 10^{14} eV. Therefore, simulations at the highest energies are not necessary, but are included for completeness for the modified case, as time allowed for some shower simulations at the highest energies. It should be mentioned here, that the simulated value for iron at 10^{20} eV is biased as only about one third of the simulations, which finished within 14 days computation time were taken into account. Compared to the unmodified case, the expected values for both modified cases of $\langle X_{\mathrm{max}} \rangle$, is lower, which will be explained in more detail in the next sections. This is done for positive and negative κ separately, also showing the partial modification and their contribution to $\langle X_{\mathrm{max}} \rangle$, making it more readable.

Positive Value of κ

Figure 5.2 shows $\langle X_{\mathrm{max}} \rangle$ for a positive κ value of 3×10^{-20}. The top plot shows proton initiated simulations, while the simulations for the bottom plot were performed with a primary iron particle. The continuous lines correspond to the new simulations made with CORSIKA, while the dashed line are simulations performed by standalone CONEX. Three cases are differentiated, namely unmodified, VCh modified ($e^{\pm}$), which includes only the Cherenkov radiation of electrons and positrons, and VCh modified, which also includes the Cherenkov radiation of hadrons. For positive κ, the maximum energy of the primary particle initiating the air shower, depends on its mass, as seen in Equation (2.3.6). Particles above the energy threshold are excluded as discussed in the previous chapter. For protons, the highest primary energy for which simulations were performed is $E = 10^{18.58}$ eV. In contrast, the iron energy threshold is above $E = 10^{20}$ eV, which is the highest primary energy for simulations in this thesis.

The average slant depth of the shower maximum $\langle X_{\mathrm{max}} \rangle$ decreases for the VCh modified cases. It can also be seen in the proton initiated plot that the main part of the reduction is due to the electron and positrons radiation of Cherenkov photons, as values for both modifications are with regards to their statistical errors equal. This isn't surprising either, as most particles in an air shower are electrons and positrons. The reduction can also qualitatively be explained by the Heitler toy model. The electromagnetic shower is contracted as electrons and positrons above the threshold energy radiate more than one photon at each interaction step. Through this contraction the maximum number of particles will be reached at a lower slant depth.

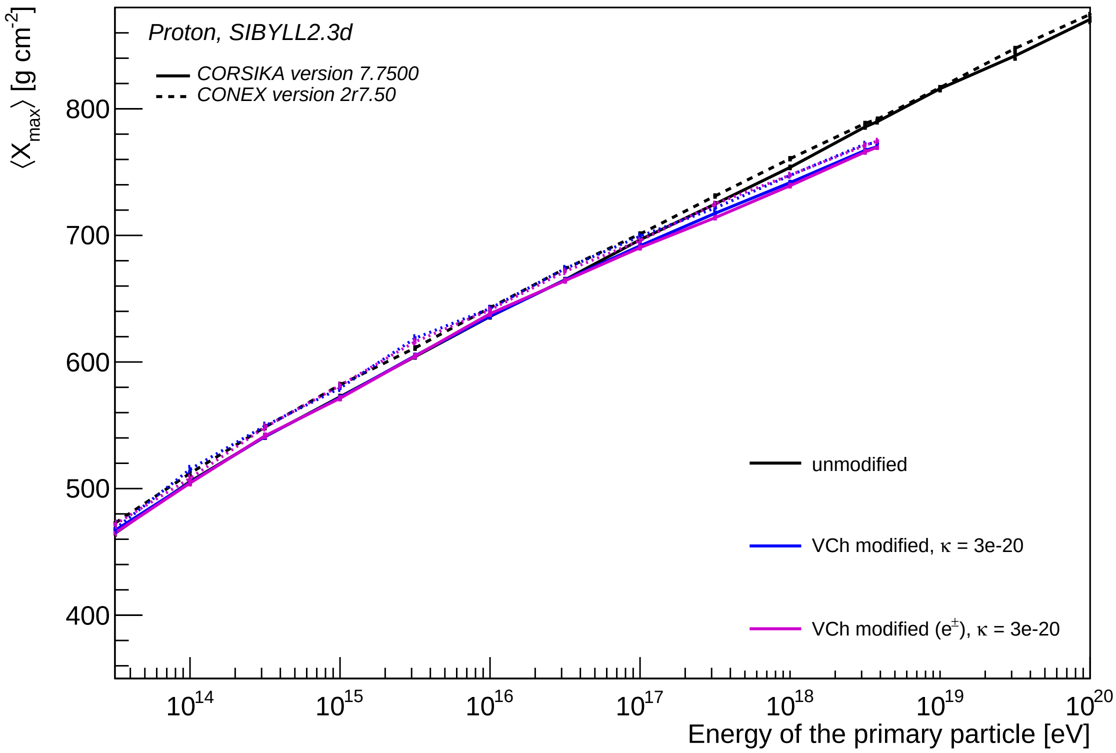

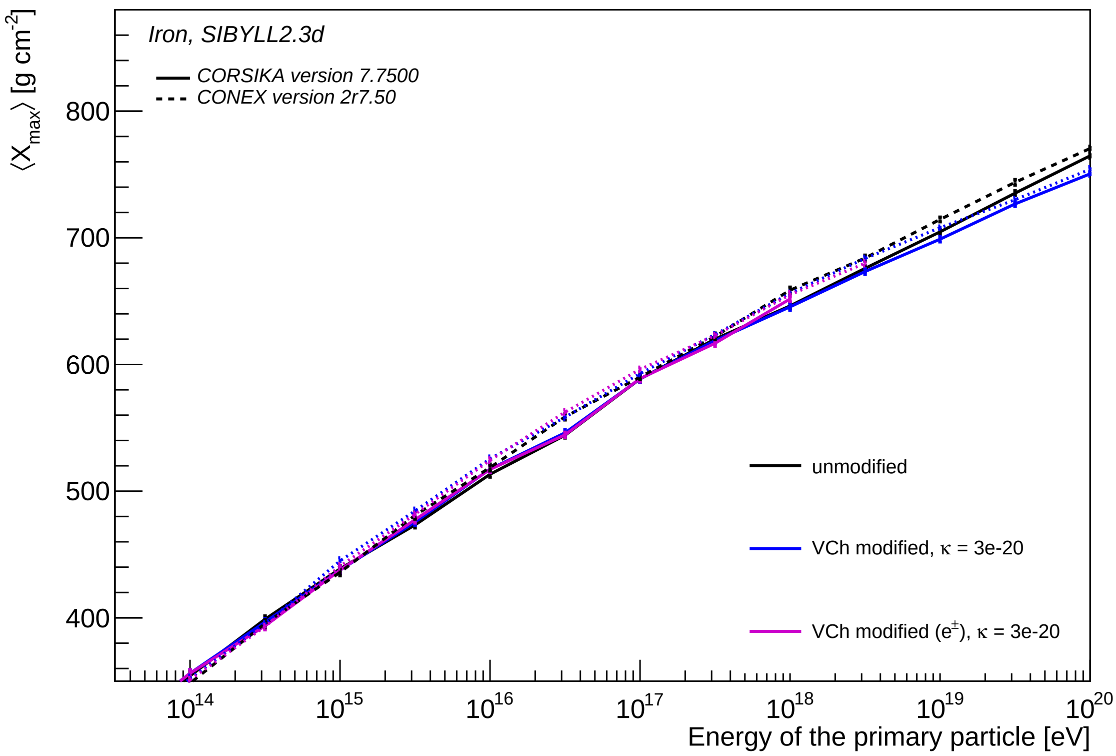

Figure 5.2. *Simulated values of $\langle X_{max} \rangle$ as a function of the primary energy of the initiating particle for the unmodified case and for a κ value of 3×10^{-20}. CORSIKA simulations are shown by the solid lines, while CONEX simulations are shown with a dashed line. Protons were used as the primary particle for the top plot and iron for the bottom plot.*

The threshold energy for electrons and positrons, as given by Equation (2.3.6), is around 2.1 PeV. For air shower simulations initiated by such a primary particle, one expects the trend of the reduction to be visible after this energy, when enough electrons and positrons will be above the VCh threshold. For other primary particles, the difference compared to the unmodified case starts at higher energies, as particles starting the electromagnetic subshowers will only have inherited a part of the primary particles energy, meaning that at the same primary energy there are fewer electrons and positrons above the VCh threshold energy. For primary protons, the reduction compared to the unmodified simulations is noticeable at energies around 10^{17} eV, while for iron the trend starts at around 10^{19} eV. Iron has a mass number of 56, such that the superposition model for EAS initiated by nuclei approximates the iron nuclei as 56 protons with an evenly scaled primary energy. This means the expected primary energy above which $\langle X_{\mathrm{max}} \rangle$ will be roughly 56 times higher for primary iron compared to protons, which is roughly what can be seen.

Negative Value of κ

Figure 5.3 shows $\langle X_{\mathrm{max}} \rangle$ for a negative κ value of -9×10^{-16}. The plots show besides the unmodified and modified cases, also the partial modifications of photon decay in cyan and increased lifetime of neutral pions in green. For $\kappa = -9 \times 10^{-16}$ the threshold energy for the photon decay and the energy above which neutral pions become stable are given by equations (2.3.11) and (2.3.12):

$$E^{\gamma}_{\mathrm{thresh}}(-9 \times 10^{-16}) \approx 2.4 \times 10^{13} \text{ eV} \tag{5.1.1}$$

$$E^{\pi^0}_{\mathrm{cut}}(-9 \times 10^{-16}) \approx 3.2 \times 10^{15} \text{ eV} \tag{5.1.2}$$

Both partial modifications result in a reduction of the average slant depth of the shower maximum $\langle X_{\mathrm{max}} \rangle$ as a consequence above these energy thresholds, for proton initiated air showers earlier than for iron initiated ones, as discussed for positive κ. The pion modification has the least effect on $\langle X_{\mathrm{max}} \rangle$, while the main part of the reduction follows from the photon decay. The reduction for the pion modified case starts when enough neutral pions become stable or their lifetime is long enough, such that hadronic interactions are likely. In that case, they initiate electromagnetic subshowers later in the shower development with less primary energy, as they do not decay into two photons but distribute their energy in a hadronic interaction. The reduction based on the photon decay can again be viewed by the Heitler model as a contraction of the electromagnetic shower. Since the decay was implemented as instantaneous, this means instead of radiating a photon at each interaction step in the toy model, electrons and positrons would instead produce an additional electron-positron pair. In short, the number of particles at each step would triple instead of doubling, leading to the contraction. Due to the large number of electromagnetic particles in the overall shower, this also leads to the reduction of $\langle X_{\mathrm{max}} \rangle$ of the shower as a whole.

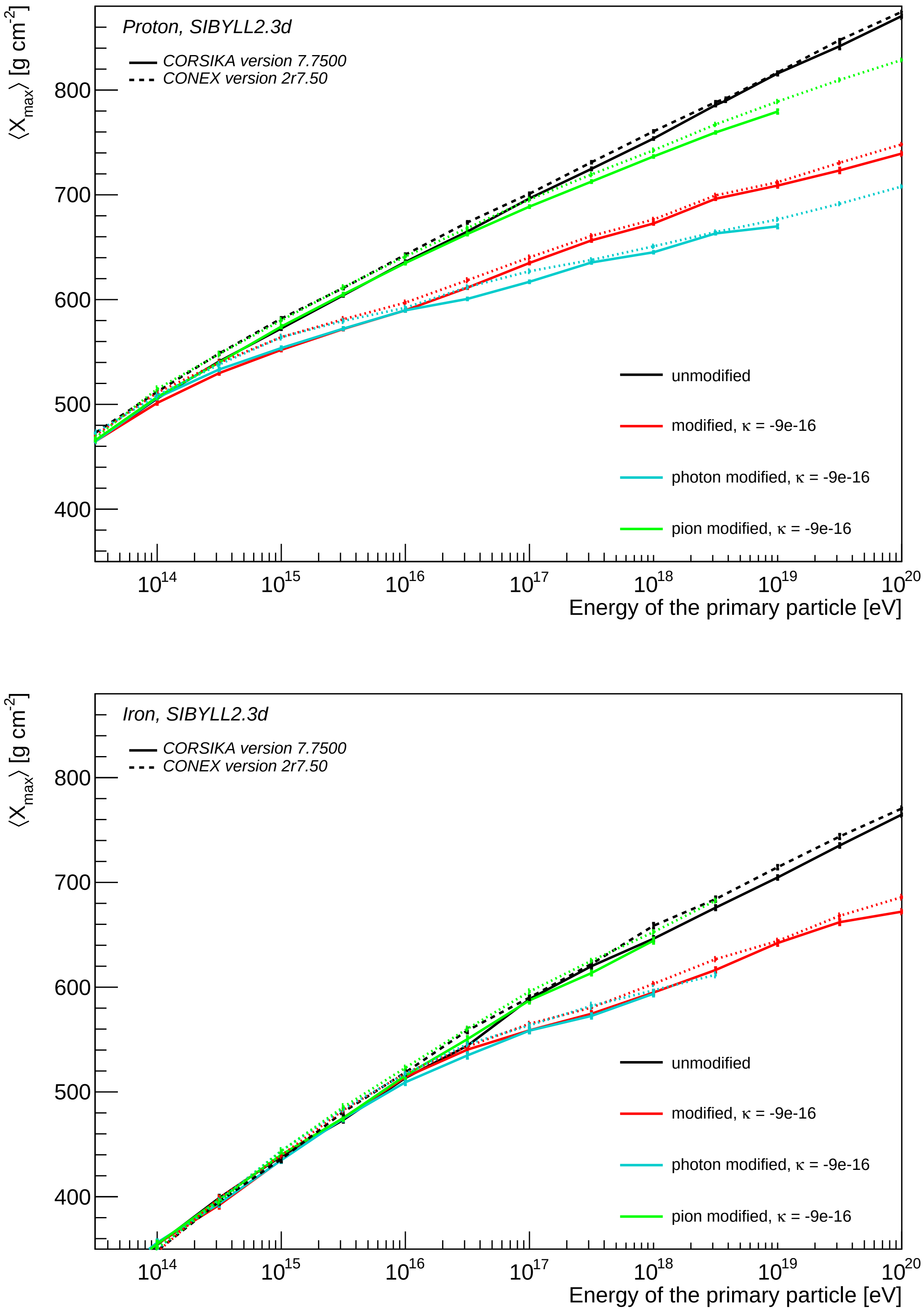

Figure 5.3. *Simulated values of $\langle X_{max} \rangle$ as a function of the primary energy of the initiating particle for the unmodified case and for a κ value of -9×10^{-16}. CORSIKA simulations are shown by the solid lines, while CONEX simulations are shown with a dashed line. Protons were used as the primary particle for the top plot and iron for the bottom plot.*

Interestingly, the combined modification, shown in red, lies between the two partial modifications, as they act together against each other. Since the effect of the photon decay from the decay of neutral pions is stronger than the effect of stable neutral pions have on $\langle X_{\max} \rangle$, the former plays a more significant role in the development of air shower simulations.

Comparing the values for all cases with the simulations made in CONEX, it is evident that CORSIKA reproduces all significant features and the values are generally in agreement, but it is also noticeable that nearly all values simulated with CORSIKA are lower than those of its CONEX counterparts. The difference is shown in Figure 5.4 and is due to the fact, that CONEX and CORSIKA simulations were not performed using identical input parameters. This is not dependent on the presence of LV modifications, instead it is an inherent difference between the models. For time reasons, no new simulations were performed.

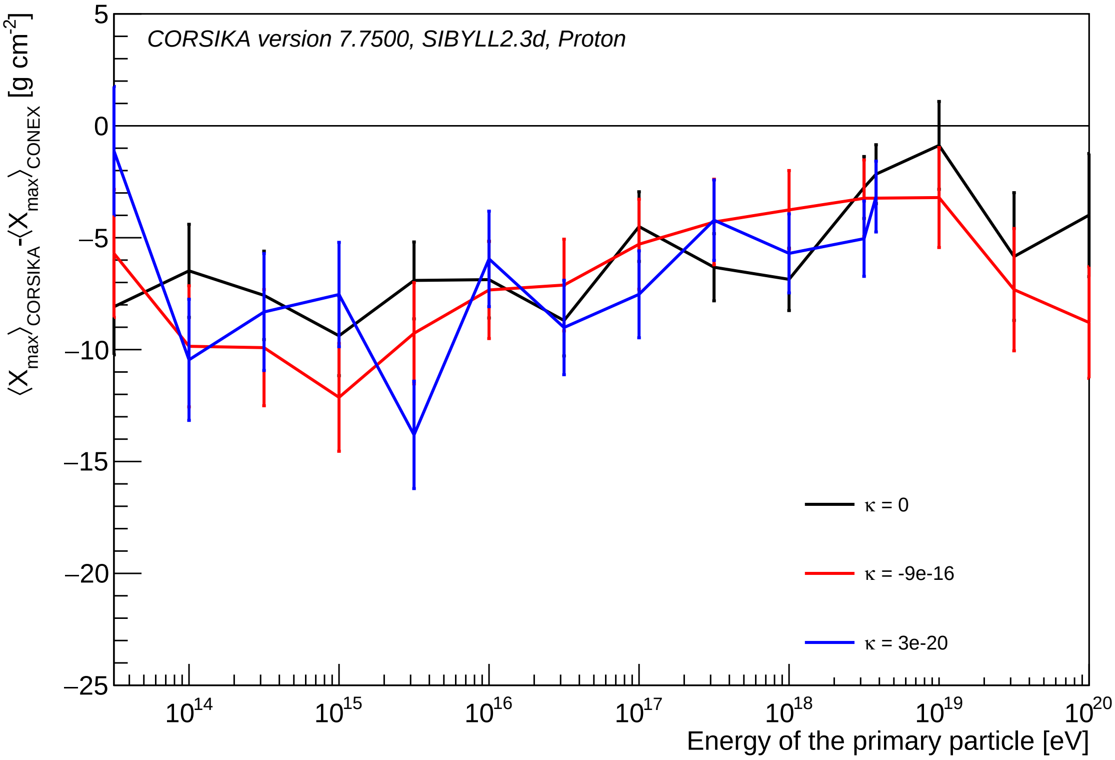

Figure 5.4. *Difference between $\langle X_{max} \rangle$ values for CORSIKA and CONEX simulations as a function of the primary energy of the initiating proton.*

5.1.2 Results for $\sigma(X_{\mathbf{max}})$

Figure 5.5 shows the shower-to-shower fluctuations $\sigma(X_{\max})$ as a function of the primary energy for the CORSIKA simulations. The continuous lines correspond to air showers initiated by a proton, while the dashed lines correspond to iron primaries.

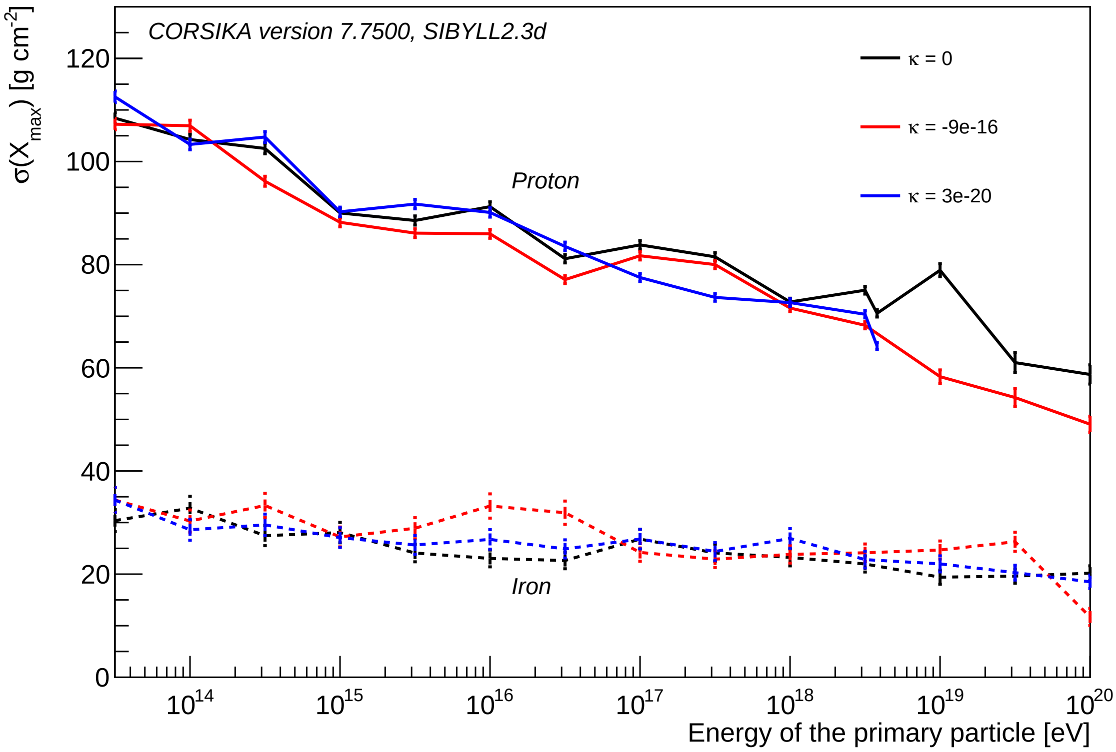

Figure 5.5. *Simulated values using CORSIKA of $\sigma(X_{max})$ as a function of the primary energy of the initiating particle. Proton and iron were used as primary particles and the three different cases for κ are shown. In case of negative κ simulations were done for a value of -9×10^{-16} and for positive κ with a value of* 3×10^{-20}.

It can be seen that $\sigma(X_{\max})$ is nearly independent of the modification for both chosen κ values. This is also true for the partial modifications, as can be seen in Figure 5.6. The standard deviation is mainly determined by the first interaction. Therefore, as the modifications for negative κ only alter electromagnetic interactions, it is expected to have negligible influence. For a positive κ value of 3×10^{-20}, protons will emit VCh radiation for energies of $E \gtrsim 10^{18.58}$ eV, due to this proton initiating air-showers excluded. As such the first interaction is again independent of the modification, as is the case for the iron initiated air shower simulations.

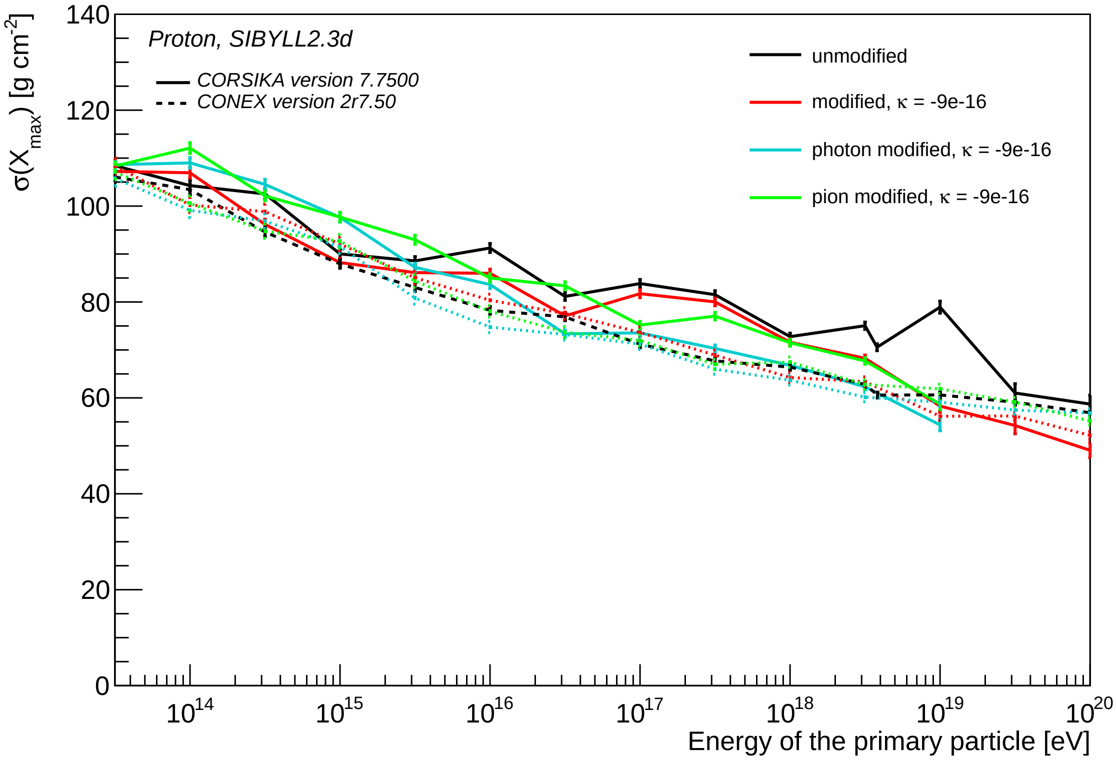

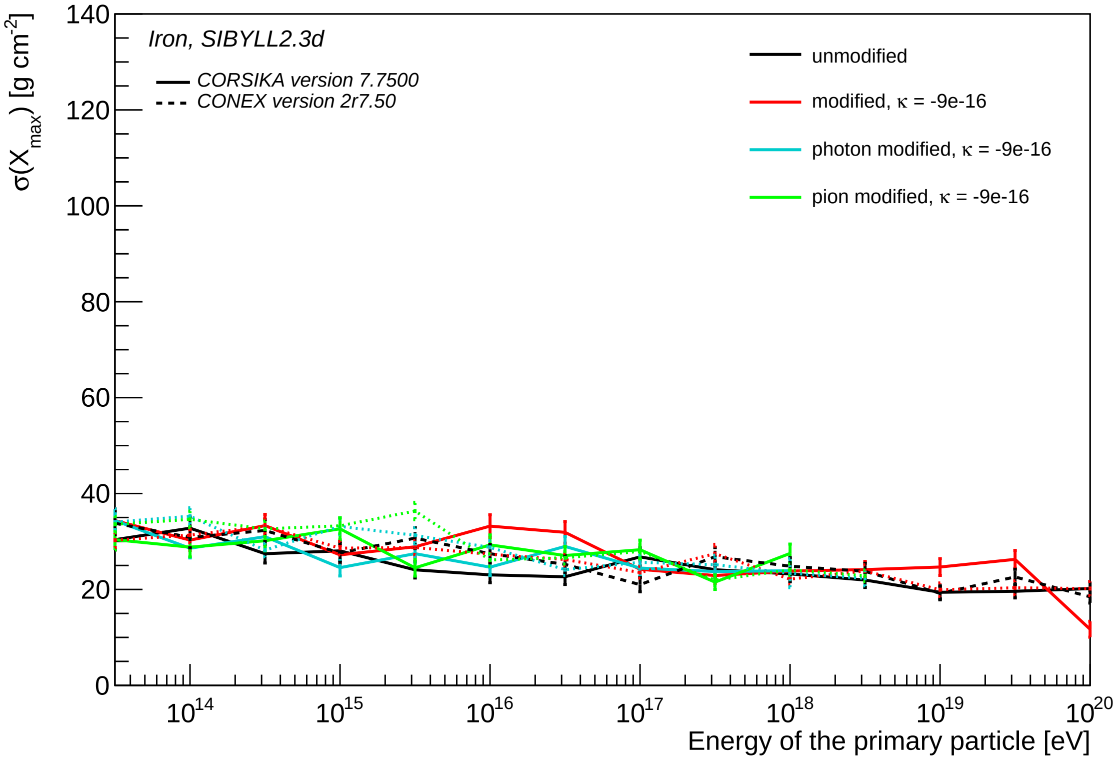

Figure 5.6. *Simulated values of $\sigma(X_{max})$ as a function of the primary energy of the initiating particle. CORSIKA simulations are shown by the solid lines, while CONEX simulations are shown with a dashed line. Protons were used as the primary particle for the top plot and iron for the bottom plot.*

The values for $\sigma(X_{\max})$ derived from CORSIKA fluctuated more and a higher number of simulations was needed to reduce the error bars to a level where the curves more or less flattened out. This might be attributed to certain input variables, such as the thinning level, or the magnetic field, but due to time constraints testing every input variable on their effect on the shower observables was not feasible. This could probably also have been slightly improved by stricter constraints on the goodness of the fit, but it was not necessary to determine if the modifications were implemented correctly. Outliers, such as the value for the unmodified case at a primary energy of 10^{19} eV are possibly due to lower statistics at the highest energy.

CORSIKA also reproduces the values of CONEX for $\sigma(X_{\max})$, but it is also noticeable, that nearly all values simulated with CORSIKA are higher than its CONEX counterparts. This difference is shown in Figure 5.7 and is again due to the fact that CONEX and CORSIKA simulations were not performed using identical input parameters. Again, the difference is independent of modification.

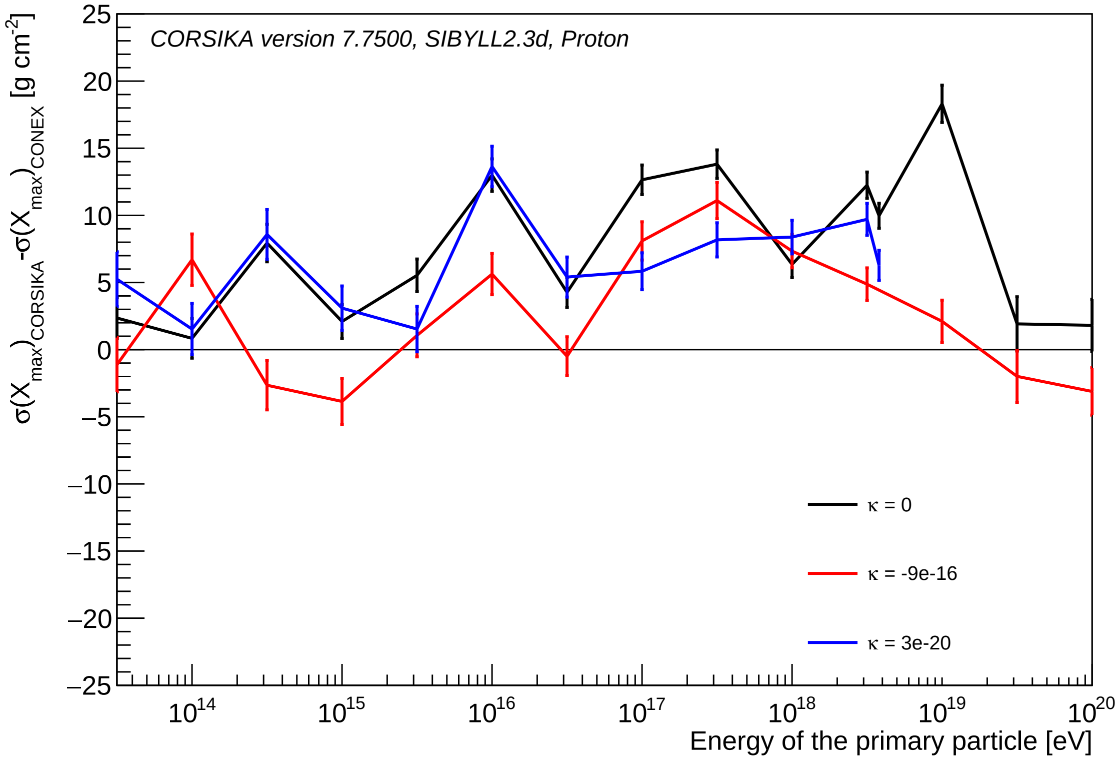

Figure 5.7. *Difference between $\sigma(X_{max})$ values for CORSIKA and CONEX simulations as a function of the primary energy of the initiating proton.*

5.1.3 Results for N_μ

The number of muons at ground level N_μ as a function of the primary energy follows a power law. Instead of showing the exact number of muons, Figure 5.8 shows the number of muons at ground level normalized to the unmodified case as a function of the primary energy for the CORSIKA simulations. The continuous lines correspond to air showers initiated by a proton, while the dashed line corresponds to iron primaries.

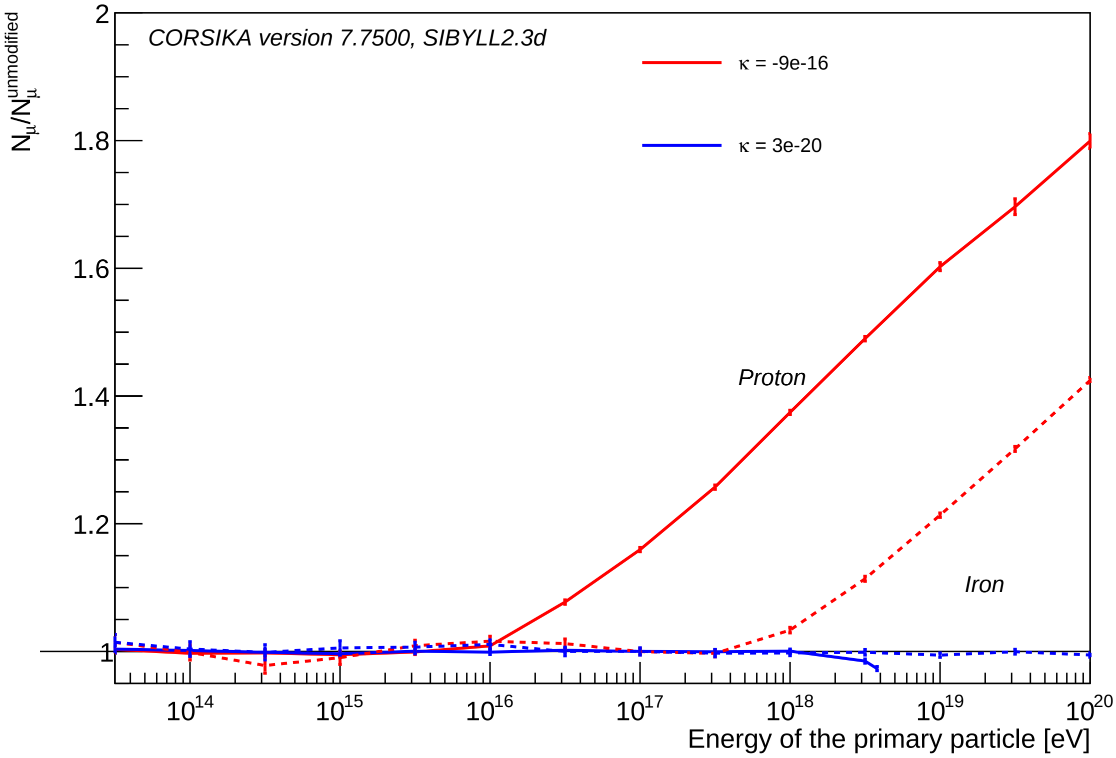

Figure 5.8. *Simulated values using CORSIKA of the number of muons at ground level normalized to the unmodified case as a function of the primary energy of the initiating particle. Proton and iron were used as primary particles and the three different cases for κ are shown. In case of negative κ, simulations were done for a value of -9×10^{-16} and for positive κ with a value of 3×10^{-20}.*

In this plot the difference can be seen more clearly, compared to a double logarithmic plot, where the lines $N_\mu(E)$ lie close together. Additionally, air shower simulations show a deficit in the muon number compared to measurements, called the muon puzzle [46]. The important part is that for positive κ, a small reduction compared to the unmodified case can be observed, while negative κ increase the number of muons.

Positive Value of κ

Figure 5.9 shows the number of muons at ground level normalized to the unmodified case for a positive κ value of 3×10^{-20}. The top plot shows proton initiated simulations, while the simulations for the bottom plot were performed with a primary iron particle.

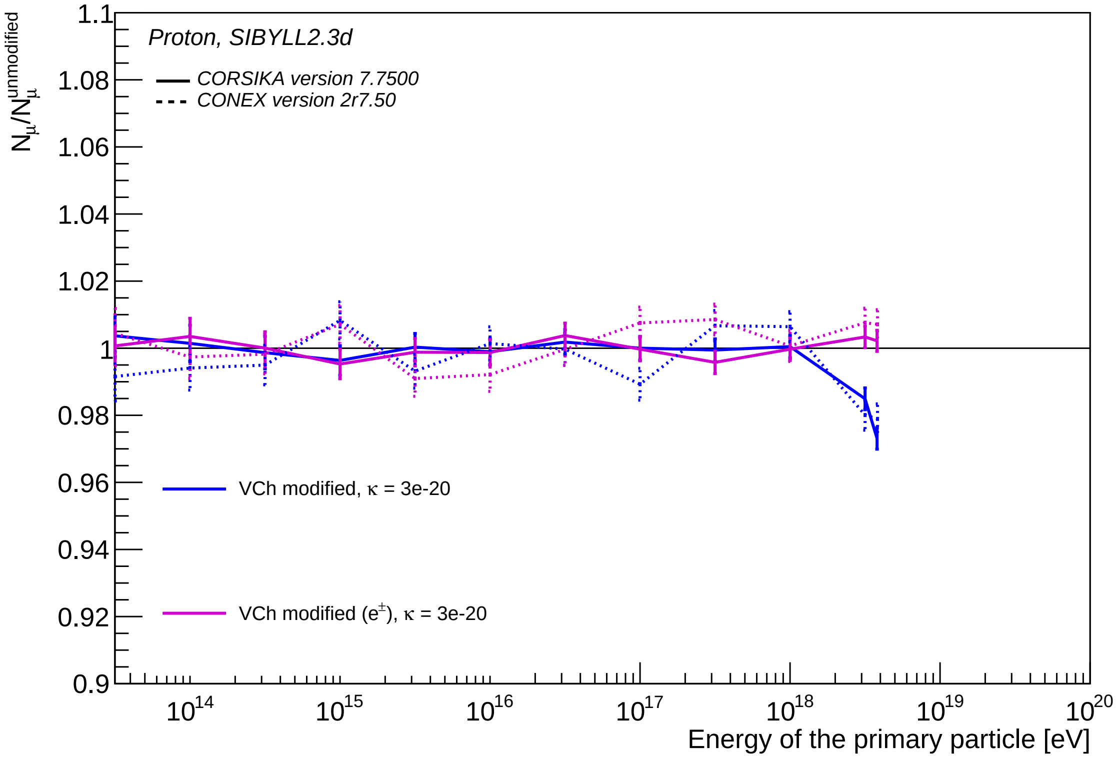

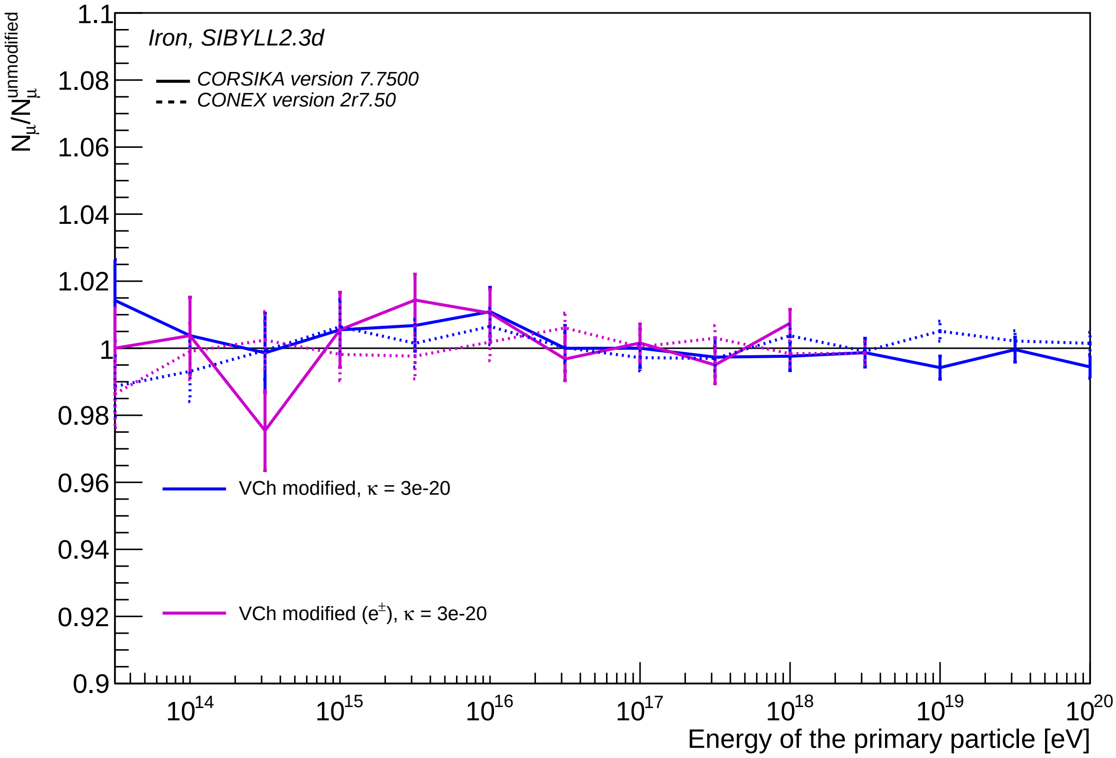

Figure 5.9. *Simulated values of the number of muons at ground level, normalized to the unmodified case as a function of the primary energy of the initiating particle for the unmodified case and for a κ value of 3×10^{-20}. CORSIKA simulations are shown by the solid lines, while CONEX simulations are shown with a dashed line. Protons were used as the primary particle for the top plot and iron for the bottom plot.*

In the proton initiated simulations, the number of muons at ground level for the last two simulated primary proton energies is smaller compared to the unmodified case for the VCh modification in blue. For all other energies and for the partial modification shown in magenta, all values are in good agreement with the unmodified case. In other words, for positive κ only the radiation of Cherenkov photons in the hadronic shower influences the number of muons, and as such the number of muons at ground level. This is because energy of the hadronic part is fed via the VCh radiation into the electromagnetic part, leading to fewer muons. This is comparable to the number of muons as a function of the primary energy, when the initiating particle is a hadron, as less energetic hadrons will produce less muons in the EAS. The simulations performed with CORSIKA and CONEX are in good agreement.

Negative Value of κ

Figure 5.10 shows the number of muons at ground level normalized to the unmodified case for a negative κ value of -9×10^{-16}. The top plot shows proton initiated simulations, while the simulations for the bottom plot were performed with a primary iron particle. It can be seen that the increase in the number of muons is due to the modification of the pion lifetime, while photon decay has only a minor effect, seemingly reducing the number of muons. Even though most of the values are in good agreement with the unmodified case regarding their statistical errors, it is evident, that the values of the photon modified graph are for energies higher than 10^{17} eV below 1, while the modified curve is always below the pion modified curve. This is a relatively small effect that can not be explained by the Heitler toy model, where no muons will be produced from the electromagnetic part of the air shower. After the implementation of the photon decay, unlikely processes, including those in which these photons would create muons, are no longer possible, leading to a small reduction in the number of muons. The increased lifetime of neutral pions, on the other hand, causes some of those pions, mainly the stable neutral pions, to interact further hadronically, instead of feeding the electromagnetic part. Through these interactions new charged hadrons, such as $\pi^{\pm}$ and $K^{\pm}$, will be produced, which will decay into additional muons. The increase of muons is as such bound to the threshold energy given by Equation (2.3.12). The reason that the onset for iron initiated air showers is shifted to higher energies, is explained by the superposition model for initiating nuclei as discussed for $\langle X_{\mathrm{max}} \rangle$.

While the increase, especially for protons, appears with around 80% at an energy of 10^{20} eV extremely high, this κ value is already excluded. For higher κ values, and thus for stricter bounds on LV, the onset will shift to higher and higher energies. As the muon puzzle was shortly mentioned before, it should be stated here, that the LV theory implemented in this work is no solution to the problem, although negative κ could contribute to explain a smaller part of the muon deficiency.

The simulations performed with CORSIKA generally agree with those made with CONEX, but it can also be seen that the increase at the highest energies by proton initiated air showers, as well as for iron induced EAS, are below the increase expected by CONEX. The small difference is due to the fact, that not the exact same initial conditions for CORSIKA and CONEX were selected.

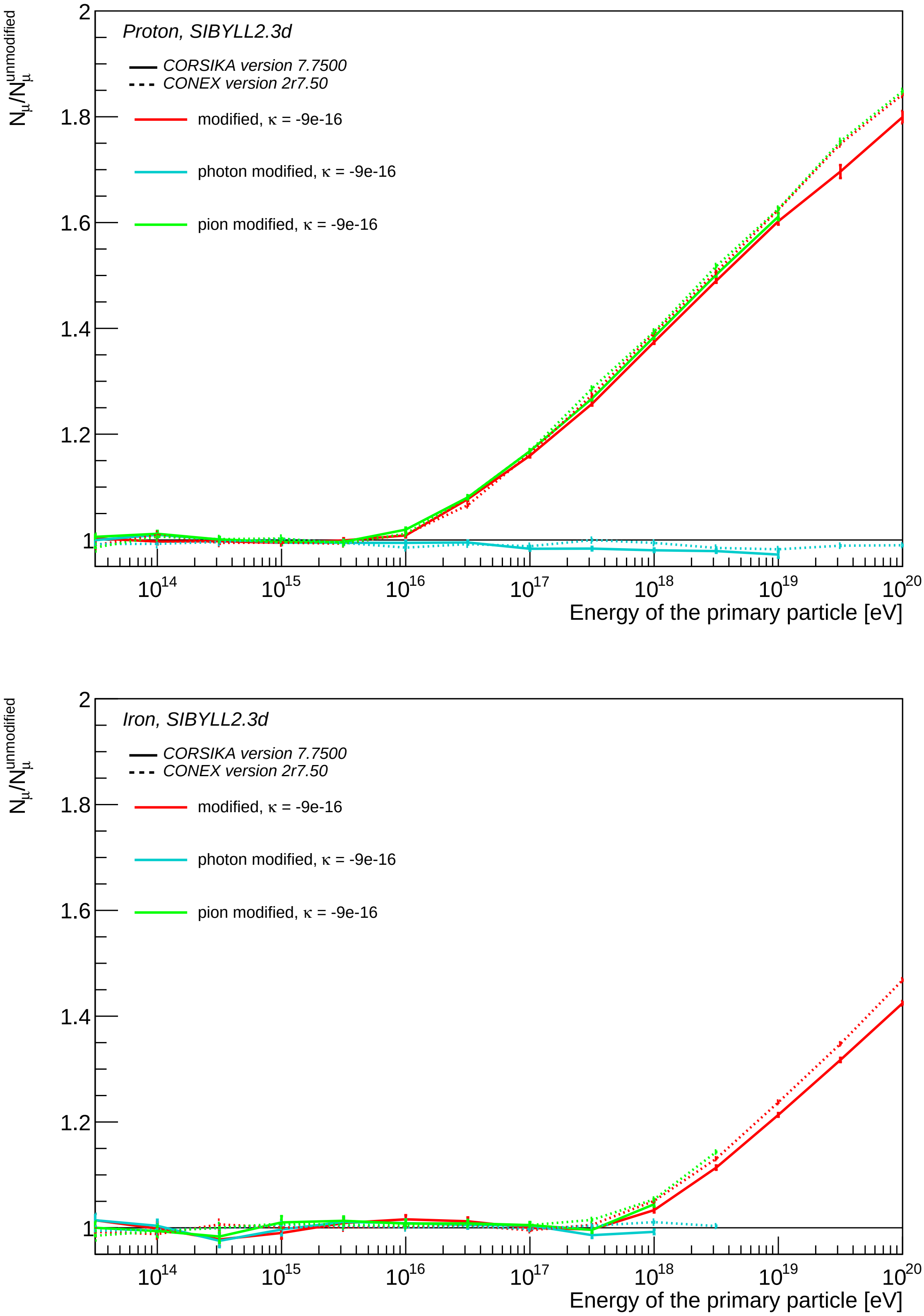

Figure 5.10. *Simulated values of the number of muons at ground level, normalized to the unmodified case as a function of the primary energy of the initiating particle for the unmodified case and for a κ value of -9×10^{-16}. CORSIKA simulations are shown by the solid lines, while CONEX simulations are shown with a dashed line. Protons were used as the primary particle for the top plot and iron for the bottom plot.*

5.2 New Observables

While the LV effects were implemented in the CONEX part of the simulations, after an energy threshold the particles are passed to CORSIKA, which distributes the particles 3-dimensionally. With CORSIKA's continued simulation processes, it is possible to obtain observables connected to the lateral particle distribution. The following sections detail particle densities at the set observation level, which corresponds to the ground level at the Pierre Auger Observatory, which were not available to 1-dimensional simulations, such as standalone CONEX simulations.

5.2.1 Muon Density $\langle \rho_{\mu^\pm} \rangle$

The muon density is of special interest, as muons are the main component of particles triggering the water Cherenkov detectors at the Pierre Auger Observatory. Figure 5.11 shows the average muon densities as a function of the distance from the shower core. As discussed for the number of muons at ground level, simulations yield less muons than are measured by experiments. Since no follow-up detector simulation is performed, the change in muon density is more meaningful, as it is correlated to the expected detector signals.

However, looking at Figure 5.11, it can be seen that only the case of negative κ has a major impact on the muon density, which is caused by the change in the pion life time. The shape of the distribution remains mostly unchanged, which can further be seen in Figure 5.12. The number of muons decreases fast with increasing distance. In case of unmodified simulations initiated by a proton with an energy of 10^{18} eV, the mean density of muons at 160 meters is around 10 m^{-2}, while at 880 meters it is only about 0.1 m^{-2}.

The error bars correspond to the statistical error. Since all simulations are vertical air showers with a zenith angle of 0°, no angular dependence has to be considered. As such, the area for each bin, with the exception of the first, corresponds to an annulus. The first bin is a circle with a radius of two times the bin width, so in this case of 160 meters.

The specific primary energy of 10^{18} eV, shown in this plot, was chosen, as this is the highest energy for which simulations were performed for all modifications, both for proton and iron initiated air showers. The higher the energy, the higher the effect on the observable, as already explained for the 1-dimensional observables.

The muon density is slightly higher for iron induced air showers, as can be seen from a comparison between the top and bottom plot. It is also evident that the effect at the same energy is much smaller. Figure 5.12 and Figure 5.13 only display the results for proton initiated air showers, because the effect of the implemented LV is shifted to higher energies for heavier nuclei, as already discussed using the superposition-model for EAS, and the number of simulations for iron, with only 100 simulations, is much smaller.

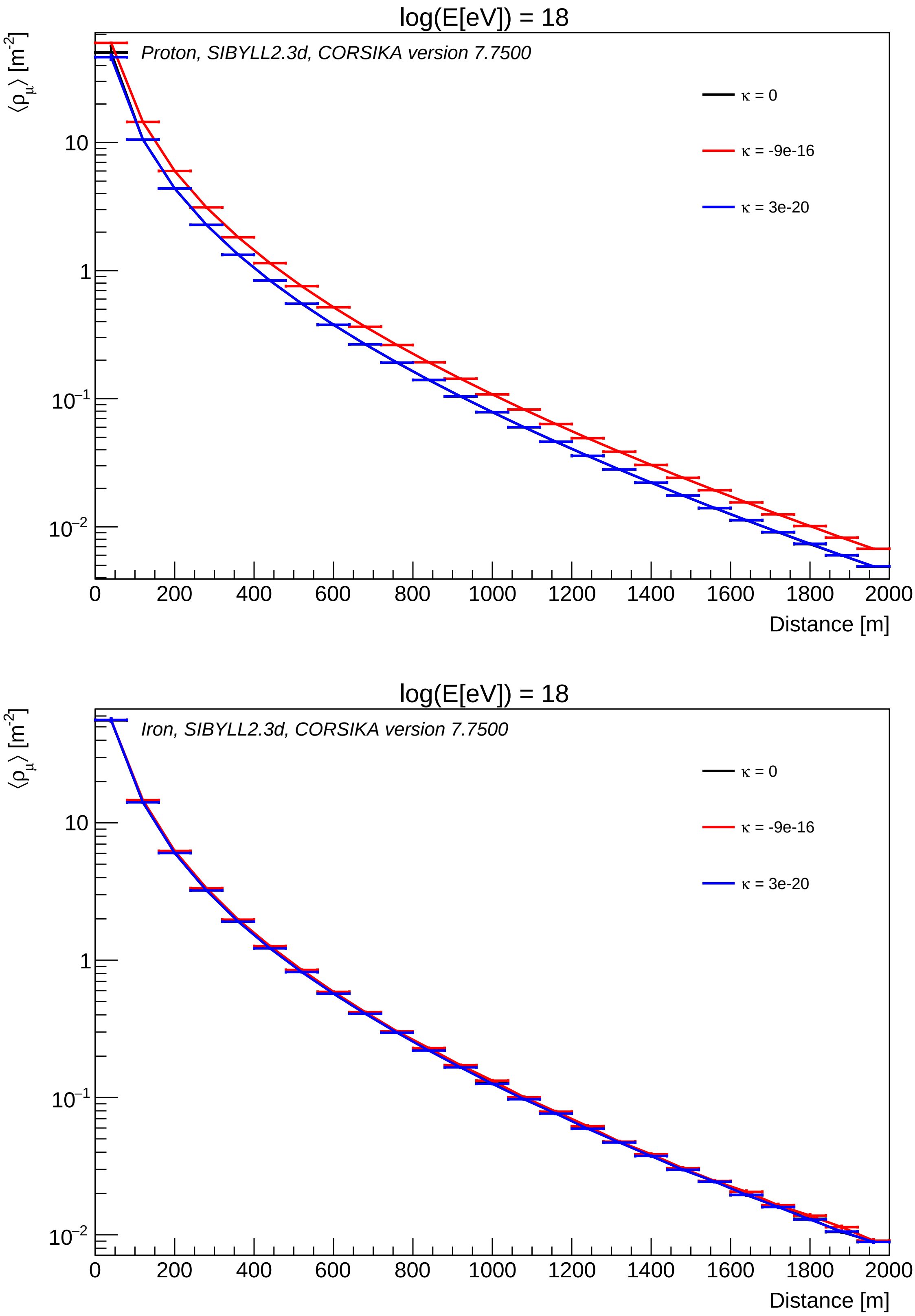

Figure 5.11. *Simulated values of the average muon density* $\langle \rho_{\mu^\pm} \rangle$ *at ground level as a function of the distance from the shower core. Protons were used as the primary particle for the top plot and iron for the bottom plot, both with a primary energy of* 10^{18} eV.

Figure 5.12 displays the change of the average muon density at ground level for the different modifications, as a factor of the unmodified values as a function of the distance from the shower core. The first bin at 40 meters has a large statistical error compared to the other distances, which is a remnant of the thinning algorithm used by CORSIKA. The thinning was applied up to a maximum distance of 80 meters, such that it only takes place in the first bin of the histogram.

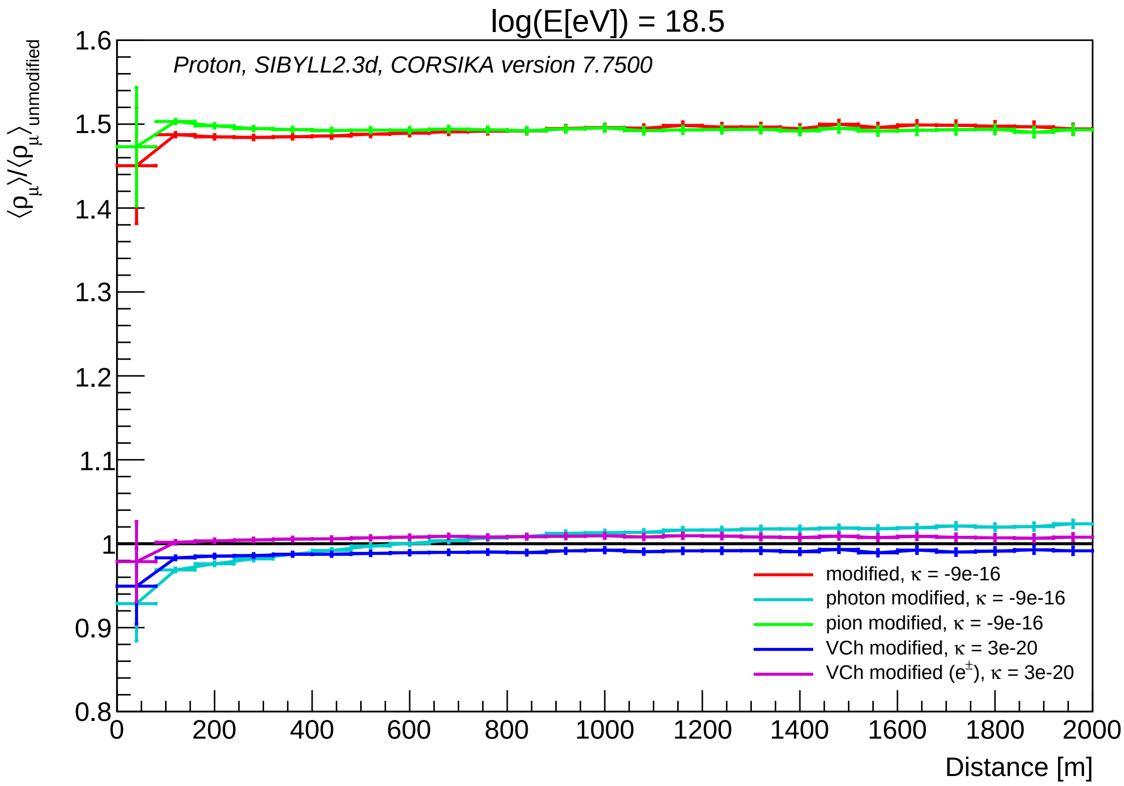

Figure 5.12. *Simulated values of the average muon density $\langle \rho_{\mu^\pm} \rangle$ at ground level, normalized to the unmodified case as a function of the distance from the shower core. Protons were used as the primary particle with a primary energy of* $10^{18.5}$ *eV.*

The values for the modified and pion modified cases are fairly constant independent of the distance and show an increase in muon density of about 50%. At low distances the muon density for the pion modified case is slightly higher, as the values for the implemented photon decay show a decrease in the muon density at these distances. In the second bin at 120 meters the density decreases by about 3% for the photon modified case compared to the unmodified simulations, but rises to an increase of about 2% at a distance of 1960 meters. The increase in the muon density for the pion modified case is the same as for the number of muons at ground level. Because of the change to the neutral pion decay, more charged pions are produced in the air shower leading to an increase in muons through their decay. For the photon modified case, this is different, as we can observe a change in muon density as a function of the distance from the shower core. It should be kept in mind, that the LV effects were implemented in the 1-dimensional simulation part. Through the implemented effects the expected lateral distribution of particles will change. For example, in the case of VCh radiation, one expects more photons distributed like the particles, which radiated them. As such, this trend could also be influenced by the fact that CORSIKA does not take into account the changed lateral distribution functions after transferring particles from CONEX, rather than solely by the implementation itself. Additionally, this might be explained by the lateral distribution of electrons and positrons discussed in the next section, which follows a similar trend. Therefore, a reduction or increase could be dependent on reaction channels where electrons and positrons create muons and the change in electrons and positrons compared to the unmodified case.

For positive κ, the plot shows that VCh radiation of electrons and positrons causes no significant change in the number of muons, as the values are in good agreement with 1. The reduction in muon density for the VCh modified case is also quite small at this energy. At the highest primary energy for the VCh modified case, the reduction increases to about 2%.

Figure 5.13 shows the average muon density at ground level, normalized to the unmodified case at a distance of 1 km from the shower core as a function of the primary energy. This reproduces the values for the absolute change of the number of muons very well if compared to Figures 5.9 and 5.10, with the exception of the photon modified values at the highest energies. Here, at 10^{19} eV, the plot indicates an increase of about 1% compared to the decrease in the number of muons in Figure 5.10. The distance of 1 km was chosen as the values correlate to the commonly used variable S(1000) in air shower experiments.

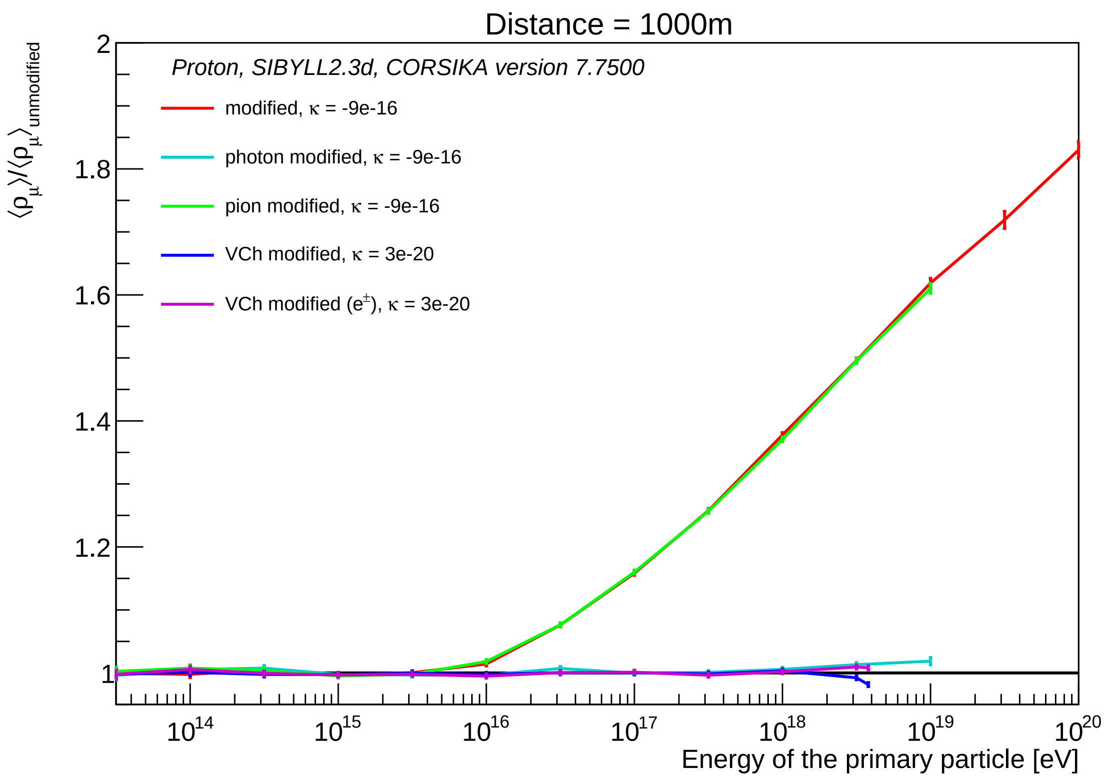

Figure 5.13. *Simulated values of the average muon density $\langle \rho_{\mu^\pm} \rangle$ at ground level, normalized to the unmodified case as a function of the primary energy of the initiating proton at a distance of* 1 *km from the shower core.*

5.2.2 Electron and Positron Density $\langle\rho_{\mathbf{e}^\pm}\rangle$

Figure 5.14 shows the average density of electrons and positrons as a function of the distance from the shower core for a proton initiated air shower with a primary energy of 10^{18} eV. It can be seen compared to the muon density in Figure 5.11 that there are on average more electrons and positrons than muons. Together with Figure 2.11, this is a quick cross-check. In this case, there are about 10^4 particles per square meter for the unmodified case within 80 meters of the shower core at the chosen observation level, corresponding to the Pierre Auger Observatory's height. The number shrinks down to about 10^{-2} m^{-2} at the last bin at a distance of 1960 m to the shower core.

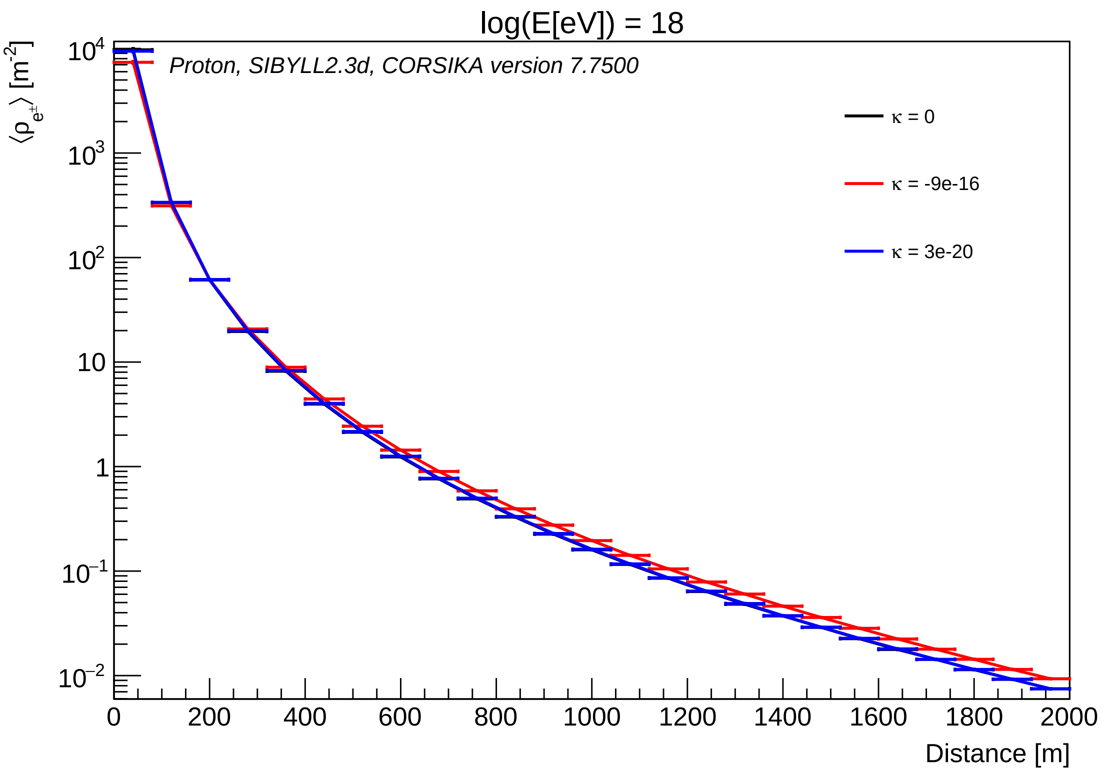

Figure 5.14. *Simulated values of the average electron and positron density $\langle\rho_{e^\pm}\rangle$ at ground level as a function of the distance from the shower core. Protons were used as the primary particle with a primary energy of 10^{18} eV.*

Figure 5.15 is much better suited to compare the differences of the modifications. The large statistical error of the values for the first bin is again caused by the thinning algorithm.

For positive κ, the density for both modifications increases by about 2% at low distances from the shower core, trending towards no change at the last displayed bin, where the values are consistent with the unmodified case.

For negative κ, it can be seen that the density of electrons and positrons decreases near the shower core, for the first two bins, while it increases at distances beyond this compared to the unmodified case. For the pion modified case, this seems surprising at first, because neutral pions above the threshold energy do not decay into a photon pair, which in turn would create electrons and positrons. It is important to consider the lateral distribution of electrons and positrons here which can be seen in Figure 5.14. A reduction of $2-3\%$ in the first bins for the pion modified case with a density of more than 10^4 m^{-2} leads to a loss of more electrons and positrons than the increase of up to 30% at further distances, because the density is falling strongly in the logarithmic plot. The same is true for the photon modified and modified cases, where the reduction of the density is even larger compared to the unmodified case. Through the photon decay into an electron-positron pair, the overall number of photons at the chosen observation level decreases for these simulations. The observation level was chosen as the height of the Pierre Auger Observatory, corresponding to 870 g cm^{-2}. As already seen in Figure 5.3 the average atmospheric depth of the shower maximum is for the primary energy of $10^{18.5}$ eV around 660 g cm^{-2} for the photon modified case, which is a large reduction compared to the unmodified case. Therefore, more particles of the electromagnetic shower will already be absorbed at the observation level. At a much earlier atmospheric depth, where electrons and positrons are created through photon decay at earlier steps in the shower development, an increase of the density would be expected. The increase of the density at further distances from the shower core might be explained by the different lateral particle distributions. After reaching the threshold energy for photon decay, particles are transferred to CORSIKA. This means, together with the contracted electromagnetic subshowers, when there would normally be photons around this energy, they will be replaced by an electron-positron pair, and follow a different distribution compared to the photons.

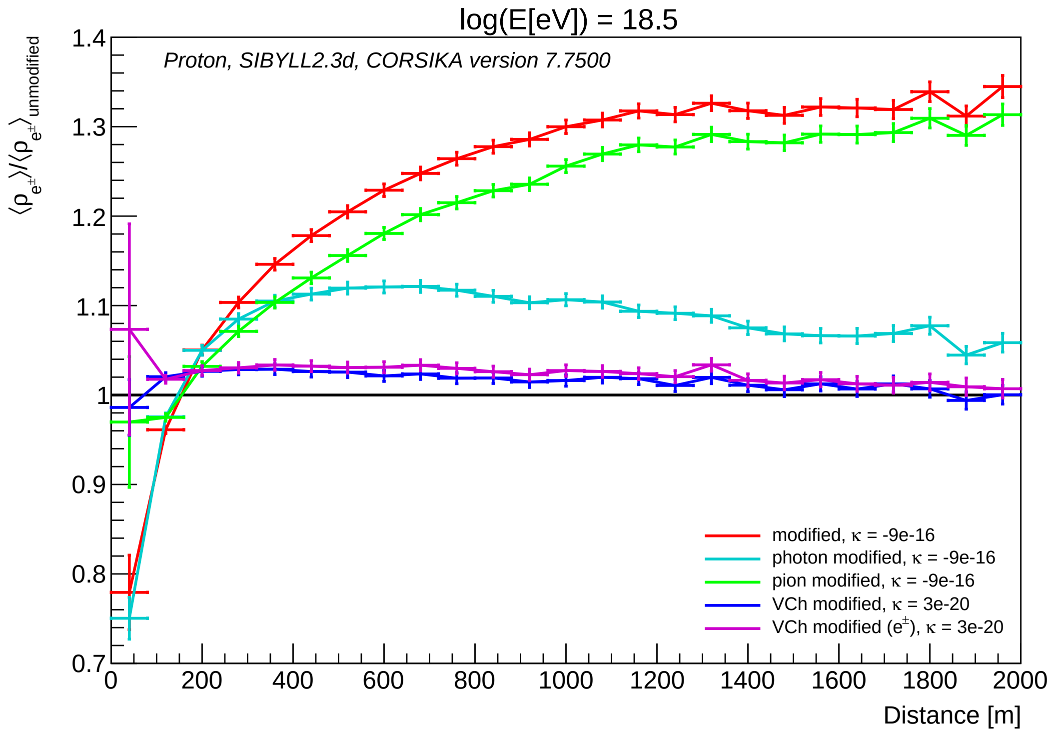

Figure 5.15. *Simulated values of the average electron and positron density* $\langle\rho_{e^\pm}\rangle$ *at ground level, normalized to the unmodified case as a function of the distance from the shower core. Protons were used as the primary particle with a primary energy of* $10^{18.5}$ *eV.*

5.2.3 Charged Pion Density $\langle \rho_{\pi^\pm} \rangle$

Lastly, the average density of charged pions will be shown. Figure 5.16 displays the density as a function of the distance from the shower core for a proton initiated air shower with a primary energy of 10^{18} eV. The total values can again be compared to the density of muons or electrons and positrons. It can be seen that there are fewer charged pions, starting at around 10 m^{-2} in the first bin to nearly 10^{-6} m^{-2} in the last bin. Because of their small numbers at large distances from the shower core the statistical fluctuations are stronger.

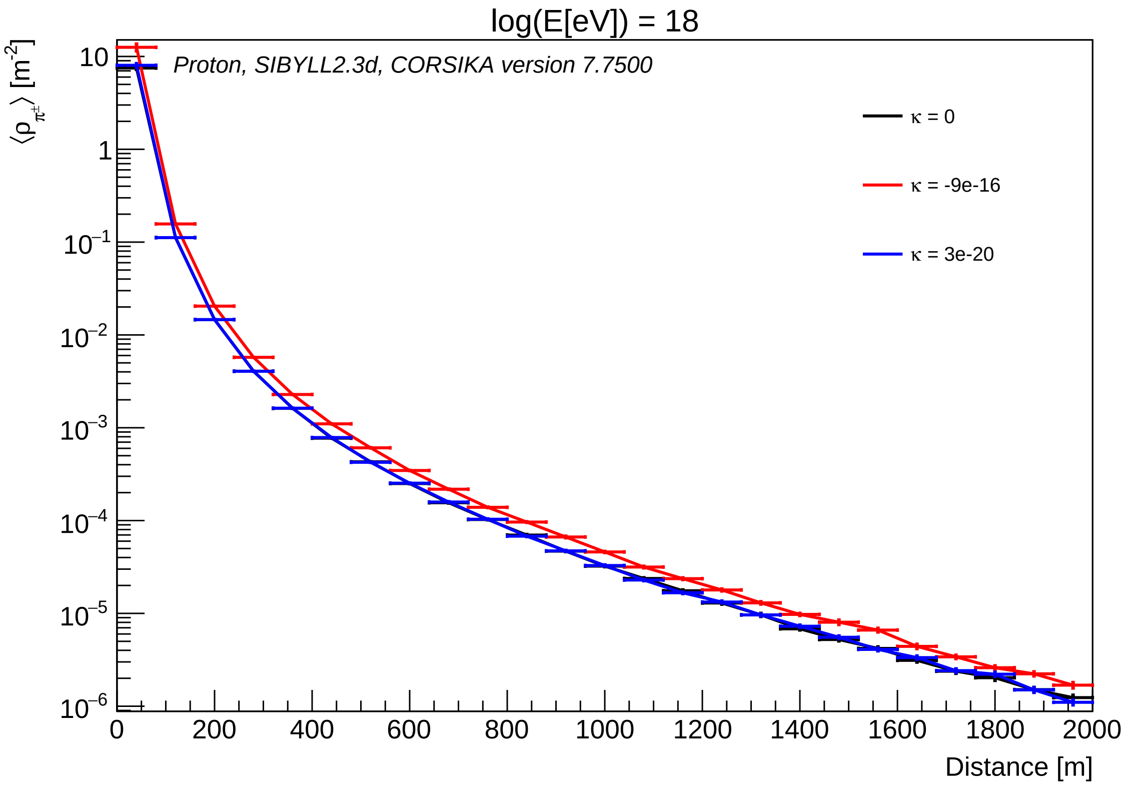

Figure 5.16. *Simulated values of the average pion density $\langle \rho_{\pi^\pm} \rangle$ at ground level as a function of the distance from the shower core. Protons were used as the primary particle with a primary energy of 10^{18} eV.*

This section is included to show that the modification of the pion lifetime indeed increases the number of charged pions. This is confirmed and illustrated in Figure 5.17 at ground level for a proton initiated air shower with a primary energy of $10^{18.5}$ eV at the top and for a distance of 1 km at the bottom. In the top plot, an increase of about 50% can be seen for the pion modified and modified cases, although values are fluctuating strongly at the highest distances from the shower core in the plot. In the bottom plot, a steady increase as a function of the proton's primary energy can be seen, while the other modifications are in good agreement with the unmodified case. For small primary energies, the statistical errors are significant due to the low number of charged pions. At the highest energies the error is also slightly higher, due to the lower number of simulations performed at these energies.

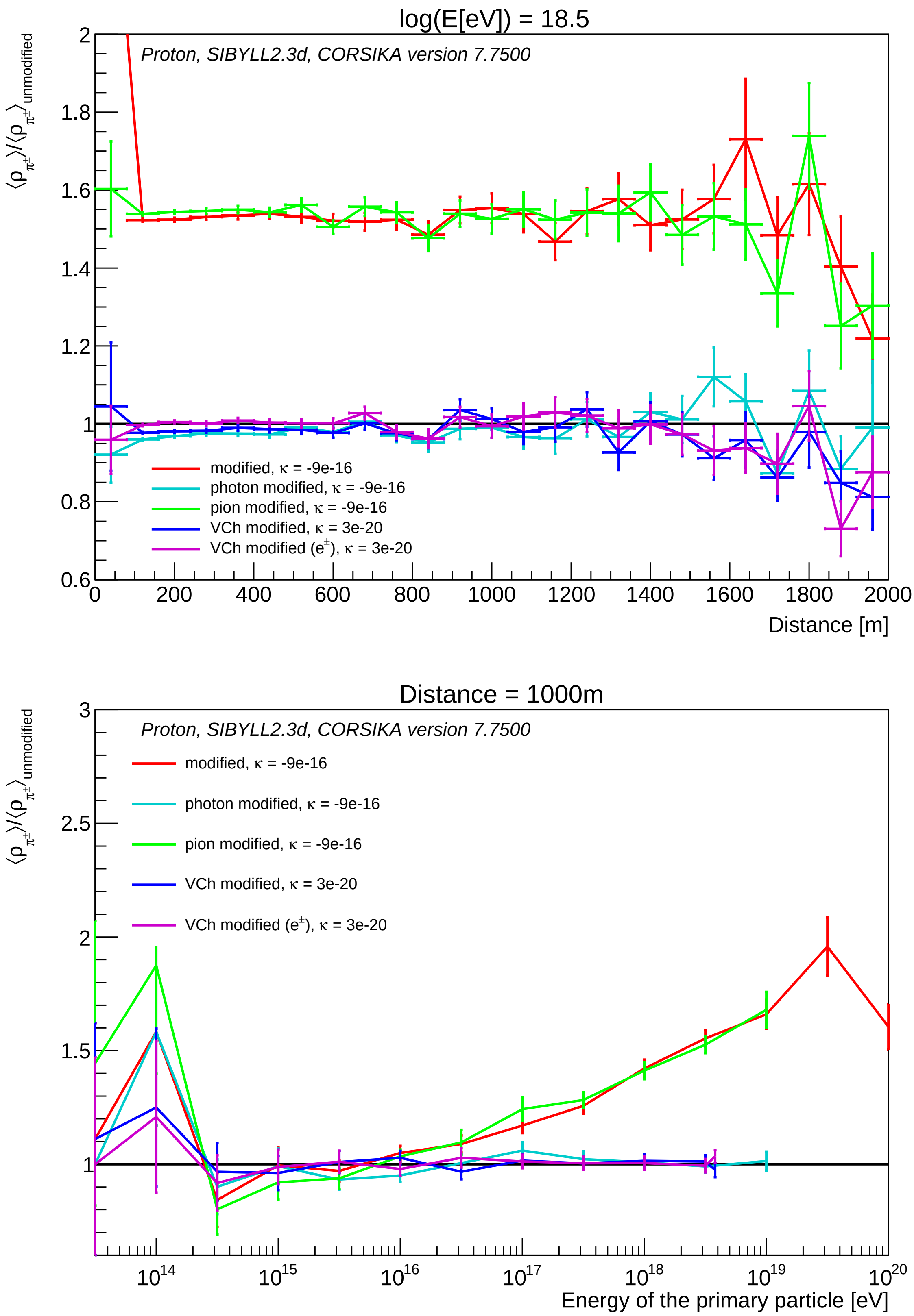

Figure 5.17. *Values of the average pion density $\langle \rho_{\pi^\pm} \rangle$ at ground level, normalized to the unmodified case for proton initiated air shower simulations. The top figure plots the values as a function of the distance from the shower core with a primary energy of $10^{18.5}$ eV. The bottom figure plots the values as a function of the primary energy at a set distance of 1 km.*

6. Summary and Outlook

The aim of this thesis was to implement effects violating Lorentz invariance into the 3-dimensional air shower simulation program CORSIKA. This was motivated by the access to new observables such as those connected to the lateral particle distribution, which are unavailable to a 1-dimensional simulation. Through the inclusion of additional observables, an improved search for LV will be possible.

The isotropic, non-birefringent LV in question was discussed in chapter 2.3. It is controlled by a single dimensionless parameter κ. The effects of LV were introduced separately for both, positive and negative κ in the FORTRAN Monte Carlo code of the CONEX simulation. After reaching a certain energy threshold, particles are transferred to CORSIKA, where the remaining simulation is performed in 3 dimensions.

CORSIKA simulations were performed for $\kappa = 3 \times 10^{-20}$ and for $\kappa = -9 \times 10^{-16}$, including some partial modifications to the unmodified simulation code, such as only photon decay without altering the pion lifetime for negative κ. As part of this work, after the simulations were completed, the CORSIKA raw files were read out and converted into ROOT files for subsequent analysis and visualization of the data.

The simulations confirmed the LV effects on air showers observables and a comparison with stand-alone CONEX simulation results was made to ensure that the LV effects were correctly implemented. However, due to non-identical input parameters between the simulations performed with CORSIKA and stand-alone CONEX, small deviations were found. As these deviations are independent of the implementation of LV, the results are consistent with the expected behavior, confirming correct implementation. The effects of the LV on both previously analyzed as well as additional observables were also discussed. The average atmospheric depth of the shower maximum $\langle X_{\mathrm{max}} \rangle$ decreases for both κ cases, because the electromagnetic subshowers develop earlier. The shower-to-shower fluctuations $\sigma(X_{\mathrm{max}})$ stay roughly the same, as the first hadronic interaction was not changed. The number of muons N_μ decreases slightly for positive κ, but increases for negative κ. In the positive case, this is due to the redistribution of energy in the hadronic shower part, where muons are mainly produced through decay, to the electromagnetic part. For negative κ, the number of muons increases because more charged pions are produced due to the longer lifetimes of neutral pions.

Additionally, results of the CORSIKA simulations were presented for lateral particle densities at ground level corresponding to the Pierre Auger Observatory, showing indeed a change consistent with the changes observed in 1-D.

Future work could involve implementing Lorentz-violating effects in the general CORSIKA code, particularly in versions 7 or 8. A comparison of particle densities between simulations using CONEX at the highest energies and CORSIKA simulations across the entire energy range would also be beneficial. Further steps might include performing detector simulations and incorporating newly obtained observables in an analysis. Future analyses incorporating additional observables may lead to improved constraints on Lorentz violation, potentially improving existing bounds on κ.

Bibliography

[1] S. Liberati and L. Maccione. "Lorentz Violation: Motivation and New Constraints". In: *Annual Review of Nuclear and Particle Science* 59.1 (Nov. 2009), pp. 245–267. ISSN: 1545-4134.

[2] F. R. Klinkhamer and M. Schreck. "Consistency of isotropic modified Maxwell theory: Microcausality and unitarity". In: *Nuclear Physics B* 848.1 (July 2011), pp. 90–107. ISSN: 0550-3213.

[3] T. Bergmann et al. "One-dimensional hybrid approach to extensive air shower simulation". In: *Astropart. Phys.* 26 (2007), pp. 420–432. eprint: `astro-ph/0606564`.

[4] T. Pierog et al. "First Results of Fast One-dimensional Hybrid Simulation of EAS Using CONEX". In: *Nucl. Phys. Proc. Suppl.* 151 (2006), pp. 159–162. eprint: `astro-ph/0411260`.

[5] F. R. Klinkhamer, M. Niechciol, and M. Risse. "Improved bound on isotropic Lorentz violation in the photon sector from extensive air showers". In: *Phys. Rev. D* 96 (11 Dec. 2017), p. 116011.

[6] F. Duenkel, M. Niechciol, and M. Risse. "Photon decay in ultrahigh-energy air showers: Stringent bound on Lorentz violation". In: *Physical Review D* 104.1 (July 2021), p. 015010. ISSN: 2470-0029.

[7] D. Heck et al. *CORSIKA: a Monte Carlo code to simulate extensive air showers.* FZKA-6019. 1998.

[8] W. Demtröder. *Experimentalphysik 1.* 8th ed. Springer Spektrum, 2018.

[9] W. Nolting. *Theoretical Physics 4.* 1st ed. Springer Cham, 2017.

[10] S. Weinberg. *The Quantum Theory of Fields. Volume 1: Foundations.* Cambridge University Press, 1995.

[11] S. Weinberg. *The Quantum Theory of Fields. Volume 2: Modern Applications.* Cambridge University Press, 1996.

[12] S. P. Martin and J. D. Wells. *Elementary Particles and Their Interactions.* 1st ed. Springer Cham, 2022.

[13] `https://home.cern/news/news/cern/sit-down-coffee-standard-model` accessed on July 22, 2024.

[14] `https://upload.wikimedia.org/wikipedia/commons/0/00/Standard_Model_of_Elementary_Particles.svg` accessed on July 22, 2024.

[15] `https://atlas.cern/updates/briefing/weighing-top-quark-mass` accessed on September 23, 2024.

[16] W. Hollik. *Quantum field theory and the Standard Model.* 2010. arXiv: `1012.3883 [hep-ph]`.

[17] W. Demtröder. *Experimentalphysik 4.* 5th ed. Springer Spektrum, 2017.

[18] S. Chadha and H.B Nielsen. "Lorentz invariance as a low energy phenomenon". In: *Nuclear Physics B* 217.1 (1983), pp. 125–144. ISSN: 0550-3213.

[19] V. A. Kostelecký and M. Mewes. "Signals for Lorentz violation in electrodynamics". In: *Phys. Rev. D* 66 (5 Sept. 2002), p. 056005.

[20] F. R. Klinkhamer and M. Schreck. "New two-sided bound on the isotropic Lorentz-violating parameter of modified Maxwell theory". In: *Phys. Rev. D* 78 (8 Oct. 2008), p. 085026.

[21] J. S. Díaz and F. R. Klinkhamer. "Parton-model calculation of a nonstandard decay process in isotropic modified Maxwell theory". In: *Phys. Rev. D* 92 (2 July 2015), p. 025007.

[22] F. Duenkel, M. Niechciol, and M. Risse. "New bound on Lorentz violation based on the absence of vacuum Cherenkov radiation in ultrahigh energy air showers". In: *Phys. Rev. D* 107 (8 Apr. 2023), p. 083004.

[23] J. S. Díaz, F. R. Klinkhamer, and M. Risse. "Changes in extensive air showers from isotropic Lorentz violation in the photon sector". In: *Phys. Rev. D* 94 (8 Oct. 2016), p. 085025.

[24] F. R. Klinkhamer. *Lorentz-violating neutral-pion decays in isotropic modified Maxwell theory.* 2018. arXiv: `1610.03315 [hep-ph]`.

[25] M. Casolino and The Pamela collaboration. *The Pamela Cosmic Ray Space Observatory: Detector, Objectives and First Results.* 2009. arXiv: `0904.4692 [astro-ph.HE]`.

[26] C. Grupen. *Astroparticle Physics.* 2nd ed. Springer Cham, 2020.

[27] J. S. George et al. "Elemental composition and energy spectra of galactic cosmic rays during solar cycle 23". In: *The Astrophysical Journal* 698.2 (June 2009), pp. 1666–1681.

[28] A. Aab et al. "Depth of maximum of air-shower profiles at the Pierre Auger Observatory. I. Measurements at energies above $10^{17.8}$ eV". In: *Phys. Rev. D* 90 (12 Dec. 2014), p. 122005.

[29] A. Aab et al. "Depth of maximum of air-shower profiles at the Pierre Auger Observatory. II. Composition implications". In: *Phys. Rev. D* 90 (12 Dec. 2014), p. 122006.

[30] A. Aab et al. "Evidence for a mixed mass composition at the 'ankle' in the cosmic-ray spectrum". In: *Physics Letters B* 762 (Nov. 2016), pp. 288–295. ISSN: 0370-2693.

[31] T. L. Fehler. *Hybrid Search for Photons with the Low-Energy Extensions of the Pierre Auger Observatory.* `https://www.hep.physik.uni-siegen.de/pubs/master/fehler-master.pdf` accessed on August 20, 2024.

[32] A. A. Watson. "High-energy cosmic rays and the Greisen–Zatsepin–Kuz'min effect". In: *Reports on Progress in Physics* 77.3 (Feb. 2014), p. 036901. ISSN: 1361-6633.

[33] J. W. Cronin. “The highest-energy cosmic rays”. In: *Nuclear Physics B - Proceedings Supplements* 138 (Jan. 2005), pp. 465–491. ISSN: 0920-5632.

[34] J. R. Hörandel. “Early cosmic-ray work published in German”. In: *AIP Conference Proceedings* 1516.1 (Feb. 2013), pp. 52–60. ISSN: 0094-243X. eprint: https://pubs.aip.org/aip/acp/article-pdf/1516/1/52/11799915/52_1_online.pdf.

[35] T. Stanev. *High Energy Cosmic Rays*. 3rd ed. Springer Cham, 2021.

[36] Pierre Auger Observatorium. https://www.flickr.com/photos/134252569@N07/22401145072/in/album-72157659225375559/ accessed on August 20, 2024.

[37] R. Engel and D. Schmidt. “Indirect Detection of Cosmic Rays”. In: *Handbook of Particle Detection and Imaging*. Ed. by I. Fleck et al. Cham: Springer International Publishing, 2021, pp. 801–849. ISBN: 978-3-319-93785-4.

[38] P.A. Zyla et al. (Particle Data Group). https://pdg.lbl.gov/2020/listings/rpp2020-list-muon.pdf accessed on September 28, 2024.

[39] The Pierre Auger Collaboration. “The Pierre Auger Cosmic Ray Observatory”. In: *Nuclear Instruments and Methods in Physics Research Section A: Accelerators, Spectrometers, Detectors and Associated Equipment* 798 (Oct. 2015), pp. 172–213. ISSN: 0168-9002.

[40] https://auger.org/ accessed on October 01, 2024.

[41] E. Ahn et al. “Cosmic ray interaction event generator SIBYLL 2.1”. In: *Phys. Rev. D* 80 (9 Nov. 2009), p. 094003.

[42] F. Riehn et al. “Hadronic interaction model sibyll 2.3d and extensive air showers”. In: *Phys. Rev. D* 102 (6 Sept. 2020), p. 063002.

[43] T. Huege D. Heck and T. Pierog. *Extensive Air Shower Simulation with CORSIKA: A User’s Guide*. https://www.iap.kit.edu/corsika/70.php accessed on August 20, 2024.

[44] https://www.iap.kit.edu/corsika/88.php accessed on October 01, 2024.

[45] M. Niechciol. *A New Window to the Universe? Searching for Ultra-High-Energy Photons at the Pierre Auger Observatory*. https://www.hep.physik.uni-siegen.de/pubs/diss/niechciol-dr.pdf accessed on August 20, 2024.

[46] J. Albrecht et al. “The Muon Puzzle in cosmic-ray induced air showers and its connection to the Large Hadron Collider”. In: *Astrophysics and Space Science* 367.3 (Mar. 2022), p. 04054. ISSN: 1572-946X.

Appendix

A. List of Abbreviations

CR	Cosmic Ray
EAS	Extensive Air Shower
FD	Fluorescence Detector
GCR	Galactic Cosmic Ray
LV	Lorentz (invariance) Violation
MC	Monte Carlo
PMT	Photomultiplier Tube
QED	Quantum Electrodynamics
SD	Surface Detector
SM	Standard Model (of particle physics)
UHE	Ultra-High-Energy
VCh	Vacuum Cherenkov

B. Code for Implementation

This appendix provides the modifications made to the file conex_cors.F, which is located in the conex directory of CORSIKA. Section B.1 shows the additional code for the case of a positive κ value of 3×10^{-20}. The implementation for a negative κ value of -9×10^{-16} is given in Section B.2.

B.1 Positive Value of κ

```
C-----------------------------------------------------------------------
      SUBROUTINE VCPionInteraction
C-----------------------------------------------------------------------
C  modified QBall interaction for Pi0 VC radiation
c
c  subroutine called by cnexus
c
c
C-----------------------------------------------------------------------
      implicit none
#include "conex.h"
#include "conex.incnex"
      double precision epq(5),epp(5), aKappa, vcmass, omega, drawnenergy
      integer i,id,iret,nptl0,iptl
      external drangen
      double precision drangen,dummy,efrac

c  Initialize temporary stack
      do i=1,2
         epp(i)=0.d0
         istptlxs(i)=1
         xsptl(1,i)=dptl(1)      !px
         xsptl(2,i)=dptl(2)      !py
         xsptl(3,i)=dptl(3)      !pz
         xsptl(4,i)=dptl(4)      !E
         xsptl(5,i)=dptl(5)      !m
         ityptlxs(i)=0
         iorptlxs(i)=1
         jorptlxs(i)=1
         ifrptlxs(1,i)=0
         ifrptlxs(2,i)=0
         xsorptl(1,i)=0.d0       !x
         xsorptl(2,i)=0.d0       !y
         xsorptl(3,i)=0.d0       !z
         xsorptl(4,i)=0.d0       !t
         xstivptl(1,i)=0.d0
         xstivptl(2,i)=0.d0
         idptlxs(i)=0            !id
      enddo

      nptlxs=0                   !number of secondaries


      aKappa = 3e-20
      vcmass = dptl(5)           !134976.0
      omega = dptl(4)
      drawnenergy = 0

      print *, 'original particle px:',xsptl(1,1),'py:',xsptl(2,1),
     &        'pz:',xsptl(3,i),'E:',xsptl(4,1),'m:',xsptl(5,1)
      call lvdrawrandomenergy(aKappa, omega, vcmass, drawnenergy)
c      print *, 'drawn energy',drawnenergy

      epp(4)=drawnenergy
      epp(1)=dptl(1)*epp(4)/dptl(4)
      epp(2)=dptl(2)*epp(4)/dptl(4)
      epp(3)=dptl(3)*epp(4)/dptl(4)
      epp(5)=0.d0
      id=nint(dptl(10))
      nptlxs=nptlxs+1
      do i=1,4
         xsptl(i,nptlxs)=xsptl(i,nptlxs)-epp(i)
      enddo
c      xsptl(4,nptlxs)=sqrt(xsptl(1,nptlxs)**2+xsptl(2,nptlxs)**2
c      &     +xsptl(3,nptlxs)**2+xsptl(5,nptlxs)**2)
      idptlxs(nptlxs)=id
      istptlxs(nptlxs)=0

      id=10
      nptlxs=nptlxs+1
      do i=1,5
         xsptl(i,nptlxs)=epp(i)
      enddo
```

```
      idptlxs(nptlxs)=id
      istptlxs(nptlxs)=0
      do i=1,2
         print *, 'particle ',i,'px:',xsptl(1,i),'py:',xsptl(2,i),
     &           'pz:',xsptl(3,i),'E:',xsptl(4,i),'m:',xsptl(5,i)
      enddo

C     call d2a
C     call c2s(100)
#ifdef __CXDEBUG__
      if(isx.ge.4)write(ifck,*)'decay ',id,' --> ',nptlxs-nptl0,' ptls'
      if(isx.ge.6)call cxalist('QBallInt&',1,nptlxs,2)
#endif

      END


C-----------------------------------------------------------------------
      SUBROUTINE lvomegathreshold(kappa, vcmass, threshold)
C-----------------------------------------------------------------------
      implicit none
      double precision kappa, vcmass, threshold

      threshold = vcmass*sqrt((1+kappa)/(2*kappa))
      return
      end

      subroutine lvdrawrandomenergy(kappa, omega, vcmass, drawnenergy)
      implicit none
      double precision kappa, omega, vcmass, drawnenergy
      double precision Eminus, Eplus, Gamma, r, drangen
      integer nbins, i, j, low, high, mid, k
      double precision x(100000), y(100000)

      Eminus = 0

      Eplus = (omega-vcmass**2/(2.0*omega*kappa))*(1.0-kappa)

      Gamma = 0

      nbins = 100000
      i = 2
      x(1) = Eminus
      y(1) = 0.0

      do while( i < nbins )
      x(i) = Eminus + (Eplus-Eminus)/(nbins)*i

      y(i) = (2.0*kappa*omega/(1.0-kappa*kappa)*
     &(omega*x(i)-x(i)*x(i)/2.0)
     &-vcmass**2/(1.0-kappa)*x(i)
     &+kappa/((1.0-kappa*kappa)*(1.0-kappa))*x(i)*x(i)*x(i)/3)/
     &(2.0*kappa*omega/(1.0-kappa*kappa)*
     &(omega*Eplus-Eplus*Eplus/2.0)
     &-vcmass**2/(1.0-kappa)*Eplus
     &+kappa/((1.0-kappa*kappa)*(1.0-kappa))*Eplus*Eplus*Eplus/3)

      i = i + 1
      end do

      call random_number(r)
c       r = drangen(omega)
      low = 0
      high = nbins - 1
      do while (low <= high)
        mid = (low + high)/2
        if(r < y(mid)) then
          if(y(mid-1) <= r .and. y(mid) >= r) then
             drawnenergy = x(mid-1) + (x(mid)-x(mid-1))/(y(mid)-y(mid-1
     &))*(r-y(mid-1))
            return
          end if
          high = mid - 1
```

```
          end if
          if(r >= y(mid)) then
            if(y(mid) <= r .and. y(mid+1) >= r) then
               drawnenergy = x(mid) + (x(mid+1)-x(mid))/(y(mid+1)-
     &y(mid))*(r-y(mid))
              return
            end if
            low = mid + 1
          end if
         end do
      return
      end


C-----------------------------------------------------------------------
C       IMPLEMENTATION OF EFFECTS VIOLATIONG LORENTZ INVARIANCE
C       FOR POSITIVE KAPPA
C-----------------------------------------------------------------------

c-----------------------------------------------------------------------
c       in subroutine propagation(imode,iCEmode)
c-----------------------------------------------------------------------

c Check particle type
      if(ida.eq.14)then !muon
        aKappa = 3e-20
        avcmass = 105658
        aThreshold = 0
        call lvomegathreshold(aKappa,avcmass,aThreshold)
        aThreshold=aThreshold/1e6

        IF(E1.GE.aThreshold) THEN
           print *,"VC_mu: ",E1,aThreshold
           imode=100
           goto 9999
        END IF

c ... unchanged code ...

        elseif(id.eq.110)then !pi0
        aKappa = 3e-20
        avcmass = 134976.0
        aThreshold = 0
        call lvomegathreshold(aKappa,avcmass,aThreshold)
        aThreshold=aThreshold/1e6

        IF(E1.GE.aThreshold) THEN
           print *,"VC_pi0:",E1,aThreshold
           imode=100
           goto 9999
        END IF

c ... unchanged code ...

        elseif(ida.eq.1120.or.ida.eq.1220)then !proton
        aKappa = 3e-20
        avcmass = 938272.0
        aThreshold = 0
        call lvomegathreshold(aKappa,avcmass,aThreshold)
        aThreshold=aThreshold/1e6

        IF(E1.GE.aThreshold) THEN
           print *,"VC_p/n:",E1,aThreshold
        END IF

c ... unchanged code ...

        elseif(ida.eq.120)then !charged pion
        aKappa = 3e-20
        avcmass = 139570.0
        aThreshold = 0
        call lvomegathreshold(aKappa,avcmass,aThreshold)
        aThreshold=aThreshold/1e6
```

```
        IF(E1.GE.aThreshold) THEN
           print *,"VC_pic:",E1,aThreshold
           imode=100
           goto 9999
        END IF


c-----------------------------------------------------------------------
c     in subroutine propagation1D(imode,iCEmode)
c-----------------------------------------------------------------------

        if(ida.eq.14)then !muon
        aKappa = 3e-20
        avcmass = 105658
        aThreshold = 0
        call lvomegathreshold(aKappa,avcmass,aThreshold)
        aThreshold=aThreshold/1e6

        IF(E1.GE.aThreshold) THEN
           print *,"VC_mu: ",E1,aThreshold
           imode=100
           goto 9999
        END IF

c ... unchanged code ...

        elseif(ida.eq.1120.or.ida.eq.1220)then !proton
        aKappa = 3e-20
        avcmass = 938272.0
        aThreshold = 0
        call lvomegathreshold(aKappa,avcmass,aThreshold)
        aThreshold=aThreshold/1e6

        IF(E1.GE.aThreshold) THEN
           print *,"VC_p/n:",E1,aThreshold
        END IF

c ... unchanged code ...

        elseif(ida.eq.120)then !charged pion
        aKappa = 3e-20
        avcmass = 139570.0
        aThreshold = 0
        call lvomegathreshold(aKappa,avcmass,aThreshold)
        aThreshold=aThreshold/1e6

        IF(E1.GE.aThreshold) THEN
           print *,"VC_pic:",E1,aThreshold
           imode=100
           goto 9999
        END IF

c ... unchanged code ...

        elseif(id.eq.110)then !pi0
        aKappa = 3e-20
        avcmass = 134976.0
        aThreshold = 0
        call lvomegathreshold(aKappa,avcmass,aThreshold)
        aThreshold=aThreshold/1e6
        IF(E1.GE.aThreshold) THEN
           print *,"VC_pi0:",E1,aThreshold
           imode=100
           goto 9999
        END IF


c-----------------------------------------------------------------------
c     in subroutine SHOW(IQI,EI,XMI,YMI,ZMI,DMI,XI,YI,ZI,TMI,UI,VI,WI,
c     *                 IRI,WTI,LATCHIN)
c-----------------------------------------------------------------------
c ... unchanged code ...
```

```
          IF (ABS(IQ(NP)).EQ.1) THEN !new
             aKappa = 3e-20
             avcmass = 511000.0
             aThreshold = 0
             call lvomegathreshold(aKappa,avcmass,aThreshold)
             aThreshold=aThreshold/1e6

             IF(E(NP).GE.aThreshold) THEN
                print *,"VC_e:  ",E(NP),aThreshold,NP
                aTempEnergy = E(NP)*1e6
                aDrawnEnergy = 0
                call lvdrawrandomenergy(aKappa,aTempEnergy,avcmass,
     &               aDrawnEnergy)
                print *,"VC_P:",aDrawnEnergy/1e6
                E(NP)=aDrawnEnergy/1e6
                IQ(NP+1)=IQ(NP)
                IQ(NP)=0
                E(NP+1)=aTempEnergy/1e6-E(NP)
                U(NP+1)=U(NP)
                V(NP+1)=V(NP)
                W(NP+1)=W(NP)
                X(NP+1)=X(NP)
                Y(NP+1)=Y(NP)
                Z(NP+1)=Z(NP)
                IR(NP+1)=IR(NP)
                XM(NP+1)=XM(NP)
                YM(NP+1)=YM(NP)
                ZM(NP+1)=ZM(NP)
                DM(NP+1)=DM(NP)
                TM(NP+1)=TM(NP)
                WT(NP+1)=WT(NP)
                DNEAR(NP+1)=DNEAR(NP)
                LATCH(NP+1)=LATCH(NP)
                NP=NP+1
             END IF
          END IF

          IF (IQ(NP).EQ.0) THEN !unchanged
            CALL PHOTONCX(IRCODE)
          ELSEIF (ABS(IQ(NP)).EQ.1) THEN
            CALL ELECTRCX(IRCODE)
          ELSE
            IARG=100
            CALL AUSGABCX(IARG)
          END IF

c-----------------------------------------------------------------------
c      in subroutine HadronShower(n,iCEmode)
c-----------------------------------------------------------------------
c ... unchanged code ...
            if(imode.eq.3)then
              call cdecay
           elseif(imode.eq.100)then !new
              print *, 'Special VC interaction'
              call VCPionInteraction
c ... unchanged code ...

c-----------------------------------------------------------------------
c      in subroutine c2s(imode)
c-----------------------------------------------------------------------
      implicit double precision (a-h,o-z)
#include "conex.h"
#include "conex.incnex"
      dimension p(6)
      dimension ep(3)
      common/cossins/s0xs,c0xs,s0s,c0s
      ist=0
      if(imode.ne.3.and.imode.ne.4.and.imode.ne.100)then !new
        ist=-1
c ... unchanged code ...
```

B.2 Negative Value of κ

```
C-----------------------------------------------------------------------
      SUBROUTINE lvomegathreshold(kappa, vcmass, threshold)
C-----------------------------------------------------------------------
      implicit none
      real*8, intent(in) :: kappa
      real*8, intent(out) :: threshold

      threshold = 2*511000*sqrt((1-kappa)/(-2*kappa))
      return
      end

      subroutine lvdrawrandomenergy(kappa, omega, drawnenergy)
      implicit none
      real*8, intent(in) :: kappa, omega
      real*8, intent(out) :: drawnenergy
      real*8 :: Eminus, Eplus, Gamma, r
      integer*4 :: nbins, i, j, low, high, mid, k
      real*8, dimension(100000) :: x, y

      Eminus = 0.5*omega*(1.0 - sqrt((1.0+kappa)/(1.0-kappa))*sqrt(1.0-
     &(1022000.0*sqrt((1.-kappa)/(-2.0*kappa)))**2/(omega**2)))

      Eplus = 0.5*omega*(1.0 + sqrt((1.0+kappa)/(1.0-kappa))*sqrt(1.0-
     &(1022000.0*sqrt((1.-kappa)/(-2.0*kappa)))**2/(omega**2)))

      Gamma = -1.0/(137.0*sqrt((1.0+kappa)/(1.0-kappa))*(1+kappa)*(1+
     &kappa))*((2*kappa/(3*omega**2)*Eplus**3)-(2*kappa/(3*omega*omega)*
     &Eminus**3)-(kappa/omega*Eplus**2)+(kappa/omega*Eminus**2)+
     &(kappa/(1.0-kappa)-(1+kappa)*511000.0**2/(omega**2))*
     &Eplus-(kappa/(1.0-kappa)-(1+kappa)*511000.0**2/(omega**2))*Eminus)

      nbins = 100000
      i = 2
      x(1) = Eminus
      y(1) = 0.0

      do while( i < nbins )
      x(i) = Eminus + (Eplus-Eminus)/(nbins)*i

      y(i) = -1.0/(Gamma*137.0*sqrt((1.0+kappa)/(1.0-kappa))*(1+kappa)*
     &(1+kappa))*((2*kappa/(3*omega*omega)*x(i)**3)-(2*kappa/(3*
     &omega*omega)*Eminus**3)-(kappa/omega*x(i)**2)+(kappa/omega*
     &Eminus**2)+(kappa/(1.0-kappa)-(1+kappa)*511000.0**2/
     &(omega**2))*x(i)-(kappa/(1.0-kappa)-(1+kappa)*511000.0**2/
     &(omega**2))*Eminus)

      i = i + 1
      end do

      call random_number(r)
      low = 0
      high = nbins - 1
      do while (low <= high)
        mid = (low + high)/2
        if(r < y(mid)) then
          if(y(mid-1) <= r .and. y(mid) >= r) then
             drawnenergy = x(mid-1) + (x(mid)-x(mid-1))/(y(mid)-y(mid-1
     &))*(r-y(mid-1))
            return
            end if
          high = mid - 1
          end if
          if(r >= y(mid)) then
            if(y(mid) <= r .and. y(mid+1) >= r) then
               drawnenergy = x(mid) + (x(mid+1)-x(mid))/(y(mid+1)-
     &y(mid))*(r-y(mid))
              return
            end if
            low = mid + 1
          end if
         end do
      return
      end
```

```
C-----------------------------------------------------------------------
      SUBROUTINE lvpizerogfactor(kappa,energy,gfactor)
C-----------------------------------------------------------------------
      implicit none
      real*8, intent(in) :: kappa, energy
      real*8, intent(out) :: gfactor
      real*8 :: ecut

      ecut = 134.9766*1e6*sqrt((1-kappa)/(-2*kappa))

      if(energy < ecut) then
         gfactor = sqrt(1-kappa**2)/((1-kappa)**3)*(1-(energy**2
     &   -(134.9766*1e6)**2)/((1-kappa)/(-2*kappa)*
     &   (134.9766*1e6)**2))**2
      end if
      if(energy >= ecut) then
         gfactor = 0
      end if

      return
      end


C-----------------------------------------------------------------------
C       IMPLEMENTATION OF EFFECTS VIOLATIONG LORENTZ INVARIANCE
C       FOR NEGATIVE KAPPA
C-----------------------------------------------------------------------

c-----------------------------------------------------------------------
c       in subroutine propagation(imode,iCEmode)
c-----------------------------------------------------------------------
c ... unchanged code ...

      elseif(id.eq.110)then !pi0
        mc2ce=.false.
        np=2
        aPionKappa = -9e-16
        aPionTempEnergy = E1*1e9
        aGfactor = 1
        call lvpizerogfactor(aPionKappa,aPionTempEnergy,aGfactor)
        B= bdeca(6)*aGfactor


c-----------------------------------------------------------------------
c      in subroutine SHOW(IQI,EI,XMI,YMI,ZMI,DMI,XI,YI,ZI,TMI,UI,VI,WI,
c      *                IRI,WTI,LATCHIN)
c-----------------------------------------------------------------------
c ... unchanged code ...

        IF (IQ(NP).EQ.0) THEN !new
           aKappa = -9e-16
           aThreshold = 0
           call lvomegathreshold(aKappa,aThreshold)
           aThreshold=aThreshold/1e6
          IF(E(NP).GE.aThreshold) THEN
            aTempEnergy = E(NP)*1e6
C            print *,"found photon above threshold!",E(NP)
            IQ(NP)=-1
            aDrawnEnergy = 0
            call lvdrawrandomenergy(aKappa,aTempEnergy,aDrawnenergy)
            E(NP)=aDrawnenergy/1e6
            IQ(NP+1)=1
            E(NP+1)=aTempEnergy/1e6-E(NP)
            U(NP+1)=U(NP)
            V(NP+1)=V(NP)
            W(NP+1)=W(NP)
            X(NP+1)=X(NP)
            Y(NP+1)=Y(NP)
            Z(NP+1)=Z(NP)
            IR(NP+1)=IR(NP)
            XM(NP+1)=XM(NP)
            YM(NP+1)=YM(NP)
```

```
    ZM(NP+1)=ZM(NP)
    DM(NP+1)=DM(NP)
    TM(NP+1)=TM(NP)
    WT(NP+1)=WT(NP)
    DNEAR(NP+1)=DNEAR(NP)
    LATCH(NP+1)=LATCH(NP)
    NP=NP+1
  END IF
END IF

IF (IQ(NP).EQ.0) THEN !unchanged
  CALL PHOTONCX(IRCODE)
ELSEIF (ABS(IQ(NP)).EQ.1) THEN
  CALL ELECTRCX(IRCODE)
ELSE
  IARG=100
  CALL AUSGABCX(IARG)
END IF
```

C. Additional Figures

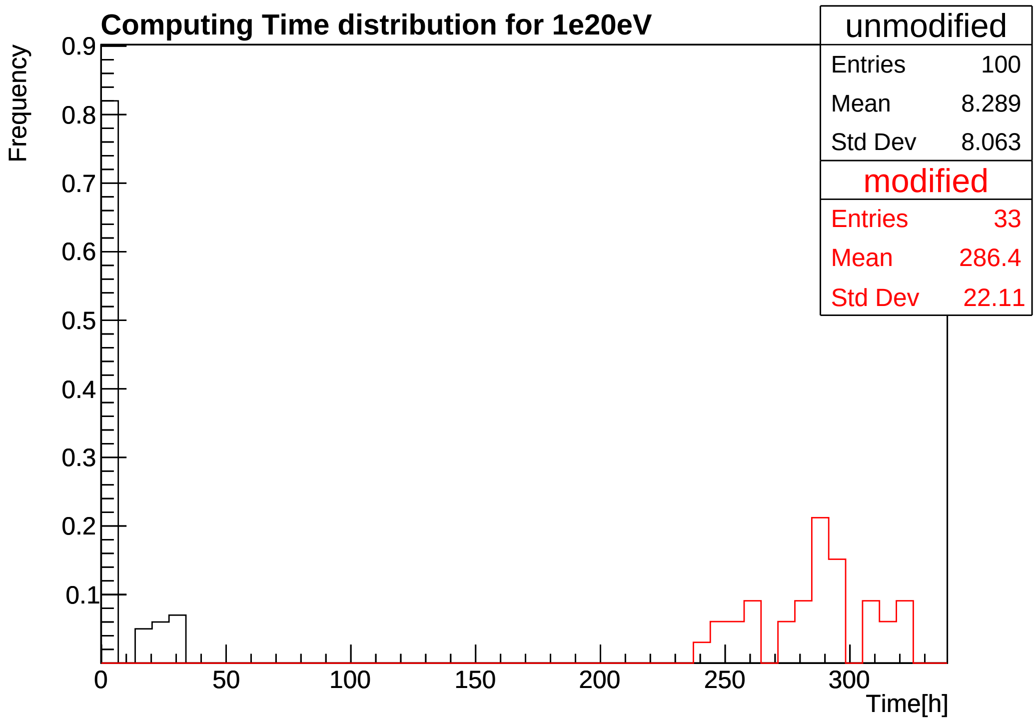

Figure C.1. *Comparison of two histograms depicting the different computing times for iron initiated air showers with different thinning levels with a primary energy of* $E = 10^{20}$ eV. *Only* 33 *out of* 100 *simulations for the modified case were completed within* 14 *days.*

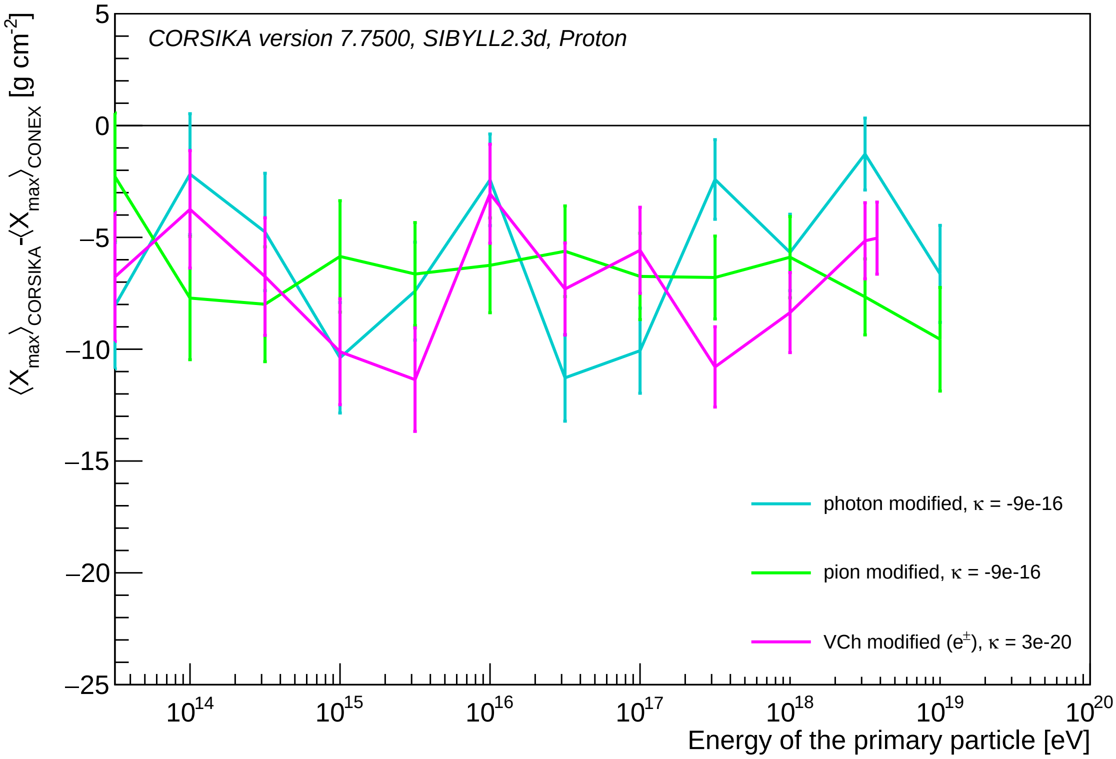

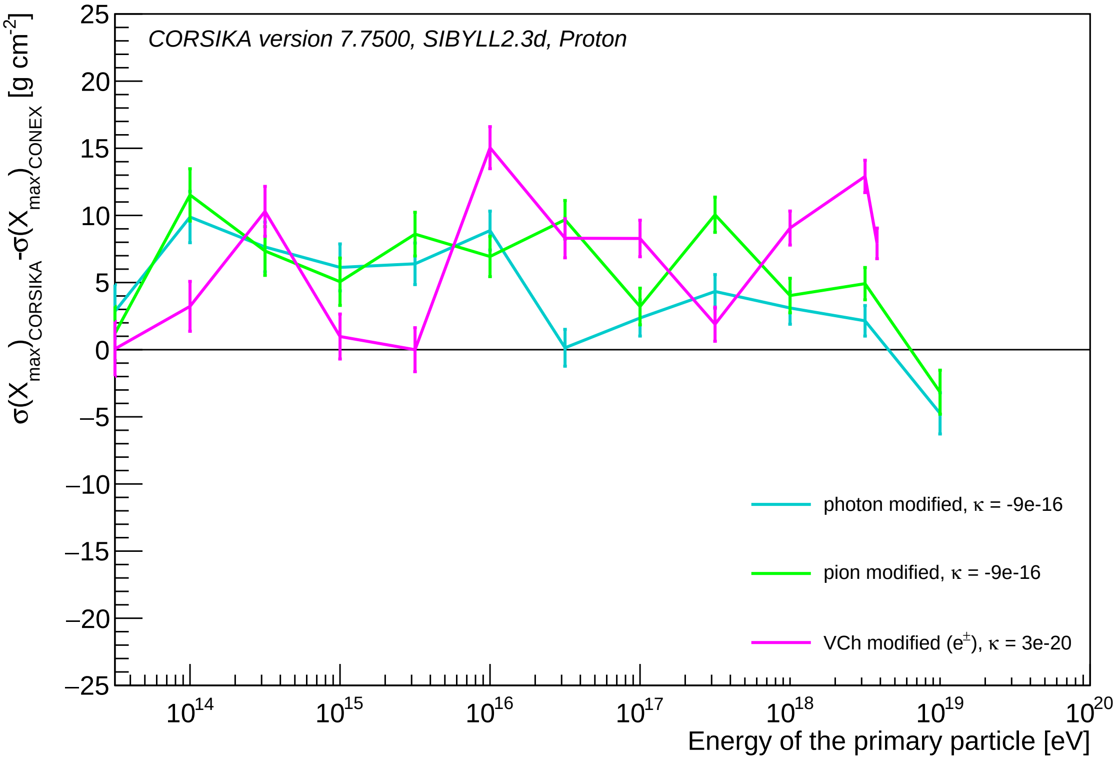

Figure C.2. *Difference between $\langle X_{max}\rangle$ values for CORSIKA and CONEX simulations as a function of the primary energy of the initiating proton is shown at the top plot. The difference of $\sigma(X_{max})$ is shown in the bottom plot.*

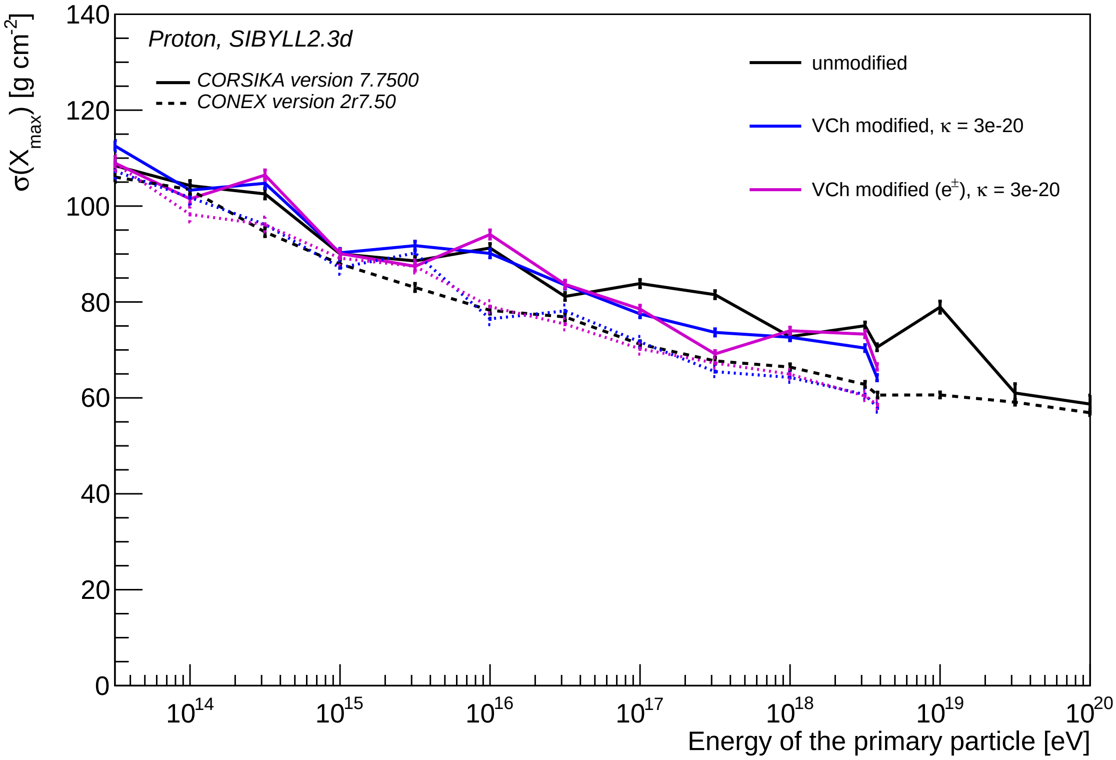

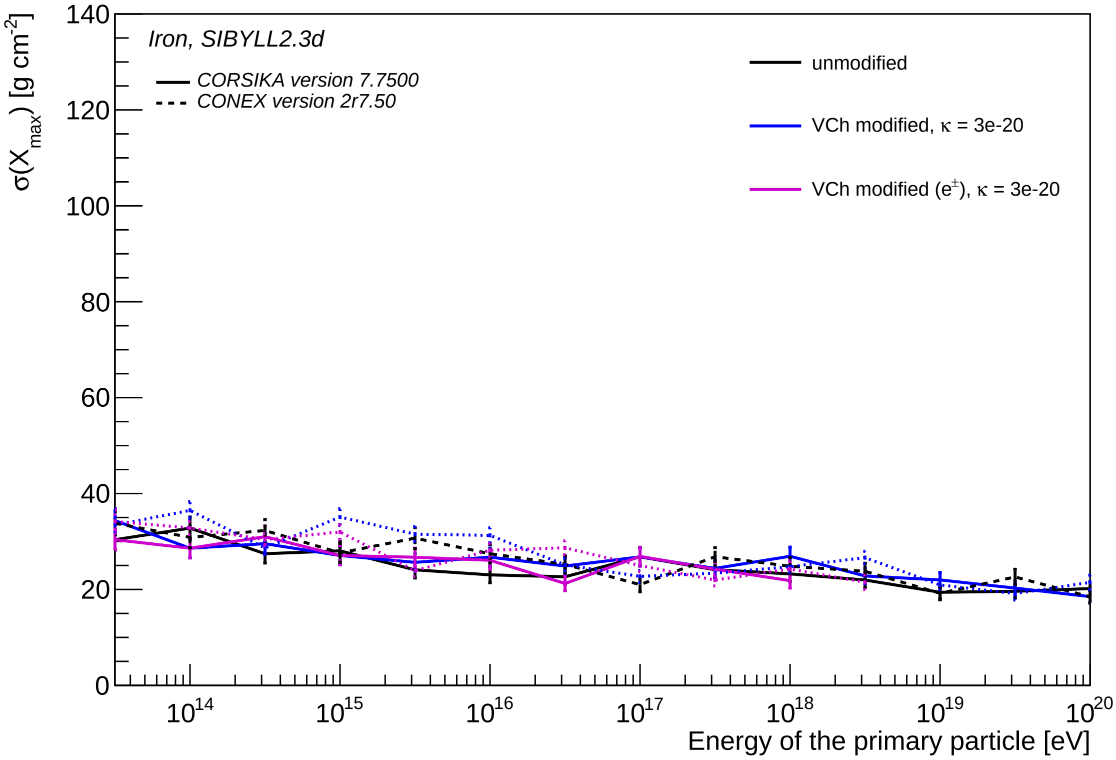

Figure C.3. *Simulated values of $\sigma(X_{max})$ as a function of the primary energy of the initiating particle. CORSIKA simulations are shown by the solid lines, while CONEX simulations are shown with a dashed line. Protons were used as the primary particle for the top plot and iron for the bottom plot.*

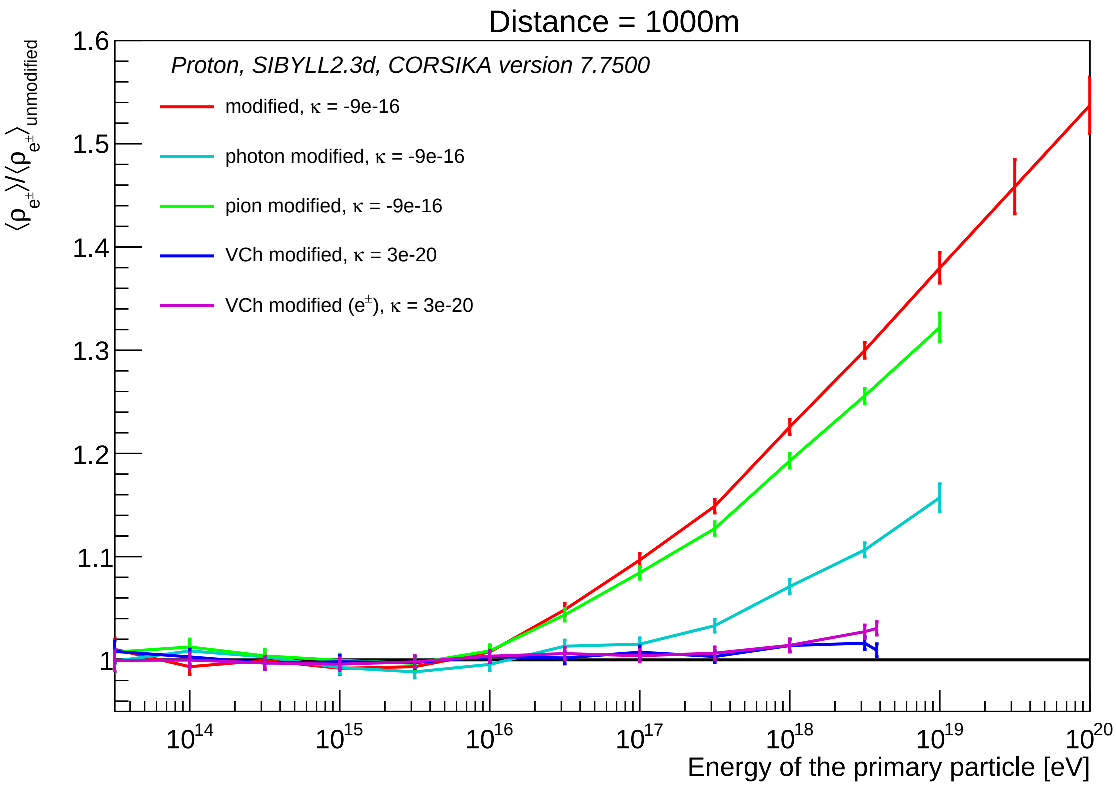

Figure C.4. *Average electron and positron density* $\langle \rho_{e^\pm} \rangle$ *at ground level, normalized to the unmodified case for proton-initiated air shower simulations. The values are plotted as a function of the primary energy at a set distance of* 1 *km.*

D. Acknowledgments

At the conclusion of this thesis, I would like to thank the people who accompanied me throughout its creation for their support and their patience until its completion.

First of all, I would like to thank Prof. Dr. Markus Risse, who made it possible for me to complete this thesis, and who was always available for conversation and helpful suggestions. I wish to thank Prof. Dr. Markus Cristinziani for agreeing to be the second reviewer.

I would also like to thank Dr. Tanguy Pierog to take the time to answer some questions I had on CORSIKA.

Special thanks go to Dr. Fabian Dünkel for supervising my work, always making time for questions, and sharing suggestions – even after leaving the working group. Likewise I am grateful for the thoughtful advice of Dr. Marcus Niechciol.

I would also like to thank the entire Experimental Particle Physics group for creating a welcoming working environment, not only for the master's thesis, but for the course of the degree in general.

Finally, my thanks are due to my family and friends for their encouragement and support through proofreading and motivating words throughout the course of this thesis.

E. Declaration of Authorship

Hiermit erkläre ich, dass ich die vorliegende Masterarbeit selbständig verfasst und keine anderen als die angegebenen Quellen und Hilfsmittel benutzt, sowie Zitate und Ergebnisse Anderer kenntlich gemacht habe. Die Arbeit hat in gleicher oder ähnlicher Form noch keiner anderen Prüfungsbehörde vorgelegen.

Ort, Datum

Unterschrift